POLITECNICO DI TORINO

Master of Science in Automotive Engineering

Design and modeling of a fuel cell hybrid ecargo bike prototype

SUPERVISOR: PROF. ANDREA TONOLI

CO-SUPERVISOR: ING. SARA LUCIANI

CANDIDATE: DANTE MARIA MODESTI

A.Y. 2021/2022

Graduation session July 2022

Abstract

Increasing concern about climate change, urban pollution, and traffic congestion has led some large cities, like Amsterdam and Utrecht, to ban completely combustion engines for inner city delivery vans within the next three years, a trend which will be likely followed by other metropolitan areas throughout Europe. To comply with this regulation trend, a few delivery companies have already started adopting eCargo bikes to perform last-mile delivery, harnessing the great potential of such vehicles in terms of operating costs and service quality. However, their diffusion in the parcel delivery sector is marginal because of their limited range. In fact, delivery eCargo bikes must travel 50 to 100 Km per day on average, which is very close to the 40 to 100 Km battery range declared by major eCargo bike manufacturers. This leads to poor real-world range performance, especially in hilly regions. In this context, the present work aims at designing a hydrogen fuel cell-based range extender to be installed on a commercial eCargo delivery bike and to evaluate its performances through simulation.

A preliminary design was first carried out developing a low-fidelity, backward model of the original eCargo powertrain in order to find a commercial fuel cell meeting the average power demand over a reference drive cycle. Subsequently, appropriately sized hydrogen feed and purge circuit components were chosen, namely high pressure tank, pressure regulator, flowmeter, and all the necessary fittings to ensure a leak-free matching between the parts. Thereafter, the best layout of fuel cell, battery and power converters was determined such as to ensure the highest efficiency and an effective power split control between the two on-board energy sources. The resulting architecture included one buck DC-DC converter for the fuel cell auxiliaries, one buck-boost converter at the fuel cell output, and one bidirectional converter in charge of managing the battery and the power split. This phase was concluded with a proposed experimental layout to test the power electronics components in their assigned functions.

Having defined vehicle architecture and components, a forward model of the eCargo bike prototype was finally created on Matlab/Simulink environment to study the bike performances under dynamic, more realistic conditions. Additionally, two fuzzy-logic based controllers were designed to manage power split and the regenerative braking torque.

Results showed that a significant range extension of +145% in the most demanding conditions is achieved despite an additional 5 Kg of weight and about 10% less cargo volume. A slightly different behavior between the dynamic model and the backward simulation was observed and it was attributed to the power-split controller design, which has proven to be more successful in sustaining the battery charge level throughout the cycle rather than maximizing the fuel cell system efficiency.

Upon the completion of my journey at Politecnico di Torino, I would like to express my gratitude to those who helped me in this final research and those that made all these years unforgettable.

First and foremost, I need to thank Sara Luciani, my co-supervisor, whose unfailingly kind and considerate advice has enriched my work and skills. Then, my heartfelt gratitude goes to my supervisor, Prof. Andrea Tonoli, who has allowed me to take part to this innovative engineering research and is the paradigm of an excellent teacher, researcher, and engineer. I would also like to extend my gratitude to my colleagues at team H_2*politO and the team's academic advisor Prof. Massimiliana Carello, whose sustainability-driven cutting-edge research on hydrogen mobility inspired me and brought me on this path.*

I would like to pay a special regard to my families, without which I would not be the person I am today. My heartfelt thanksgiving goes to mum, dad, Aldo, and my brother, for believing in me more than I did. Correspondingly, I must thank Jeanine, Chuck, Em, Owen, Mooma, and Poopa; my second family that I will never forget.

Finally, I must express my profound gratitude to all the people that left a mark throughout these years. Nicola and Giovanni have been unwavering in their personal and professional support, but I shall thank Giacomo, Arturo, Caterina, Vittorio, and Rossella as well for having been such good companions both in and out of the classes. I am also very grateful to Elisa, who has left a deep mark even though her path crossed mine not too long ago.

Table of contents

1 Introduction

1.1 A more sustainable solution for last-mile delivery

As shown in Figure 1-1, the parcel delivery sector in the EU was expected to grow 7% yearly in the past decade, but it probably ended up growing even more, given the +10% globally in 2020 alone fueled by COVID-19 restrictions. It is now possible to have almost anything delivered to our doorstep, with a consequent increase in the number of vehicles on the road impacting on traffic congestion and pollution. For this reason, some large cities like Utrecht and Amsterdam have declared a complete ban of combustion engines for inner city delivery vans from 2025. To comply with these new regulations, e-commerce and delivery companies such as Coolblue, DHL and Bol.com have introduced electric delivery bikes for inner cities [1]. More specifically, such companies acquired cargo bikes designed for transporting parcels and endowed with an electric drive system that assists the rider while pedaling in a similar fashion to eBikes. These micro-mobility vehicles solve the road congestion and pollution problems at the same time, while also ensuring quality delivery service by moving through standstill traffic, using cycle lanes, and being wheeled through pedestrian areas. Additionally, the use of eCargo bikes can contribute to a healthier, happier workforce. The physical activity of using a bike is beneficial for rider health, with some companies even reporting that their eCargo bikes riders take less sick leave than other drivers [2].

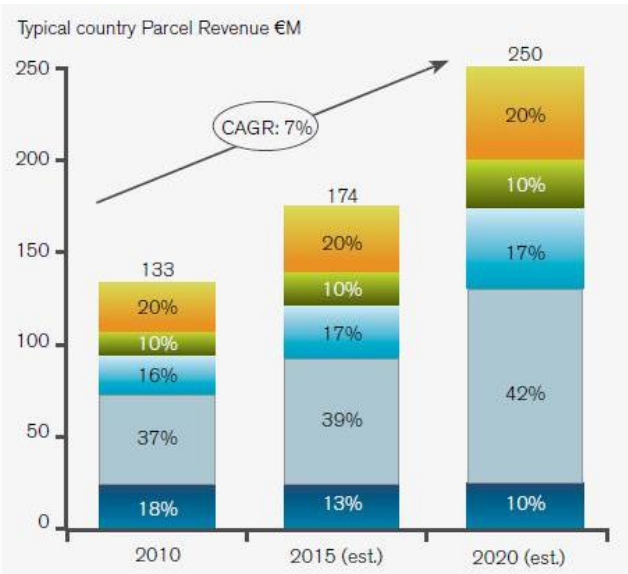

FIGURE 1-1. PROJECTED PARCEL REVENUES IN THE DECADE 2010-2020 [3]

A study concerning eBikes in Germany shows that, besides being popular among private users for leisure activities, they are increasingly frequent among postal services and home delivery services (food or small-size non-food), due to the shortness of the trips and the relatively low mass/volume of the packages to be delivered. On the other hand, their diffusion in the parcel delivery segment is very marginal due to the limited loading capacity [4]. Such limitation is partially overcome by eCargo bikes, which can usually carry up to 150 Kg and can complete last-mile delivery more efficiently by decreasing the total distance travelled to distribute the same amount of goods that would be contained in a single van [5]. Another limitation which needs to be addressed is the range: for parcel and courier services the average daily trip ranges from 50 to 100 Km [4], which is far more than the range declared by eCargo makers like Urban Arrow, i.e. 40 Km on average [6], and dangerously close to the reach specified by Bergamont, i.e. 100 Km with the smallest assistance from the eDrive [7].

The distributor “De Groene Rijders” was struggling to get its bikes through the working day with one charge in the hilly region of Arnhem and the HydroCargo project cleverly addressed the issue by introducing a fuel cell-based range extender in the eCargo chain of traction. A 500W fuel cell system was successfully installed on-board a Urban Arrow bike extending more than twice its range and reducing the refill time from several hours to a few minutes [8]. Thanks to this innovative approach, the range problem is solved and finally eCargo bikes can be a viable, sustainable alternative for last-mile delivery in the parcel shipment sector.

1.2 Aims and Objectives

Following the footsteps of the HydroCargo project, the thesis’ aim is to present the design process of a prototype of fuel cell hybrid powertrain for an Italian commercial eCargo and to quantify the advantages in term of range extension and fuel consumption of two powertrain configuration: fuel cell extender-only and fuel cell extender with regenerative braking. The design process was performed with particular care towards fuel efficiency and some further aspects are addressed such as the power split management. The design process involved the following steps:

- Preliminary study aimed at fuel cell system sizing
- Selection of the main components for the new hybrid powertrain
- Dynamic simulation on Simulink environment to quantify the performance of the prototype

1.3 Thesis outline

The thesis is structured as follows. This chapter presents the formulation and motivation of the thesis’ topic and states the aims and objectives of the work. In Chapter 2 the most relevant concepts are reviewed, namely, an overview on eBike technology, fuel cells’ working principles, the architecture of fuel cell hybrid powertrains, and energy management systems. While chapter 3 addresses the preliminary design phase of the vehicle, mostly aimed at the fuel cell system selection, chapter 4 discusses the component’s lineup process and how they were modeled on Simulink. Chapter 5 presents and analyzes the results of the work, specifically the range extension and fuel consumption of the baseline vehicle, i.e. the original BCargo eBike, the fuel-cell hybrid version and the fuel-cell hybrid version with regenerative braking capability. At last, chapter 6 presents the conclusions and possible future works.

2 Literature review

2.1 eBike technology

The vehicle under study is a close relative of the eBike, sharing the same technology and control strategies. An eBike uses an electric motor to help the rider along, ensuring same feeling and performance as a normal bike, but with less effort. As shown in Figure 2-1, the electric drive can be fit either in the front/rear hub, so-called “hub motors”, or within the bike’s central movement, i.e., mid-drive eBikes both sharing the same principles for rider’s pedaling assistance.

FIGURE 2-1. EBIKE

There are two main types of eBike - throttle assist and pedal assist. The former works in a similar fashion to a motorbike, as the motor torque output is controlled by a small throttle on the handlebar, while in pedal assist bikes the motor is activated only during the pedaling action to provide “top-up” assistance to the rider [9]. There are usually several power levels of assistance available ranging from “20% extra on top of pedal effort of a whopping 300% of it, making it rather beyond the definition of top-up” [10]. At low support levels the rider generally gets a pleasant, just noticeable helping push along the way while on the highest levels the rider feels a strong push, which is very useful for eCargo bikes where riders need to travel tens of kilometers per day carrying heavy cargo without being too worn out.

To offer pedaling assistance, various sensing systems are used to detect whether pedals are turning and how much torque is being generated by the rider. This information is then translated into a “on” signal and a torque setpoint for the motor assisting the rider. The best designs, such as mid-drive systems from Bosch, Brose, Shimano, and Yamaha, produce “an instant electrical surge that exactly matches the push on the pedals, giving the strange and rather magical feeling of having bionic legs” [10].

The power output of these pedaling assistance motors is governed by regulations. In the EU, eBikes must comply with directive 2002/24/EC in order to be exempt from road homologation (i.e., license plate, driver license, etc.). The directive limits the maximum motor continuous power at 250W and states that the power output should be “progressively reduced and finally cut off as the vehicle reaches a speed of 25 km/h, or sooner, if the cyclist stops pedaling”.

2.2 Fuel cell operating principle

In general, fuel cells are chemical reactors that produce electrical energy starting from a redox reaction between two chemical species. There exist several kinds of fuel cell (see **Errore. L'origine riferimento non è stata trovata.**), but the most relevant for the purposes of this thesis are proton-exchange membrane fuel cells (PEMFCs), which produce electricity from the redox reaction below:

$$\text{Anode: } 2\mathrm{H_2} \rightarrow 4\mathrm{H^+} + 4e^- \;\; \text{Cathode: } \mathrm{O_2} + 4\mathrm{H^+} + 4e^- \rightarrow 2\mathrm{H_2O} \qquad \textbf{EQ 2-1}$$

Practically speaking, the fuel cell has points in common both with internal combustion engines (ICEs) and batteries. It is solely an energy transforming device, like an ICE, while it cannot act as a reservoir and it needs to be provided the necessary reactants from external tanks. On the other hand, its voltage-current output, also referred to as polarization curve, is close to a battery one. The operating principle is illustrated in the figure below.

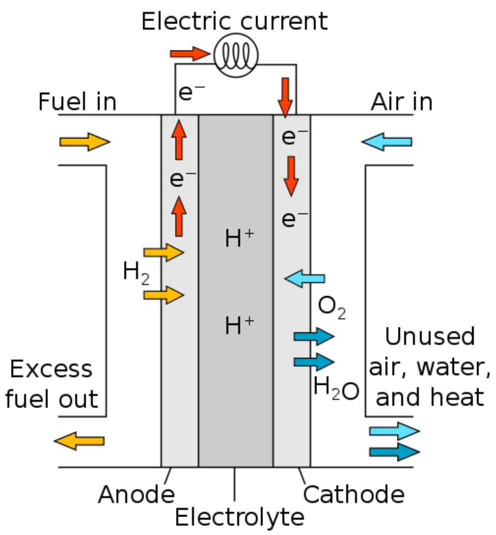

FIGURE 2-2. OPERATING PRINCIPLE OF A PEMFC [11]

A typical fuel cell polarization curve is presented in Figure 2-3, which is also illustrated with the typical losses affecting the output voltage.

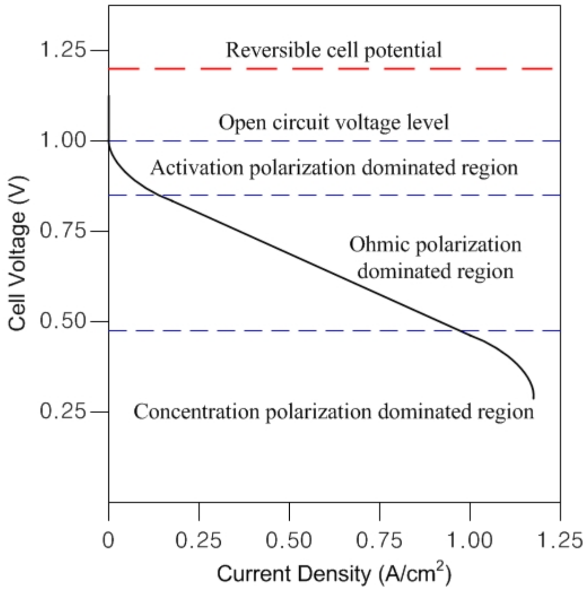

FIGURE 2-3. TYPICAL SHAPE OF A POLARIZATION CURVE [12]

The main fuel cell losses are four and they typify the shape of the polarization curve. Fuel crossover losses act throughout the whole operating range and have the effect of lowering the output voltage with respect to the reversible cell potential one. Activation losses determine the initial, steep voltage drop in the low-current region and are due to activation limitations at electrodes; ohmic losses are instead preponderant in the central quasi-linear current region and are due to internal resistance which lowers the voltage output proportionally to the output current. Finally, concentration losses are dominant in the high current region and can be attributed to local lack of reactant flow which cannot keep up with the current demand.

To quantify these losses, the stack efficiency can be defined starting from the thermodynamic efficiency η_{therm} which sets an upper bound to the cell efficiency in producing useful electrical power which is due to entropy.

$$\eta_{therm} = \frac{\Delta G}{\Delta H} = \frac{\Delta G}{LHV_{H_2}} = 0.98 \qquad \textbf{Eq 2-2}$$

Where ΔG is the Gibbs free energy released during a reversible reaction under the form of electricity, while ΔH is the hydrogen's calorific value. The latter may be equivalent to the higher heating value (HHV), in case the water produced is in gaseous state, or the lower heating value (LHV), in case the product condenses back into liquid form. As described better in the next paragraphs, for the purposes of this thesis $\Delta H = LHV_{H_2}$ because the operating temperature of the fuel cell employed for the hybridization is well below 100 ° C and it can be assumed that most of the water output is condensed back to liquid. The resulting efficiency limit at 25° C in Eq 2-2 is very close to 100%.

Therefore, the theoretical output voltage E_{th} of a fuel cell, can be defined starting from the electrical work done to move 1 mole of electrons from anode to cathode and setting it equal to the fuel's LHV, in order to take into account η_{therm}.

$$-E_{th} * n * F = LHV_{H_2}$$

$$E_{th} = \frac{LHV_{H_2}}{zF} = 1.25\,V$$ **EQ 2-3**

Where $z = 2$ is the number of electrons traveling from anode to cathode, and F is Faraday's constant. The efficiency η_{stack} of a n cells stack can finally be computed.

$$\eta_{stack} = \frac{V}{n * E_{th}} * \mu_f$$ **EQ 2-4**

Where μ_f is the fuel utilization coefficient which accounts for all the fuel that is fed to the fuel cell but does not take part to the reaction. For the purposes of this work it is assumed $\mu_f \cong 1$ [13]. As it depends on the stack output voltage, it can be easily extracted from the polarization curve.

To work properly, a fuel cell stack needs specific auxiliary subsystems (see following paragraphs for further details) which need to be fed from the FC stack itself. Together, these components make up the fuel cell system (FCS) which efficiency η_{FCS} can be characterized as follows.

$$\eta_{FCS} = \frac{P_{net}}{m_{H_2} * LHV_{H2}} = \frac{P_{stack}}{m_{H_2} * LHV_{H2}} * \frac{P_{net}}{P_{stack}} = \frac{P_{stack}}{m_{H_2} * LHV_{H2}} * \frac{P_{stack} - P_{aux}}{P_{stack}} = \eta_{stack} * \eta_{aux}$$

EQ 2-5

where P_{net} is the net power output of the FCS, P_{stack} is the net power output of the stack, and P_{aux} is the power drawn from the auxiliary systems. Finally, Eq 2-5 proves that η_{FCS} is the product of the stack efficiency η_{stack} and η_{aux} , a hereby defined efficiency which is a measure of how much power is drawn from the auxiliaries [14].

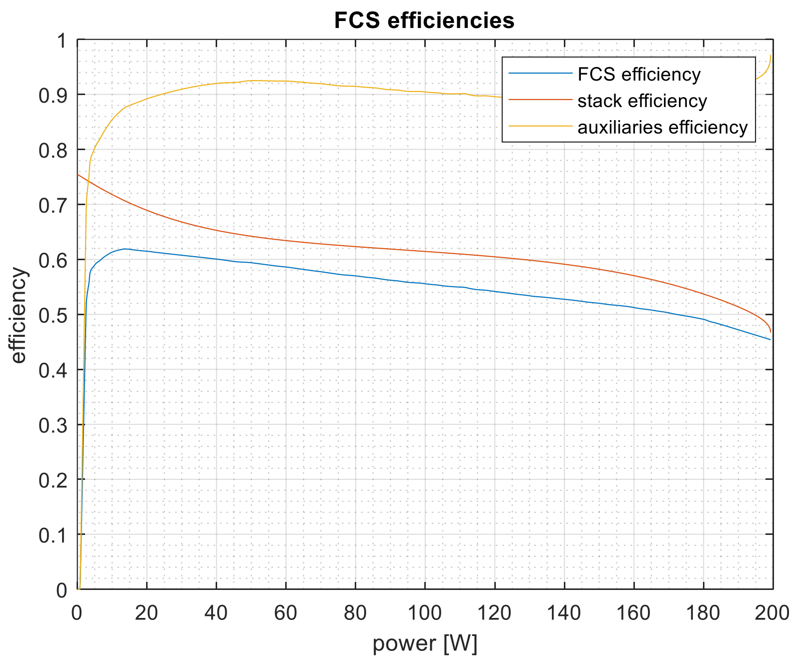

FIGURE 2-4. EFFICIENCY MAP FOR THE FCS-C200 BY HORIZON [14]

The FCS efficiency plot in Figure 2-4 was obtained by scaling an experimental diagram from Grady et al. for an FCS-C100 by Horizon to a C200 of the same family. It is thus assumed that all the FCS from this family have the same efficiency curve rescaled for the relative power output.

It is worth to notice in Figure 2-4 that fuel cells present a maximum efficiency region from 5% to 20% of the maximum FC output power, which should be kept in mind when sizing an FCS for whatever application.

From the stochiometric coefficients of electrons and hydrogen molecules in Eq 2-1 it is possible to derive a formula to calculate hydrogen consumption. From the basic operation of a fuel cell, four electrons are transferred every two moles of hydrogen. So, the amount of charges per mole of hydrogen is

$$charge\ [C] = 2F * \mathrm{H}_2[mol]$$

Dividing by time and rearranging

$$\mathrm{H}_2\ flow\ [mol\ s^{-1}] = \frac{I * n}{2F}$$

Which can then be transformed into more useful units

$$\mathrm{H}_2\ flow\ [\ Kg\ s^{-1}] = \frac{I * n}{2F} * MM_{H_2} \qquad \textbf{EQ 2-6}$$

Errore. L'origine riferimento non è stata trovata. shows many different types of fuel cell that are available according to their operating temperature and electrolyte state.

TABLE 2-1. SUMMARY OF MAIN FUEL CELL TECHNOLOGIES [15]

FCS typology	Operating temperature [°C]	Electrolyte
PEMFC	60-100	Solid
Alkaline fuel cell (AFC)	100	Liquid
Phosphoric acid fuel cell (PAFC)	60-200	Liquid
Molten carbonate fuel cell (MCFC)	500-800	Liquid
Solid oxide fuel cell (SOFC)	100-1200	Solid
Direct methanol fuel cell (DMFC)	100	Solid

All of the above-mentioned FCS use hydrogen as fuel, besides DMFC that uses methanol. There is a large consensus that PEMFC's are the most suitable technology for mobility applications because of many distinct advantages compared to the others[16], namely

- Relative low temperature operation, which ensures fast startup and the possibility of reducing the parasitic power of the auxiliaries for thermal management

- Best-in-class in terms of power density ($0.35 - 0.6\frac{W}{cm^2}$)
- The solid electrolyte is easy to manage, does not change and does not evaporate, even though it deteriorates in time
- Resistant to corrosion, as no corrosive species are involved in the reaction
- Ambient air can be used as oxidant

A PEMFC uses a solid polymeric proton exchange membrane (PEM) which was originally patented as Nafion® by Dupont and it is based on the use of sulfonated fluoro-polymers, usually fluoroethylene.

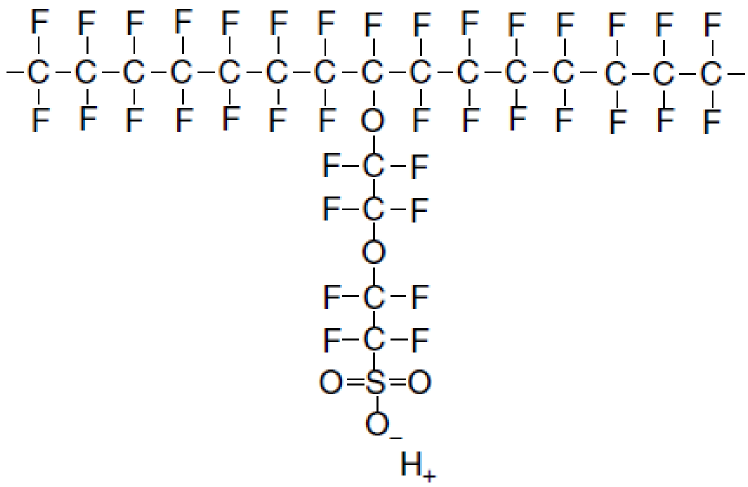

FIGURE 2-5. EXAMPLE OF STRUCTURE OF SULPHONATED FLUOROETHYLENE

The HSO_3 group added is ionically bonded, for this reason the resulting structure is called a ionomer. Such ionomer is highly iodophilic and leads to the absorption of very large quantities of water, increasing the dry weight of the material by up to 50%. Within these hydrated and slightly acidic regions, the H^+ ions are attracted to the SO^3 group and can move. In other words, if this membrane is highly hydrated it acts as a good electrolyte, conducing protons from the anode to the cathode.

The PEM is included into a sandwich-like structure called membrane-electrode assembly (MEA) which includes two catalyst layers and two gas diffusion layers. The MEA is then enclosed within two bipolar plates which act as current collector and is designed as to evenly distribute the reactants throughout the active surface (see Figure 2-6).

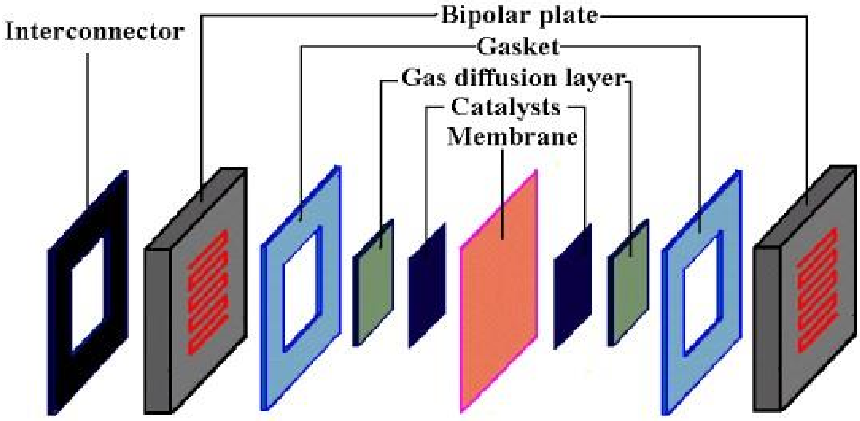

FIGURE 2-6. AN EXPLODED VIEW OF A PEMFC

The catalyst layer is a Pt-deposited carbon coating on both sides of the PEM, so the catalyst can act as electrode. The latter is particularly sensitive to poisoning due to CO and sulfur products, which affects deeply fuel cell performance. Furthermore, the amount of water within the PEM needs to be carefully managed: if it is excessive, the diffusion layers can be blocked and hinder the reactant flow to the catalyst layer, whilst if it is too dry the proton movement is hindered. For the above reasons, the inlet air usually needs to be filtered and humified before entering the fuel cell [13].

In general, for PEMFCs to work properly the following auxiliary system are required:

- Reaction air feed & humidification system
- Thermal management system
- Hydrogen feed & humidification system
- Outlet water recovery system

The most important for the purpose of this work is the hydrogen feed & humidification system because it is the only one that needs to be specifically designed for the application, while the others are built-in the commercial fuel cell acquired. There are three simple schemes for hydrogen supply systems (Figure 2-7) and the simplest is the flow-through structure scheme. In this scheme, a pressure regulator and a back-pressure valve cooperate to control anode hydrogen flux and pressure in which excessive hydrogen flows through the anode channel alongside the hydrogen needed for reactions to prevent flooding. However, this direct hydrogen emission into the atmosphere can lead to fuel waste and potential dangers and to resolve this security and economy issue, a dead-end scheme is usually adopted to ensure that the hydrogen entering the anode channels is completely consumed. In addition, because forced convection does not exist in this scheme, liquid water can easily accumulate and cause flooding, leading to the need for a purge strategy to exhaust liquid water and gas impurities. The last scheme is a recirculation mode that recirculates exhausted hydrogen back into the inlet and can not only remove hidden dangers, but also improve hydrogen utilization and system efficiency [17].

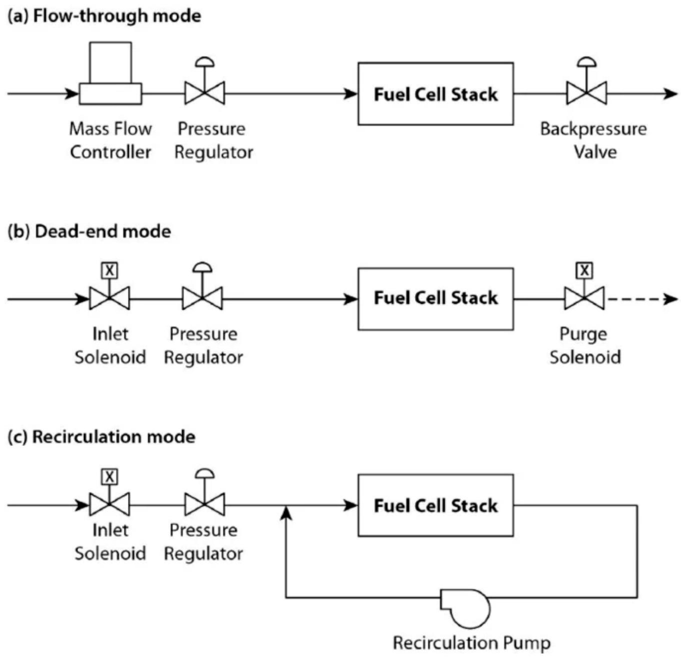

FIGURE 2-7. SCHEMATIC OF TYPICAL HYDROGEN FEED SYSTEM

The recirculation mode can be easily found in high power stacks for hydrogen mobility while dead end mode is popular among the smaller, commercial stack such as the kind selected for the prototype.

For the application on an eCargo it was decided to employ a particular design of PEMFC called "open cathode", which offers a simplified configuration in which the subsystems for cooling, humidification and inlet pressure control can be eliminated from the fuel cell system. Thus, a significantly less complex and bulky fuel cell system can be achieved by implementing this configuration, which makes it ideal for micro-mobility applications. The elimination of these complex subsystems, however, brings consequence that the stack performance is strongly affected by the surrounding conditions where temperature and humidity will fluctuate inevitably. Furthermore, this design is limited to relatively low-power PEMFCs because the heat released from the electrochemical reaction might not be sufficiently removed in high capacity fuel cells [18].

2.3 Fuel cell hybrid vehicle (FCHV) powertrain architecture

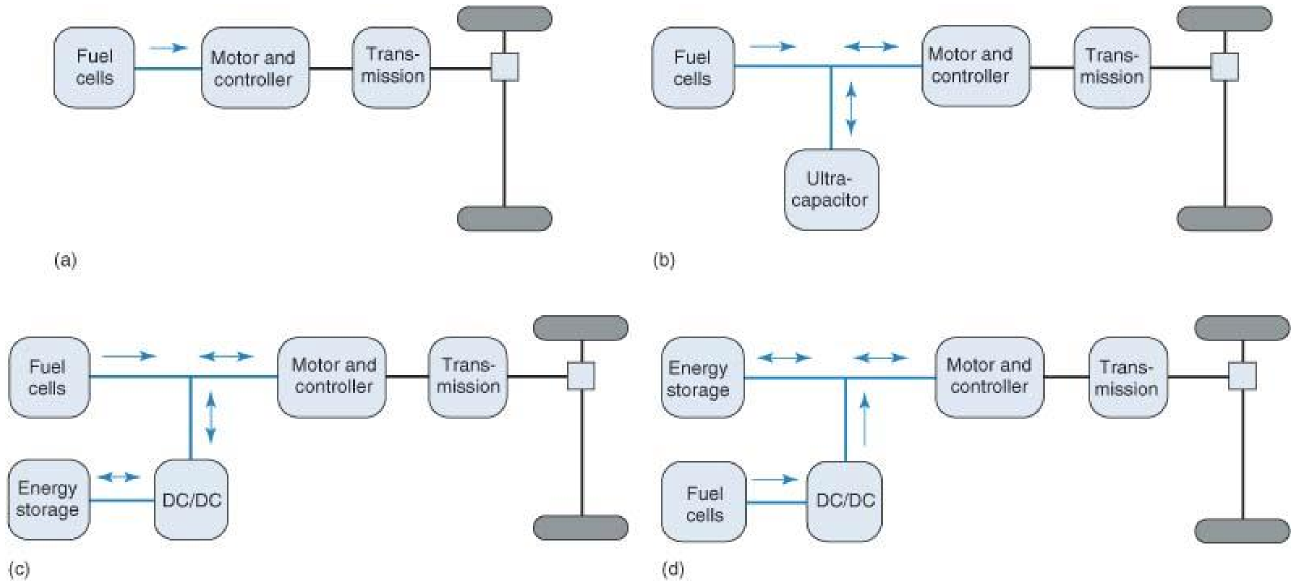

FIGURE 2-8. POWERTRAIN CONFIGURATIONS FOR FUEL CELL VEHICLES [19]

Fuel cells have been researched and successfully installed on vehicles for decades now, with many different layout and sizing approaches. Figure 2-8 reports the four main "textbook" powertrain layouts that can be described as follows [19]:

a. *A direct hydrogen FCV without electrical energy storage*. This configuration is the simplest. No DC/DC converter is employed to control the DC-link voltage resulting in the fuel cell stack voltage being equal to the DC-link voltage. Due to the low power density of FCSs, this configuration requires a higher power fuel cell and fast hydrogen and air supply systems to satisfy the large variations in load power. Even so, the DC-link voltage can experience large swings because of the poor response of PEMFCs during fast transients, thus deeply affecting the vehicle performance. Additionally, this architecture does not allow to store the recoverable energy from braking.

b. *FCVs with supercapacitors directly connected to fuel cells*. The supercapacitors are directly connected in parallel with the DC-link (fuel cell stack). In this case, the voltage of the ultracapacitor unit and fuel cell is equal. The relatively soft voltage–current characteristics of fuel cell allow supercapacitors to operate over a fairly wide range of voltages and to self-regulate the DC-link voltage fluctuation. The supercapacitors will absorb the excess power from the stack and the regenerative braking energy and provide a fraction of transient power for vehicle acceleration. A diode is utilized between the fuel cell and DC-link to prevent current from flowing into the fuel cell during regenerative braking of the vehicle. This configuration is the simplest of the hybridized powertrain arrangements, but does not allow power split control, which is a problem for mass-production vehicles for which the real-world driving conditions cannot be accurately predicted during the design phase.

c. *FCVs with electrical energy storage (supercapacitors or batteries) coupled in parallel with fuel cell stack through a DC/DC converter*. The fuel cell voltage is the DC-link voltage. The transient power provided by the energy storage is regulated by the DC/DC converter. The introduction of the DC/DC converter will maximize the utilization of supercapacitors or batteries during acceleration and cruise and regenerative braking. This configuration permits controlling the transient power from the fuel cell by applying different power split strategies such as power assist or load leveling to mitigate the stress on the fuel cell stack. The state of charge (SOC) of supercapacitors or batteries can also be controlled within appropriate ranges.

d. *FCVs with the fuel cell coupled with energy storage unit such as supercapacitors or batteries through a DC/DC converter*. The energy storage voltage is the DC-link voltage. The power provided by the fuel cell passes through the DC/DC converter. The converter regulates the fuel cell power to avoid large fluctuation of the DC-link voltage. The SOC of the battery or supercapacitor is also a factor that is determining the fuel cell output power.

Within the FC hybrid layouts, i.e., c and *d*, there are three possible dimensioning approaches definition related to the relative rated power of battery and fuel cell:

- *Full power*: the FC is sized for the maximum transient power demand, but a small battery is still present to keep the FC in the optimal operating region during very low power demand or very short, harsh transients. Also, it is possible to take advantage of regenerative braking increasing the overall energy efficiency.
- *Load follower*: the FC is sized for the maximum continuous power demand, for example when cruising on the highway. The FC is smaller compared to the previous point while the battery size is slightly larger, since it must be able to handle all transients mostly alone.
- *Range extender*: in this case the FCS power is much lower than the previous two, namely 1/10 of the nominal battery power, and it is equal to the average power demand over a defined drive cycle. The main goal of the hybridization in this case is to reduce the original battery volume and weight while increasing the vehicle's range.

The *full power* and *load follower* strategy are generally used for layout *b* , since the FCS in both cases has a comparable or even higher rated power with respect to the battery and the DC/DC on the battery size can have lower power rating than if it was to be installed on the FC side like in layout *c*. The *range extender* strategy, on the contrary, involves a relatively small capacity FC with respect to the hybridization battery, so the DC/DC should be installed on the FC side [16].

Since the aim of this thesis is mostly to extend the range of eCargo bikes, range extender is the most appropriate sizing strategy. Additionally, the fuel cell can be relatively low weight and small, thus easier to fit in the cargo compartment without taking up too much space.

2.4 Modeling approach

As stated in Chapter 1, the objective of this thesis work is to design a fuel cell hybrid powertrain to be installed on-board an eCargo bike while keeping as much as possible the original full-electric components. To reach this goal, selecting appropriate modeling approach is vital; two modeling approaches are possible, i.e., backward and forward facing, which are both employed in different phases of the design process.

Backward-facing models are often employed when a low computational cost, low fidelity model is needed for preliminary powertrain sizing and estimating roughly the fuel consumption. The reference speed trajectory is imposed on the vehicle model as an input and the torque required at wheels is computed accordingly. Following a cascade, the requirements for each component are determined backwards (hence its name) using efficiency maps that are obtained through steady-state tests, thus leading to quasi-static models that ignore transient behaviors of components. The power information flow is unidirectional, i.e., effort (torque) and flow (speed) have the same direction, and thus the system is noncausal. Figure 2-9 illustrates a backward facing model.

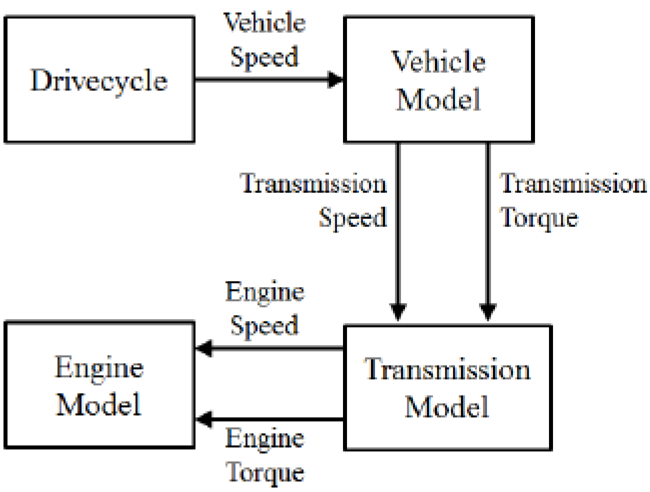

FIGURE 2-9. BACKWARD-FACING MODEL FLOWCHART

The backward facing approach is not suitable when a more realistic model is needed, as in Hardware in the Loop (HIL) tests. In this case it is preferrable to use the forward-facing approach, in which a driver model is introduced, usually as a PI controller, and the speed trajectory is no longer imposed. The driver translates the desired speed and acceleration into pedal commands, which further generates a torque request to the eMotor in order to track the desired speed trajectory. As opposed to backward facing, since the speed is not imposed, there may be a small error between desired and actual velocity. The forward-facing model flow chart is illustrated in Figure 2-10 [20].

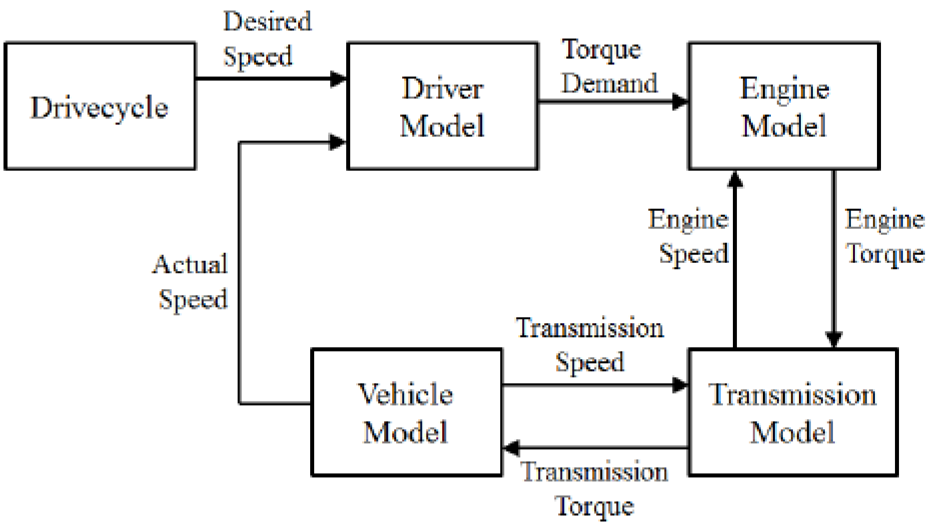

FIGURE 2-10. FORWARD-FACING MODEL FLOWCHART

Note that the forward-facing technique involves dynamic models, as opposed to the backward facing approach which was defined using quasi-static models. In the forward-facing approach the information flow is bidirectional, i.e., the actual output is fed back. Therefore, it is possible to achieve a better overview of the physical system for its use in a real application, also capturing the transient states and making it suitable for designing control systems and for implementing HIL tests. These results come at the cost of a higher model complexity due to the presence of several state equations, which require smaller time steps, i.e., a slower simulation.

A backward-facing model was implemented during the preliminary design phase explained (see chapter 3) in order to perform a preliminary sizing of the FCS. Next, a higher fidelity forward-facing model was built to test the interaction between the many components involved, i.e., power converters, fuel cell, auxiliaries, etc., and to evaluate the performance of the future prototype, with a special focus on the achievable range extension. Only the longitudinal dynamics of the eCargo bike is modeled, which is a basic modeling technique, but it can adequately represent the system for the purposes of powertrain design without increasing too much the computational cost.

2.5 Energy management systems

Hybrid vehicles involve two sets of control tasks: component-level control (also called low-level control) and high-level control. This high-level control is usually referred to the energy management system (EMS), a control system that oversees managing energy flows in and out of the many energy and power sources on-board. In a conventional vehicle, there is no need for the presence of EMS because only one main powerplant is present, i.e., the internal combustion engine, which is controlled by acting on throttle, brakes, and gear. The power desired is then translated into low-level controller, i.e., the engine electronic control unit, which manages the ICE accordingly. As most fuel cell electric vehicles are hybrid, an EMS is required. Energy management system in hybrid fuel cell vehicle consists in determining the amount of power delivered by the fuel cell and by the battery at each instant while meeting the system constraints and achieving some goals such as sustaining the state of charge and achieving a better fuel economy.

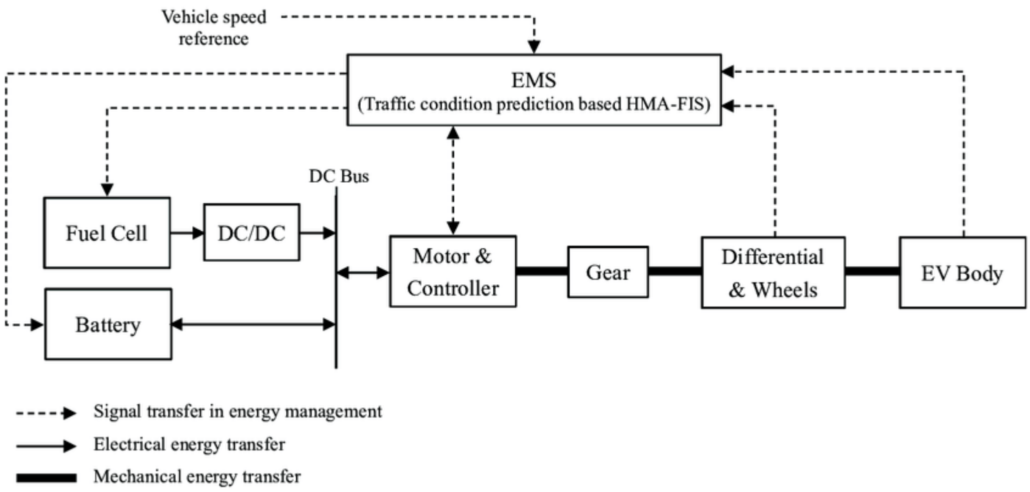

FIGURE 2-11. AN EXAMPLE OF THE ROLE OF EMS ON A FCHEV [21]

According to the power request received as an input, the EMS decides the power split between the fuel cell and the battery. As shown in the example in Figure 2-11, the reference fuel cell and battery power are sent to low-level controller (such as power converters) that enforce them.

The EMS could be classified into several families, as is shown in Figure 2-12. Two main kinds of control methods could be identified: rule-based and optimization-based. The main feature of the former is the effectiveness in real-time implementation. Decisions of fuel cell operating points made by this kind of control are based on human knowledge, intuition, or from the information obtained by offline optimization methods like dynamic programming algorithms. The result is a set of rules to control the power split. The second family is optimization-based control strategy, which aims to minimize one or more pre-defined cost functions, leading to a global or local optimum. Due to its computational complexity and requirement of prior knowledge of the drive cycle (for example, dynamic programming), they are limited in practical implementation. However, the optimization-based control strategy is helpful for benchmarking and generating rules for online implementation [22].

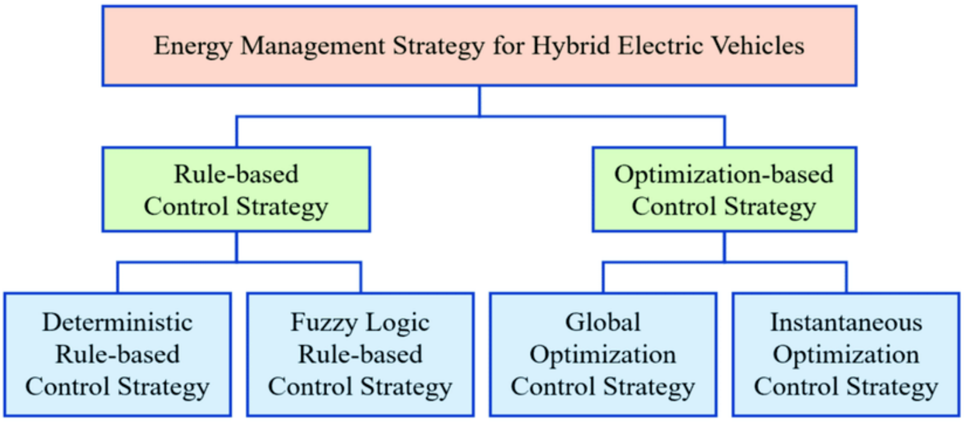

FIGURE 2-12. CLASSIFICATION OF EMSS

2.5.1 Fuzzy logic

This type of control strategy belongs to the "rule-based" EMS category. While classic logic deals with variables that represents propositions (e.g. conclusion, decision) that are "discrete", fuzzy logic uses imprecise propositions resulting in a "smooth" control actions starting from discrete rules. Fuzzy logic controllers are described by IF-THEN rules which often are based on human expertise on the controlled plant and its performance. Moreover, the membership function is somewhat subjective, depending on the designer's experience and available information.

Fuzzy control theories were first developed in the 1970s. At present, fuzzy control is widely used in many fields, such as automatic control, artificial intelligence, aerospace, rail transit, medical treatment, meteorology, finance, and so on. Its widespread application could be credited to the following advantages:

- Fuzzy logic control system is a rule-based system and has distinguishing merits in tackling systems that are not precisely described mathematical models or highly non-linear systems.
- It is a non-linear controller using linguistic variables, which is easy to be designed and implemented. It processes the intuition like human beings, easily adapting to difficulties during control actions.
- It is robust, even works well with noisy inputs. It is efficient and has a fast response.
- Concerning the designer side, it is easy to comprehend since it does not involve complex mathematical analysis. It also has a user-friendly interface, allowing designers to modify the parameters more efficiently.

The structure of a fuzzy logic controller is made of three parts: the fuzzification module, the inference engine built on rule base, and the defuzzification module, as shown in Figure 2-13.

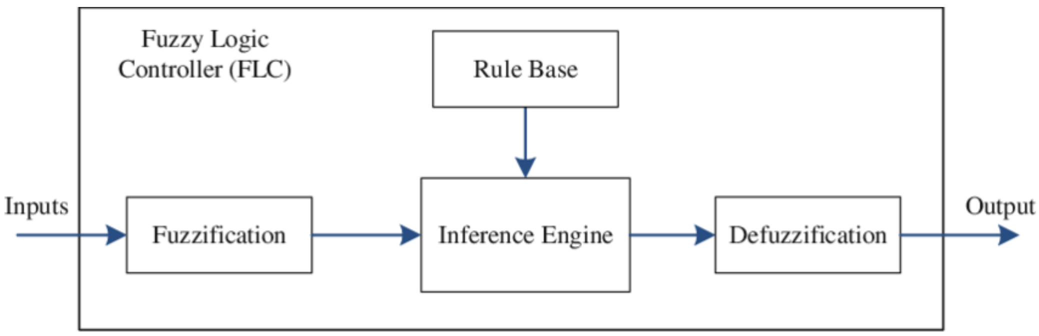

FIGURE 2-13. GENERAL STRUCTURE OF FUZZY LOGIC CONTROLLER

The fuzzification step converts the input into fuzzy subsets. The subsets include some ranges of the input and membership functions describing the degree of confidence of the belonging to a certain range. Inputs to the fuzzification module are crisp values while outputs are membership functions and their corresponding intervals. The intervals are labeled with fuzzy terms.

The outputs of the fuzzification module are then sent to the fuzzy rule base to create control actions. To be more specific, the rule base is a set of IF-THEN rules, in the following form:

$R1$: IF controller input $e1$ is $E11$ AND ... AND

controller input en is $E1n$

THEN controller output $u1$ is $U1$

$\vdots$

Rm: IF controller input $e1$ is $Em1$ AND ... AND

controller input en is Emn

THEN controller output um is Um

Where en is the input, um is the name of the outputs, Emn and Um are the fuzzy linguistic terms. The outputs are fuzzy terms Um.

Finally, the defuzzification module is a process to determine the crisp value of the outputs. Commonly used defuzzification methods are center-of-gravity methods, center-of-sums, mean-of-maxima, and so on [23].

3 Preliminary powertrain sizing

In this chapter a preliminary sizing in terms of power of the FCS and energy content for the hybridization battery is carried out through backward modeling on Matlab. The input consisted in the driving cycles explained in the next sections while the output consisted in the average power demand over the reference cycle, the required battery capacity for a good power buffering and the eCargo performance in terms of energy consumption, driveline efficiency and range extension.

3.1 Drive cycle data

As this thesis-work was carried on within the ranks of PoliTO's CARS, the necessary drive cycles to feed the backward model were borrowed from an ongoing research project on regenerative braking feasibility for eBikes. Within such project, an experimental campaign aimed at creating eBikes driving cycles was carried out by means of a rider wearing a commercial GPS watch by Garmin, see Figure 3-1.

FIGURE 3-1. A PICTURE OF THE DRIVE CYCLE'S DATA ACQUISITION DEVICE

While the bike was riding, the wristwatch was able to track altitude, speed and travelled distance and log them wirelessly to a mobile device through the app STRAVA®, which enabled the data collection into useful files and to manage the sample rate, which was set to 1 Hz. Further details regarding the statistical relevance of the experiments are not known to the author, as well as precision and accuracy of the measurements. For the scope of this thesis, it is assumed that the resulting drive cycles are 100% reliable and representative of the eBike mission profile.

Four drive cycle scenarios were considered, two urban (U1, U2) and two extra-urban (M1, M2). The former cycles were performed completing ring-like trips within the downtown area of Turin, which is mostly flat but still presents some incline. More details concerning the urban drive cycles are shown in the figures below.

FIGURE 3-2. FROM LEFT TO RIGHT, U1 & 2 MAP

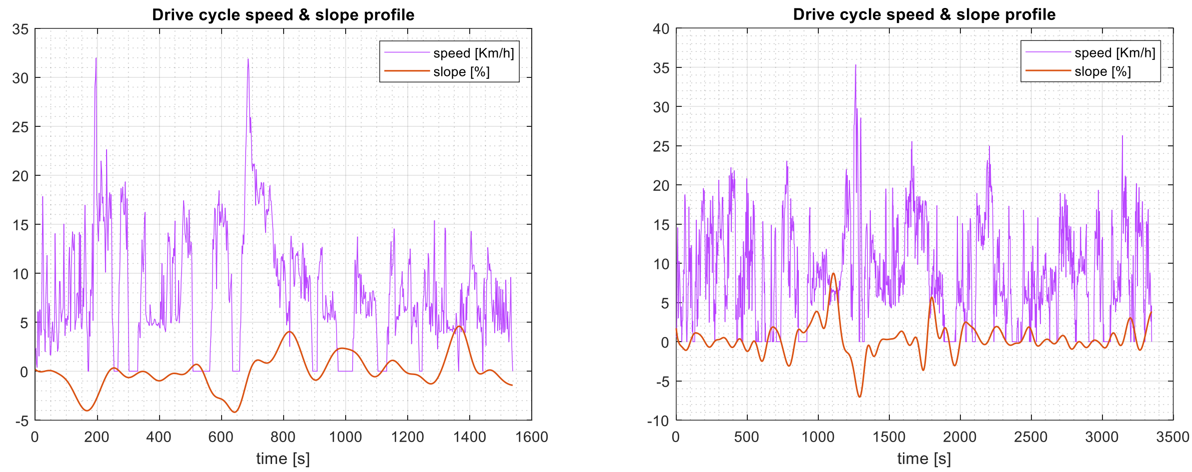

FIGURE 3-3. FROM LEFT TO RIGHT, U1 & 2 SPEED AND SLOPE PROFILE

TABLE 3-1. FURTHER DETAILS ON URBAN DRIVE CYCLES

Drive cycle	Length [Km]	Total Height difference [m]
Urban 1	13.14	82
Urban 2	5.57	34

From a first look at Figure 3-3 and Table 3-1, the U1 cycle appears to be the most demanding in terms of power; it presents the highest total height difference, the highest length, the steepest incline, and the highest peak speed. Concerning the speed, results from an early version of dynamic simulation showed that if the 2002/24/EC directive's limits on the eDrive are enforced, the vehicle is not able to even reach 25 Km/h on flat road (see next sections) nor is able to accurately track the above U1 and 2 cycles. To overcome this problem and prevent discrepancy between dynamic and quasi-static model, the U1&2 cycles were modified using the output vehicle speed of the eCargo bike longitudinal dynamics Simulink model. The resulting cycles U1eCargo & U2eCargo show a very similar behavior to U1&2 but presents lower, smoother peaks (Figure 3-5).

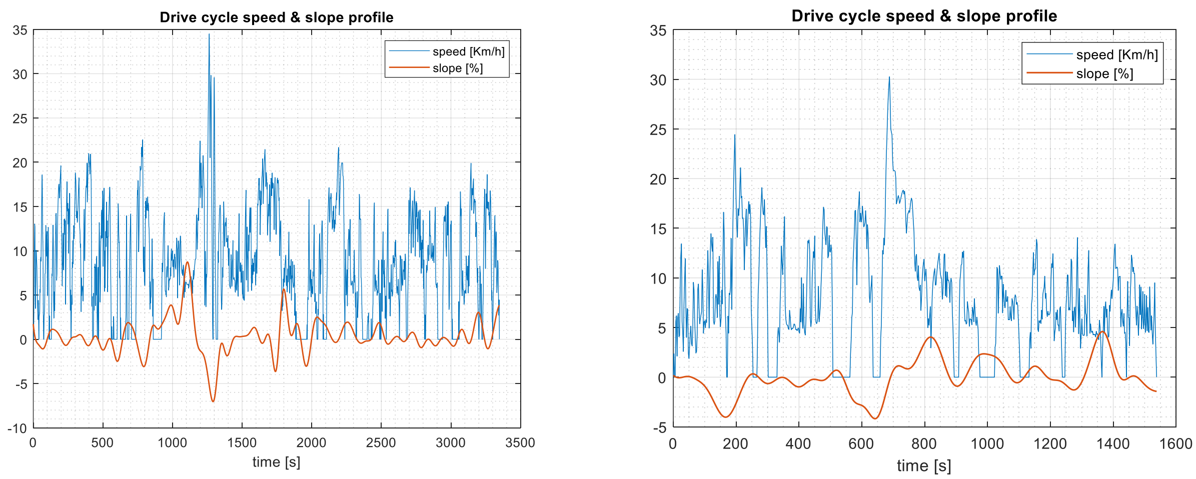

FIGURE 3-4. FROM LEFT TO RIGHT, U1&2 ECARGO CYCLES SPEED AND SLOPE PROFILE

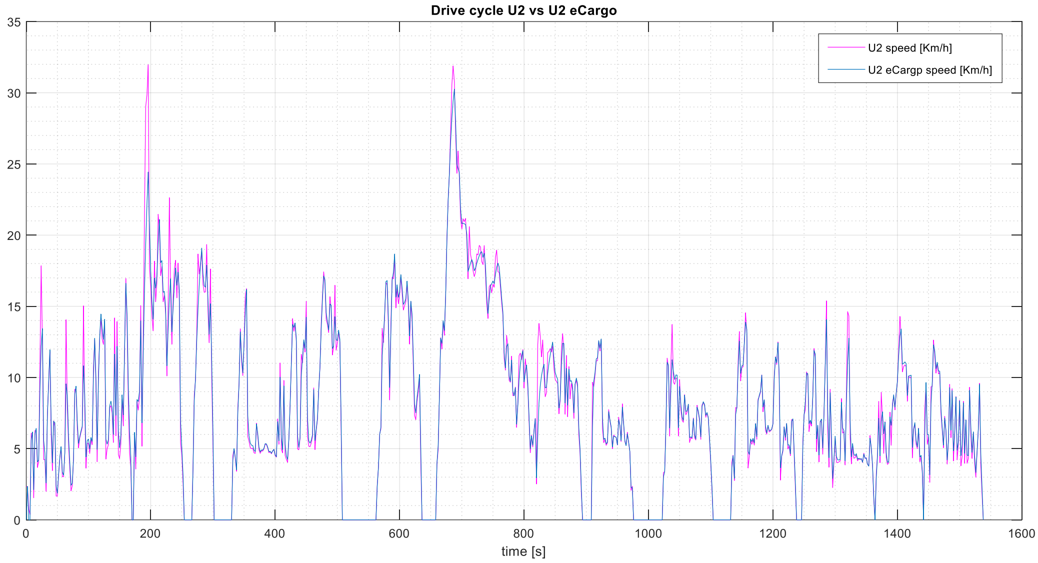

FIGURE 3-5. COMPARISON BETWEEN THE U2 ORIGINAL DRIVE CYCLE AND THE MODIFIED ONE

Going back to mountain driving cycles, M1 a ring-like trip taken in the Canavese area of Piedmont, which is a hilly region in between Turin and the Aosta valley, while M2 is a roundtrip on a single path taken in a nearby mountainous area. Note that the M1 cycle corresponds to only the blu-circled area in **Errore. L'origine riferimento non è stata trovata.**.

FIGURE 3-6. FROM LEFT TO TIGHT, CYCLES M1 & 2

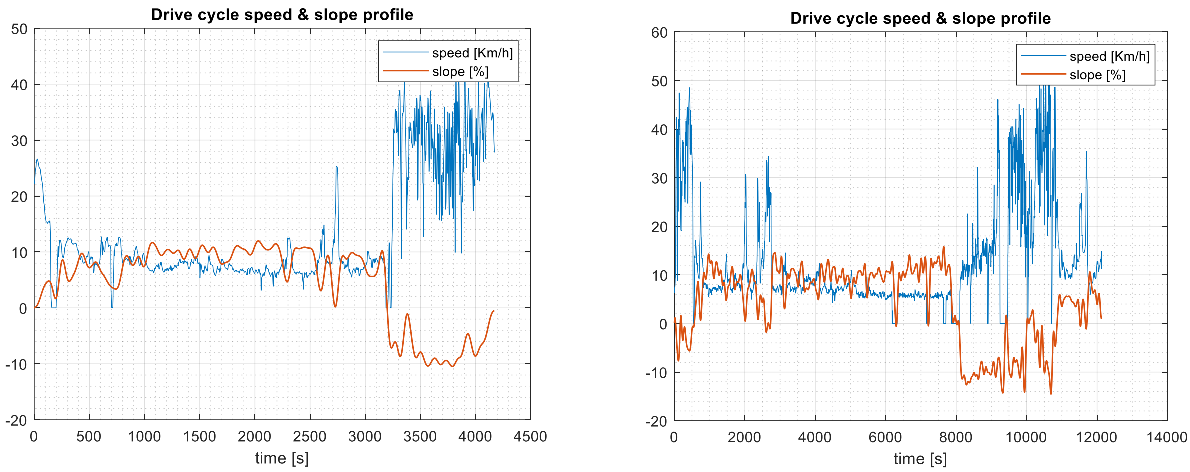

FIGURE 3-7. FROM LEFT TO RIGHT, M1&2 CYCLES SPEED AND SLOPE PROFILE

TABLE 3-2. FURTHER DETAIL ON M1&2 CYCLES

Drive cycle	Length [Km]	Total Height difference [m]
Mountain 1	16	600+600
Mountain 2	43.53	750+750

As it can be evaluated from Figure 3-7 and Table 3-2 , these cycles are definitely more energy-demanding compared to their urban counterpart, considering the much steeper incline (-10%< i < 10%) and much higher speed reached, i.e., 50 Km/h in the M2 cycle. However, judging from the expected mission profile for the eCargo bike under study which was defined in 1.1, these vehicles will be mostly used in urban environment where their advantages, i.e., ease to find parking, ability to take shortcuts, low operating costs, etc., can be fully exploited. For this reason, M1&2 cycles were considered only for fuel cell system dimensioning purposes and were not included into the dynamic simulation.

3.2 Bike longitudinal dynamics model

FIGURE 3-8. THE BCARGO BIKE

As stated in 1.3, the starting point for the design and modeling was the eCargo from Italian maker BCargo, which main parameters are summarized in Table 3-3.

TABLE 3-3. BCARGO BIKE MODELING PARAMETERS [24]

Curb mass, *UM*		34 Kg
Laden mass, *LM*		180 Kg
Battery energy, $E_{batt\,0}$		500 Wh
Cargo volume		240 l
eDrive	**Max continuous torque, $T_{m\,cont}$**	80 Nm
	Max continuous power, $P_{m\,cont}$	250 W
	Rated supply voltage, V_{bus} [25]	36 V
Traction (rear) wheel diameter, *D*		26 inches

The first step of the backward modeling was to implement the power balance equation, in order to obtain the power demand at the wheel over the considered driving cycles. The generic power balance equation for a vehicle's longitudinal dynamics is the following:

$$m_a * \frac{dV}{dt} * V = P_{wheel} - P_{aero} - P_{slope} - P_{rr} \qquad \textbf{Eq 3-1}$$

Where:

$P_{aero} = \frac{1}{2} * \rho * V^3 * C_D * S$ is the aerodynamic power lost

$P_{slope} = m * g * V * \sin(\alpha)$ is the road angle power lost

Input variables:

V vehicle speed

α road angle

$P_{rr} = m * g * f * V * \cos(\alpha)$ is the rolling resistance power lost

Physical constants:
$\rho = 1.2\ Kg\ m^{-2}$, air density
$g = 9.81\ m\ s^{-2}$, gravity acceleration

Solving for P_{wheel}, the power demand at the wheel axle, Eq 3-2 is obtained.

$$P_{wheel} = m_a * \frac{dV}{dt} * V + P_{aero} + P_{slope} + P_{rr} \qquad \textbf{Eq 3-2}$$

The parameters' values in **Errore. L'origine riferimento non è stata trovata.** were included from CARS project on regenerative braking feasibility for eBikes and are considered representative for the vehicle category, even though no information on their origin is available to the author.

TABLE 3-4. SUMMARY OF PARAMETERS EXTRACTED FROM CARS PROJECT AND THEIR CORRECTED VALUES

η_{transm} **transmission efficiency**	0.96
η_{eMot} **electric motor average efficiency**	0.95
η_{inv} **inverter average efficiency**	0.95
C_D **drag coefficient**	0.825
f **rolling coefficient**	0.01
S_{bd} **original frontal area of bike and rider**	0.475 m^2
S **frontal area corrected**	1 m^2

According to the data available and the desired fidelity of the backward model, the following hypotheses and corrections were made:

1. Rotational inertia is considered negligible, so the apparent mass is assumed near-equal to the test mass, $m_a \cong m$
2. Test mass m is calculated considering 50% of the payload, assuming that half of the trip will be at full load while the other half will be empty

$$m = UM + EM + RM + 0.5 * (LM - RM - UM) \qquad \textbf{Eq 3-3}$$

Where:

$UM =$ curb mass
$RM =$ rider mass, assumed to be 80 Kg
$EM =$ mass of extra on-board equipment to be installed for hybridization. Estimated 10 Kg
$LM =$ laden mass

TABLE 3-5. TEST MASSES FOR THE TWO ECARGO CONFIGURATION UNDER STUDY

m **resulting vehicle test mass**	**Original**	147 Kg
	FC hybrid	157 Kg

3. The frontal area S is corrected to consider the presence of the box. The front size of the box was estimated from another cargo bike maker Urban Arrow while available data on bike frontal area was halved, since the box covers the lower part of the bike.

$$S = (h * w) + \frac{1}{2} * S_{bd} = 1\, m^2 \qquad \textbf{Eq 3-4}$$

h, w : estimated height & width of frontal box, respectively $1.10\, m \times 0.7\, m$ [26]
S_{bd}: frontal area of bike and rider

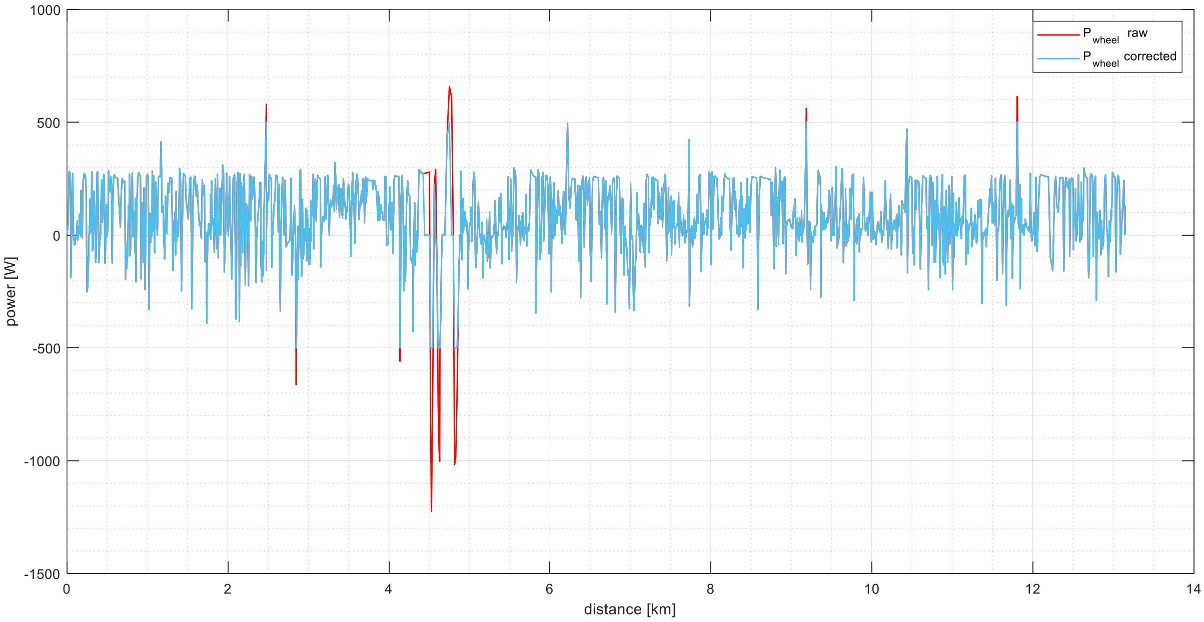

FIGURE 3-9. P_{wheel} RAW COMPARED WITH P_{wheel} CORRECTED FOR CYCLE U1

The resulting P_{wheel} is shown in Figure 3-9 and corresponds to the red plot, from which it is evident that the power required at the wheel overcome the limit imposed by the EU directive on road cycles (2.1) imposing a maximum of 250W continuous power of the pedaling assistance motor. However, it does not impose a limit on the maximum transient power, which can be assumed to be twice as much $P_{\max int} \cong 2 * P_{\max cont}$. The maximum transient torque can thus be defined as in **Eq 3-5** and the results are collected in **Errore. L'origine riferimento non è stata trovata.**.

$$T_{\max int} = \frac{P_{\max int}}{n_{base}} \text{ where } n_{base} = \frac{P_{\max cont}}{T_{\max cont}} \qquad \textbf{Eq 3-5}$$

TABLE 3-6. HYPOTHESES ON EMOTOR MAX TRANSIENT TORQUE AND POWER

$T_{m\,trans}$ **maximum eMotor transient torque**	$160\ Nm$
$P_{m\,trans}$ **maximum eMotor transient power**	$500\ W$

Having defined the maximum peak power, it is worth to notice that the resulting $P_{wheel}\ raw$ plot overcomes this limit. Additionally, by looking back to section 3.1, all the reference drive cycles reach speeds >25 Km/h, the other limit imposed by directive 2002/24/EC. As P_{wheel} deeply affects the successive steps of the modeling process, it was decided to correct $P_{wheel}\ raw$ as follows:

1. The eMotor stops assisting the rider when $V_{bike} > 25\frac{Km}{h}$. In this case P_{wheel} is set to 0
2. The eMotor maximum peak power is 500 W, so P_{wheel} is corrected as follows

$$if\ P_{wheel} > \frac{500W}{\eta_{transm}} \rightarrow P_{wheel} = \frac{500W}{\eta_{transm}}$$

$$if\ P_{wheel} < -500W * \eta_{transm} \rightarrow P_{wheel} = -500W * \eta_{transm}$$

The resulting plot is represented in blue in Figure 3-9.

Successively, the corrected P_{wheel} was elaborated to extract $P_{wheel\,nrb}$ and $P_{wheel\,reku}$, i.e., the positive power and the negative power at the wheel axle respectively. These were integrated in time domain resulting in the cumulative energy at the wheels($E_{wheel\,nrb}$ and $E_{wheel\,reku}$)and the cumulative energy at the DC bus ($E_{bus\,nrb}$ and $E_{bus\,rb}$), from which was finally derived the average power demand at the DC bus that the FCS needed to meet with and without regenerative braking, i.e., $P_{bus\,avg\,nrb}$ *and* $P_{bus\,avg\,rb}$. The above steps are summarized by the following equations, where T_{cycle} is the total duration of the driving cycle and *PS* is the power split coefficient.

Without regenerative braking:

$$E_{wheel\,nrb} = \int_0^{T_{cycle}} P_{wheel\,nrb}$$

$$E_{bus\,nrb} = \frac{E_{wheel\,nrb}}{\eta_{trans} * \eta_{eMot} * \eta_{inv}} * PS$$

$$P_{bus\,avg\,nrb} = \frac{E_{bus\,nrb}}{T_{cycle}}$$

With regenerative braking:

$$E_{wheel\,reku} = \int_0^{T_{cycle}} P_{wheel\,reku}$$

$$E_{bus\,rb} = E_{bus\,nrb} + E_{wheel\,reku} * \eta_{trans} * \eta_{eMot} * \eta_{inv}$$

$$P_{bus\,avg\,rb} = \frac{E_{bus\,rb}}{T_{cycle}}$$

EQ 3-6

As mentioned in section 2.1, the electric drive activates only when the rider is pressing on the pedals and outputs a torque proportional to the rider's. The eDrive installed on the BCargo allows the user to set this constant of proportionality, i.e., "level of assistance", from the display installed on the handlebar [25]. The "level of assistance" can thus be defined as $\frac{P_{eMot}}{P_{rider}}$, a ratio which can be re-arranged to obtain $PS = \frac{P_{eMot}}{P_{wheel}}$, the so-called power split coefficient which is more useful for the following calculations. It is important to point out that it is assumed that 100% of the recoverable kinetic energy during braking phases can always be recovered and that the battery has a unitary roundtrip efficiency, due to the lack of information on the matter.

3.3 Results & FCS selection

$P_{bus\ avg}$ was evaluated in all the possible working conditions of the eCargo, i.e., both urban and mountain cycles, with and without regenerative braking and for all the possible PS. The results are reported in **Errore. L'origine riferimento non è stata trovata.**.

TABLE 3-7. RESULTS IN TERMS OF AVERAGE POWER DEMAND

e-Motor support		Without regenerative braking				With regenerative braking			
		$P_{bus\ avg}[W]$				$P_{bus\ avg}[W]$			
Assistance level	PS	U1	U2	M1	M2	U1	U2	M1	M2
1	0.5	53	44	131	119	32	24	77	64
2	0.66	65	58	173	157	46	38	119	102
3	0.75	80	66	196	179	59	45	143	124
4	0.8	85	70	209	190	64	50	156	136
5	1	106	88	262	238	85	67	208	183

Since all FCS show a maximum operating efficiency region between 5 and 20% of their rated power (see section 2.2), the best strategy to size the FCS is to take the minimum and maximum power in **Errore. L'origine riferimento non è stata trovata.** and set them as lower bound and upper bound, respectively, of the highest-efficiency region. Considering the wide range of such powers, the selection with this approach is challenging. To simplify things and avoid oversizing of the FCS, since eCargo's mission profiles involves mainly urban areas, only the two most representative scenarios of the urban cycles were examined, i.e., the cases U2-PS=0.5 as lower bound and the case U1-PS=1 as upper bound highlighted in red in Table 3-7. From Horizon FCS manufacturer's product catalogue [27] the best FCS was then selected by comparing the two above mentioned operating points with the FCS efficiency curve obtained re-scaling the blue plot seen in Figure 2-4 to the stack's rated power. The product that showed the highest efficiency in those working points is the FCS-C1000, as it can be seen from Figure 3-10.

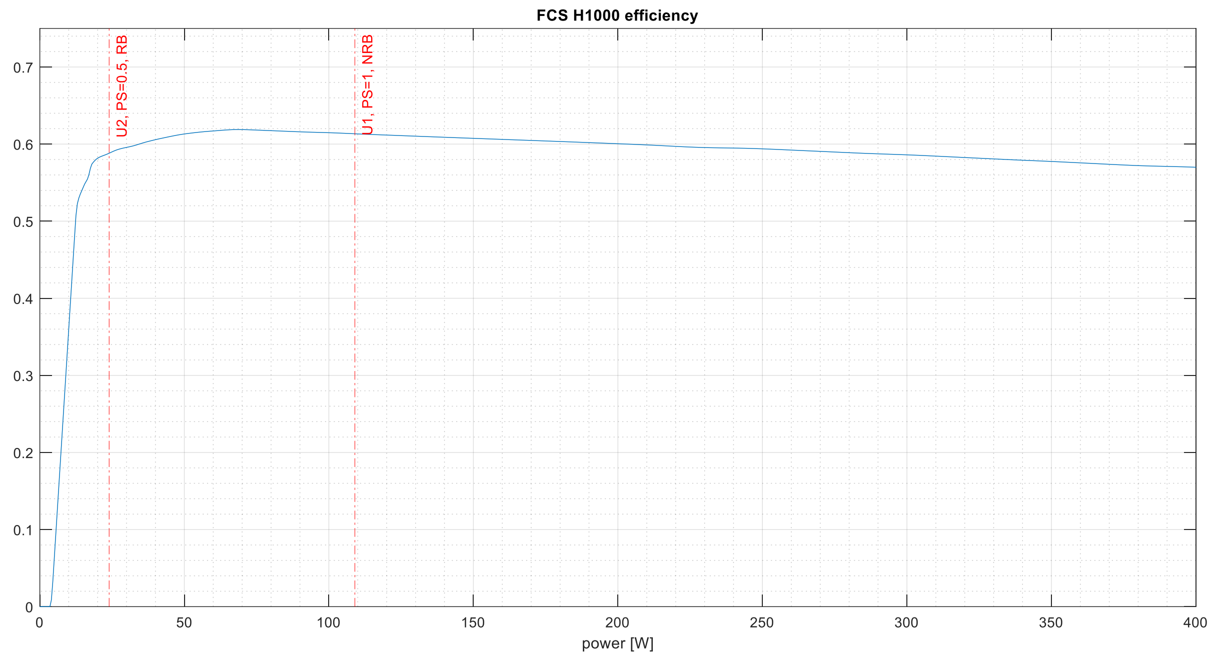

FIGURE 3-10. FCS-C1000 EFFICIENCY & LOWER-UPPER BOUNDS AVERAGE OPERATING POINTS

Nevertheless, that stack was not selected because of many reasons, namely costs, lack of detailed regulations and bulkiness. The FCS-C1000 stack's quote has not been requested yet, but was estimated to be more than 6000$ [28]. Additionally, even though the directive 2002/24/EC only mentions the 250W limit on the rated eDrive power, the single states laws are unclear on the matter and it is not known whether it would be road-legal to install a 1kW stack on a cargo bike. Finally, being the size of FCS-C1000 stack H219 x W268 x D123 mm and since Horizon's installation manual recommends keeping the air inlet perpendicular to the ground [27], it was concluded that it might take up too much vertical space inside the BCargo's trunk, penalizing the practicality of the vehicle.

Because of these issues, a 200W stack was selected: the FCS-C200. The projected cost and its height are about half of the 1kW one, saving both money and space while giving up some efficiency.

FIGURE 3-11. A PICTURE OF THE SELECTED C200 STACK

The FCS-C200 operating efficiency η_{FCS} was then calculated for all possible operating conditions to check that the performances were still acceptable.

TABLE 3-8. η_{FCS} IN ALL THE POSSIBLE OPERATING CONDITIONS

e-Motor support		Without regenerative braking				With regenerative braking			
		η_{FCS}				η_{FCS}			
Assistance level	PS	U1	U2	M1	M2	U1	U2	M1	M2
1	0.5	0.59	0.60	0.53	0.54	0.60	0.61	0.57	0.58
2	0.66	0.57	0.59	OR	0.51	0.59	0.60	0.54	0.55
3	0.75	0.57	0.58	OR	OR	0.58	0.59	0.52	0.53
4	0.8	0.56	0.57	OR	OR	0.58	0.59	0.51	0.52
5	1	0.55	0.56	OR	OR	0.56	0.58	OR	OR

In calculating the data presented in Table 3-8, an additional drawback of adopting a smaller FCS was noticed: for the M1 and M2 cycles the average power demand that must be met by the range extender is above the maximum net power output of the C200 stack; this case was reported in the table above as “OR” – Out of Range. Nonetheless, being the eCargo bike designed for last mile delivery in urban areas, cycles M1 and M2 can be considered outside of the vehicle’s mission and so it is not a problem if the eCargo bike cannot operate in charge sustaining in these scenarios. For this reason, all the next steps in the eCargo dynamic modeling were performed using only the U1 and U2 cycles as input.

The final step of the quasi-static simulation was evaluating the vehicle performance. The results are reported in tables below.

TABLE 3-9. OVERVIEW OF ENERGY CONSUMPTION RESULTS

Quasi-static simulation: energy consumption [Wh/Km]																	
PS	Battery only		with 100% regenerative braking				with FCS range extender				FCS range extender + 100% regenerative braking			
	U1	U2	U1		U2		U1		U2		U1		U2	
0.5	3.8	3.4	2.3	-40%	1.8	-46%	6.1	+62%	5.6	+66%	3.5	-6%	2.8	-17%
0.66	5.0	4.4	3.5	-30%	2.9	-35%	8.4	+68%	7.3	+65%	5.8	+17%	4.5	+2%
0.75	5.6	5.0	4.2	-26%	3.5	-31%	9.6	+71%	8.4	+66%	6.7	+20%	5.6	+10%
0.8	6.0	5.4	4.5	-25%	3.8	-29%	10.3	+71%	9.1	+68%	7.7	+28%	6.3	+17%
1	7.5	6.7	6.0	-20%	5.2	-23%	13.2	+75%	11.5	+71%	10.3	+37%	8.7	+29%

TABLE 3-10. OVERVIEW OF THE POWERTRAIN EFFICIENCY

Quasi-static simulation: powertrain efficiency [-]						
PS	Battery only (benchmark)		with FCS range extender			
	Urban 1	Urban 2	Urban 1		Urban 2	
0.5	0.87	0.87	0.56	-35%	0.57	-34%
0.66	0.87	0.87	0.54	-37%	0.56	-36%
0.75	0.87	0.87	0.54	-38%	0.55	-36%
0.8	0.87	0.87	0.54	-38%	0.54	-37%
1	0.87	0.87	0.52	-40%	0.54	-38%

TABLE 3-11. OVERVIEW OF THE RESULTS IN TERMS OF RANGE EXTENSION

Backward: range [km]														
PS	Battery only		With 100% regenerative braking				With fcs range extender				Fcs range extender + 100% regenerative braking			
	U1	U2	U1		U2		U1		U2		U1		U2	
0.5	133	149	220	+65%	277	+108%	410	+208%	450	+238%	709	+433%	899	+576%
0.66	101	113	144	+43%	174	+72%	300	+197%	343	+240%	433	+330%	553	+449%
0.75	89	99	120	+36%	143	+62%	260	+193%	300	+238%	371	+318%	450	+407%
0.8	83	93	110	+33%	131	+57%	244	+193%	277	+233%	325	+291%	400	+381%
1	67	74	83	+25%	97	+45%	190	+186%	218	+228%	244	+266%	288	+332%

From the results studies is already evident that the FCS hybridization is very effective in increasing the eCargo's range, which is deemed to increase to at least +186% of the benchmark. However, it is important to point out that an FC hybrid powertrain has an overall lower efficiency with respect to a battery electric one because of the intrinsic losses inside the fuel cell itself. This is evident in Table 3-9 and Table 3-10, where the equivalent energy consumption more than doubles because of the sharp reduction in overall powertrain efficiency. Notwithstanding these observations, the results for the configuration FC hybrid eCargo with regenerative braking capabilities present the best compromise in terms of range extension and energy efficiency. The minimum range extension achieved for this configuration is +266% while the equivalent energy consumption increments are halved with respect to the hydrogen eCargo without regenerative braking.

4 Bill of material & dynamic model

Having defined the FCS for the hybridization, from its technical specification was possible to select all the other powertrain components and the hybridization architecture: a process that was rather recursive, as the one part influenced the other and vice versa due to components availability. Once the design and all parts were frozen, the forward modeling phase was carried out to estimate the same vehicle performance introduced in section 3.3 with a higher fidelity.

This chapter has the double aim to illustrate thoroughly the main components for the H_2 eCargo bike while designating how each part was modeled within the dynamic Simulink model. The first section gives an overview of the two Simulink models created to evaluate the future prototype performance and compare it with the benchmark, i.e., the original battery electric eCargo.

4.1 eCargo Simulink model: an overview

The dynamic modeling and simulation phase was carried out on Matlab/Simulink environment from a Matlab LiveScript "eCargo_main.mlx" from which it was possible to initialize the simulation and postprocess the output. The initialization part is very similar to the one used in previous chapter for backward modeling except for the computation of *EM*, the extra mass introduced for the hybridization. As a lot more information on the weight of the hybridization unit was at this point available, *EM* was estimated as follows.

$$EM = m_{batt} + m_{FCS} + m_{H_2} + m_{boards} + m_{wiring} - m_{bosch} \quad \textbf{EQ 4-1}$$

Where each mass is reported in the table below.

TABLE 4-1. ESTIMATED MASS OF HYBRIDIZATION UNIT

m_{batt} **hybridization battery mass**	1.6 kg
m_{FCS} **fuel cell system mass**	2.6 kg
m_{H_2} **hydrogen feed circuit and supply mass**	2.1 kg
m_{boards} **electronic boards & power converter mass**	0.8 kg
m_{wiring} **power & signal wiring mass**	0.7 kg
m_{bosch} **original BCargo's BOSCH PowerPack battery mass [29]**	2.7 kg
TOT	5.1 kg

Concerning m_{batt}, m_{FCS}, and m_{H_2} information were found in the product datasheet and further details will be discussed in the relative sections, on the other hand m_{boards} and m_{wiring} are reasonable estimates.

As many key drivetrain's components of the hybrid eCargo were changed with respect to the benchmark, two Simulink model reproducing the benchmark eCargo and the FC hybrid version had to be built. Both simulations could be launched from the "eCargo_main.mlx" file. The bike was modeled on Simulink environment through Simscape physical modeling, an approach that allowed to simplify greatly the construction of the model.

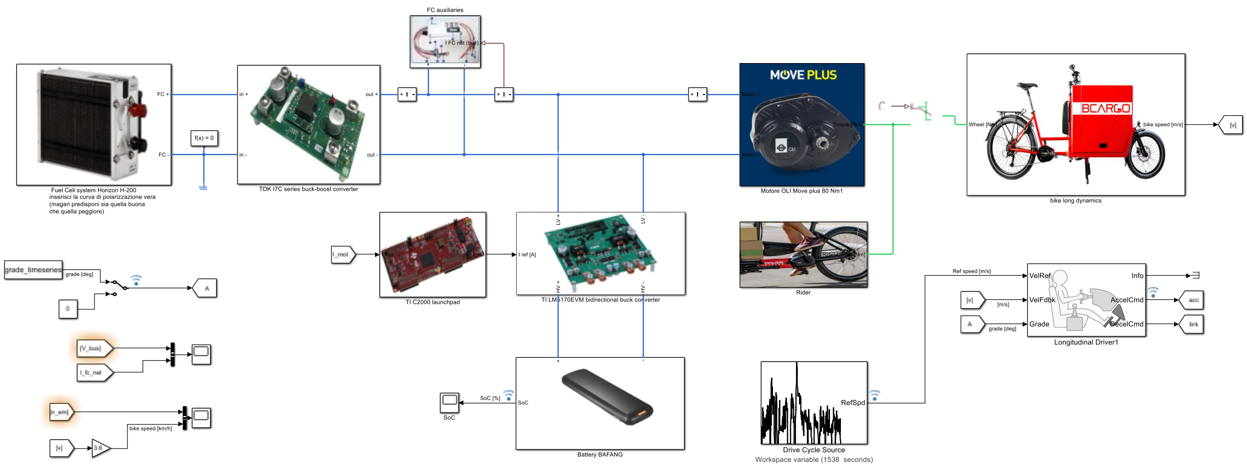

FIGURE 4-1. THE FC HYBRID ECARGO MODEL

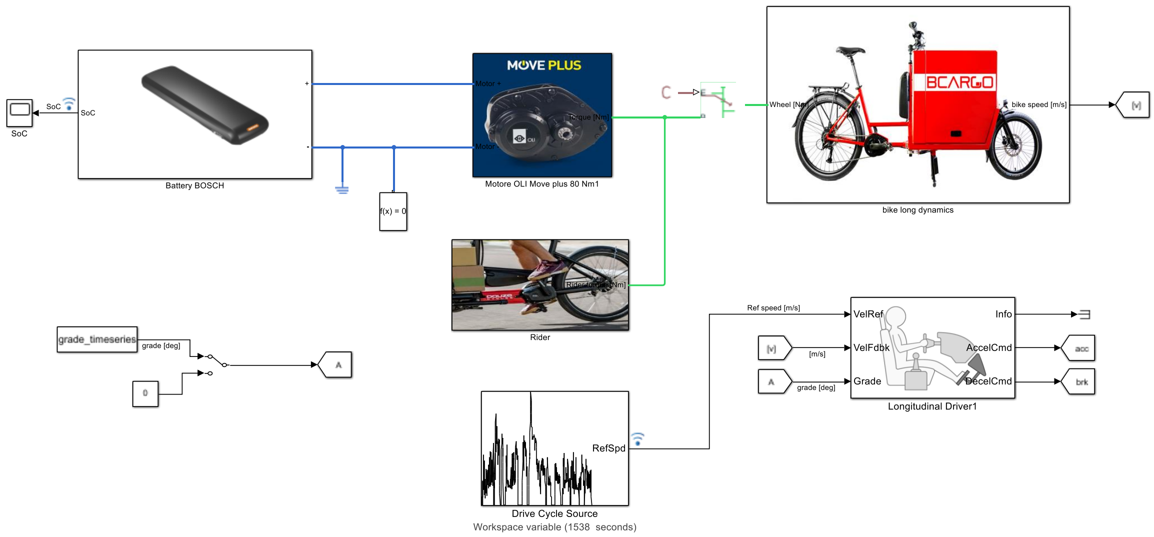

FIGURE 4-2. THE ORIGINAL BATTERY ELECTRIC ECARGO MODEL

The two models are substantially equivalent up to the DC-bus part, where for the battery electric version only the battery subsystem is present whilst for the FC hybrid version there are more subsystems modeling the various power converters, FC auxiliaries and the FC itself. Every part's model is included inside a subsystem correlated with a picture to keep everything neat.

As described in section 2.4, the difference between the previous phase of quasi static modeling and this phase of dynamic modeling is related to the information flow between blocks and the presence of a "driver" model in the latter phase, which tracks the speed driving cycle by sending acceleration signals to the eMotor model, where they are translated to a torque setpoint for the latter. For the purposes of this work, a *longitudinal driver model* block from the Powertrain blockset on Simulink was employed.

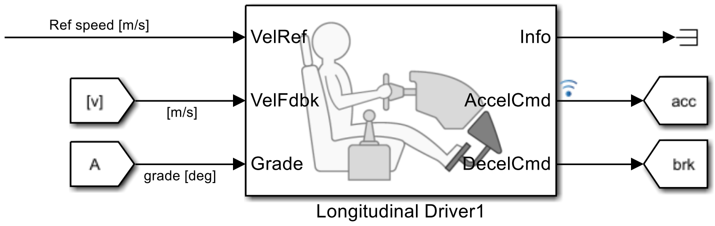

FIGURE 4-3. LONGITUDINAL DRIVER MODEL

The block sends also braking signal, to ensure speed tracking during deceleration phases, and can be potentially set to transmit gear signals in case the modeled vehicle had a gearbox and the driving cycle included a gear-shift profile [30], which is not the situation for the vehicle under study. Both acceleration and braking commands are normalized; denormalization is performed inside the subsystems the signal is routed to. Acceleration commands are routed to the eMotor subsystems while braking commands are routed to the latter, enabling regenerative braking, and to the "bike longitudinal dynamics" subsystem, to model the bike's brakes.

In the "bike longitudinal dynamics" subsystem, the BCargo's longitudinal dynamic was modeled with a *longitudinal vehicle 1* block from Simscape's Driveline blockset. The longitudinal vehicle's torque and force balance is reproduced inside this block with the following equation:

$$m\frac{dV}{dt} = \frac{T_{wheel}}{r_l} - F_b \tanh\left(\frac{\omega_{wheel}}{\omega_1}\right) - \left(C_r * mg * \cos(\theta) + \frac{1}{2}C_d A_f \rho_{air} V^2\right) * \tanh\left(\frac{V}{V_1}\right) - mg * \sin(\theta)$$

EQ 4-2

Where:
$m = bike\ mass$
$V = bike\ speed$
$r_l = wheel\ radius$
$T_{wheel} = wheel\ torque$
$F_b = braking\ force$
$C_r = rolling\ coefficient$
$\theta = road\ angle$
$C_d = drag\ coefficient$
$A_f = frontal\ area$
$g = gravity\ constant$
$\rho_{air} = air\ density$
ω_1 , V_1 $arbitrary\ constants\ for\ braking,\ rolling\ and\ aerodynamic\ force\ suppression\ range$

The block represents an abstract vehicle confined to longitudinal motion. It is possible to parameterize an arbitrary vehicle or choose from predefined parameterizations. The block includes optional non-slipping tires and ideal brakes [30], which were both used for the eCargo.

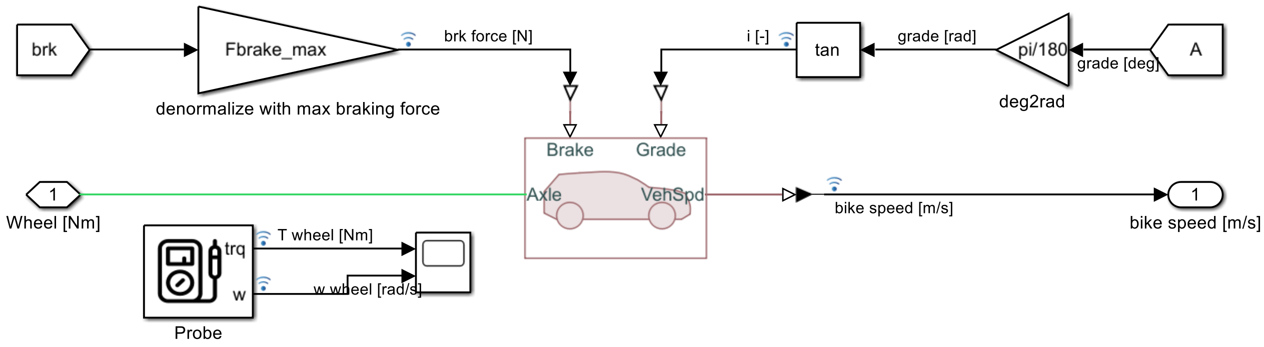

FIGURE 4-4. BIKE LONGITUDINAL DYNAMICS MODEL

The *longitudinal vehicle 1* block at the center of Figure 4-4 receives a mechanical rotational signal from the bike's transmission model, which is a Simscape physical signal embedding both rotational speed for the wheel hub and torque applied, positive or negative. The brake force signal simulates the ideal braking action performed by the bike during decelerations and it originates from the driver's model block. As in the backward model, road grade is imported under the form of $i\ [-]$, which is a conventional way of expressing the road inclination angle as a ratio [31]. The only output is the physical signal of the bike speed, which is fed back to the driver model to perform speed tracking.

The physical signal for torque-speed at the wheel hub originates from the eMotor and the rider subsystems. While in the backward model the eMotor assistance level was taken into account by simply multiplying the DC-bus output energy by PS (see Eq 3-6), the only way to account for it in the forward model is to include a rider's model that provides for a portion of the torque demand as a function of PS.

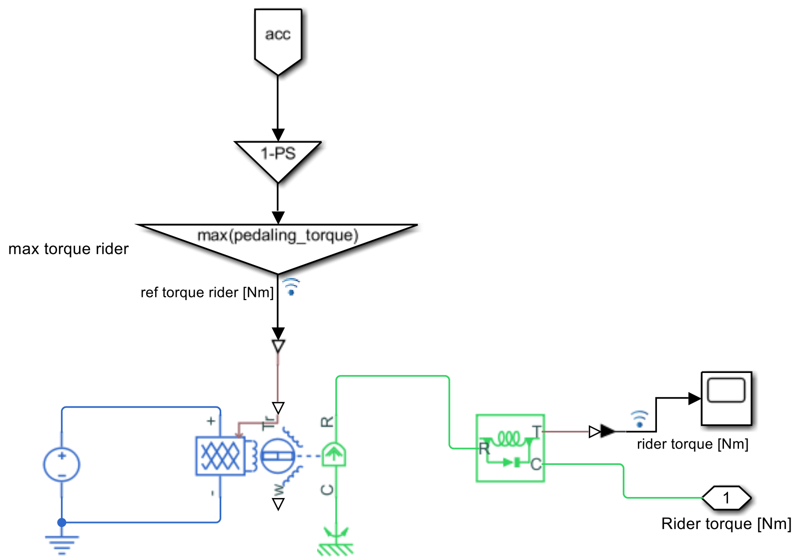

FIGURE 4-5. RIDER MODEL

The rider model is enclosed within the homonymous subsystem and it is mainly based on a *Motor & drive (system level)* connected to the torque-speed signal bus in parallel with the electric motor model and fed by a *DC voltage source* block. The voltage source block acts like an ideal voltage source, it does not have a physical meaning, but it is solely used for modeling purposes by feeding the required energy to the attached motor block reproducing the rider's torque-speed characteristic curve. The latter was extracted from the work by Abbiss et al. where a plot of the relationship between peak crank torque, crank velocity (i.e. cadence) and power output during short duration (<10s) maximal cycling in two separate subjects (solid and dashed lines), both athletes [32]. These curves are represented in Figure 4-6.

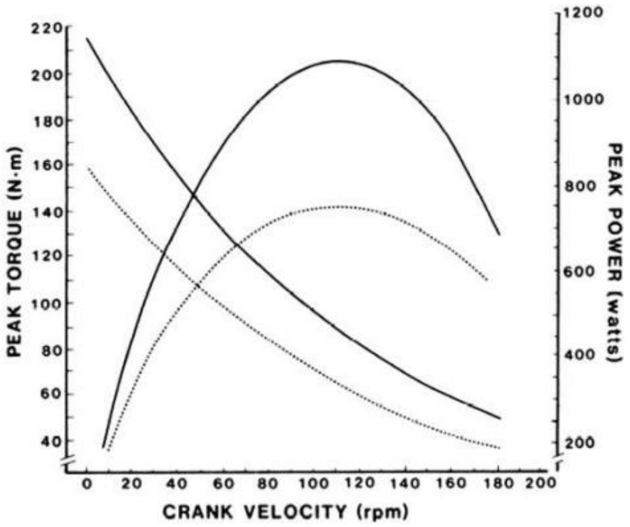

FIGURE 4-6. PEAK CRANK TORQUE VS CRANK VELOCITY IN TWO SUBJECTS

To keep a high fidelity, the curve exhibiting lower torque was taken as reference. This data was extracted and saved in matrix from by means of the Grabit tool [33]. The matrix was then fed to the *Motor & drive (system level)* block as to parametrize its torque-speed envelope. Triggered by the input <u>ref torque rider</u> signal (Figure 4-5), the block generates a torque as a function of the output shaft speed such as the operating point of the system is enclosed by the torque-speed envelope.

On the other hand, the actual eDrive system was modeled through the same *Motor & drive (system level)* block which was parametrized with the maximum torque and power, both continuous and transients. These values are then used to build the respective torque-speed envelopes within the block itself, which allows to over-torque the motor drive if the torque demand has been less than the continuous operation torque envelope for more than the value specified in the **recovery time** parameter, i.e., 300 s. Over-torquing is disabled if it has been applied for longer than the value specified in the **over-torque time limit** parameter [30], which was set to 300 s as well. The electrical losses were parametrized by an efficiency 2D lookup, which was created in such a way that the eDrive efficiency is constant and equal to $\eta_{eMot} * \eta_{inv} = 0.9$ (Table 3-4). The resulting torque, speed and efficiency envelope is shown in Figure 4-7.

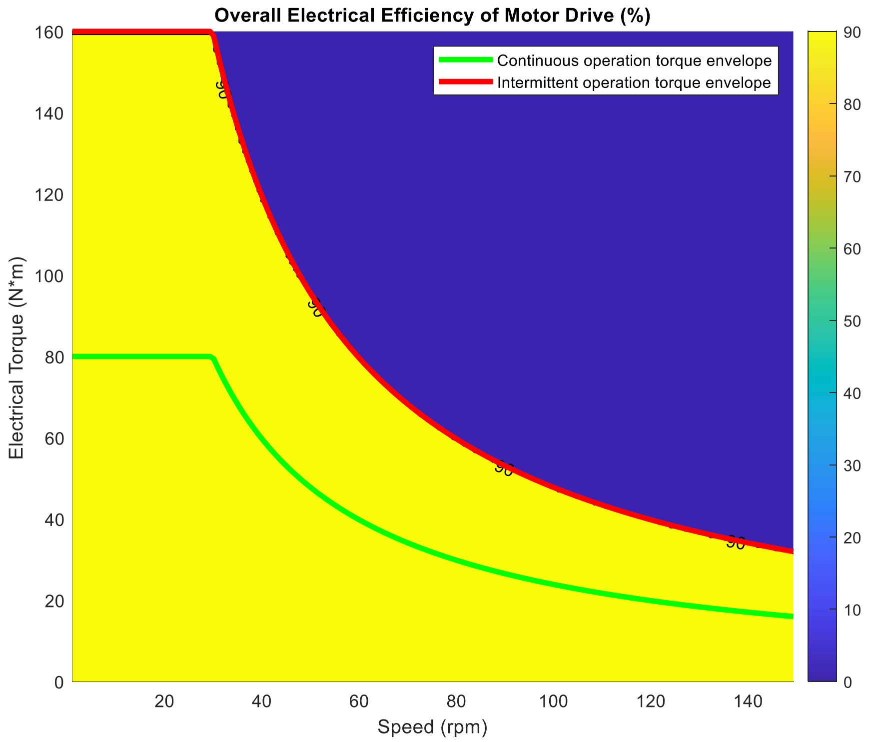

FIGURE 4-7. EDRIVE EFFICIENCY MAP & TORQUE-SPEED ENVELOPES

The rest of the model works in a very similar fashion to the rider's model: the acc signal is denormalized with the *PS* coefficient and the max transient torque value. The main difference is the presence of the "regenerative braking management" subsystem which will be explained later.

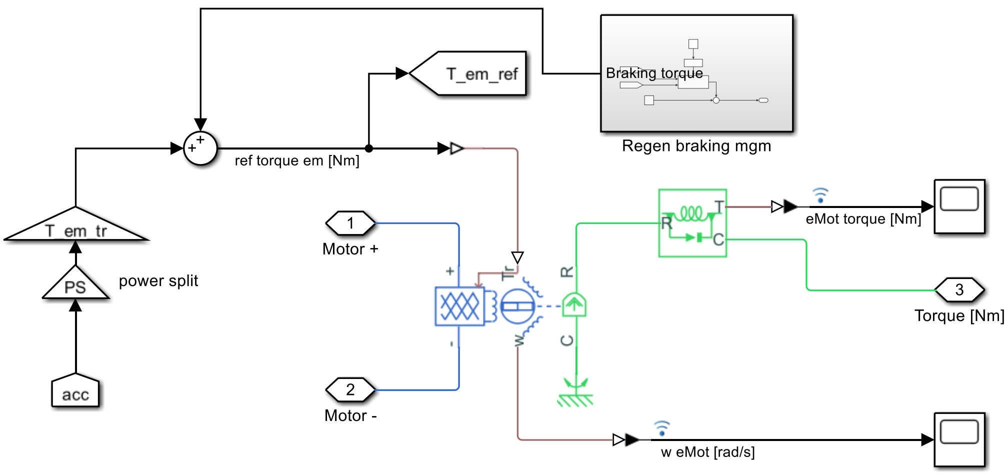

FIGURE 4-8. EMOTOR MODEL

The regenerative braking is generally implemented by sending a negative Tr signal to the *Motor & drive (system level)* block, in which case the modeled motor acts as generator sending back current to the DC bus. However, it was noticed that during harsh braking conditions, even with a state of charge (SoC) of 60%, the battery voltage V_{batt} overcame the maximum allowable battery voltage $V_{batt\ max}$, an issue that would rapidly lead to a dangerous breakdown of the battery. The solution hereby proposed is based on a z-shaped membership function inspired from fuzzy logic that smoothly inhibits the regenerative braking action when a certain threshold is overcome. The block diagram of the controller is shown in Figure 4-9.

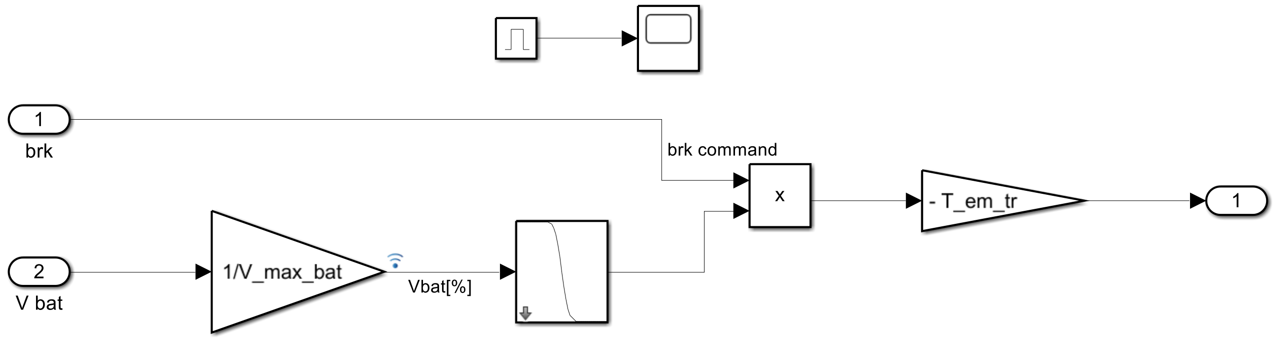

FIGURE 4-9. REGENERATIVE BRAKING CONTROLLER

In particular, V_{batt} signal is normalized with $V_{batt\,max}$ and fed to the z-membership function block, which output is 1 until $V_{batt} > V_{batt\,max} * 0.98$, then the output transitions to 0. The z-function is described in Figure 4-10.

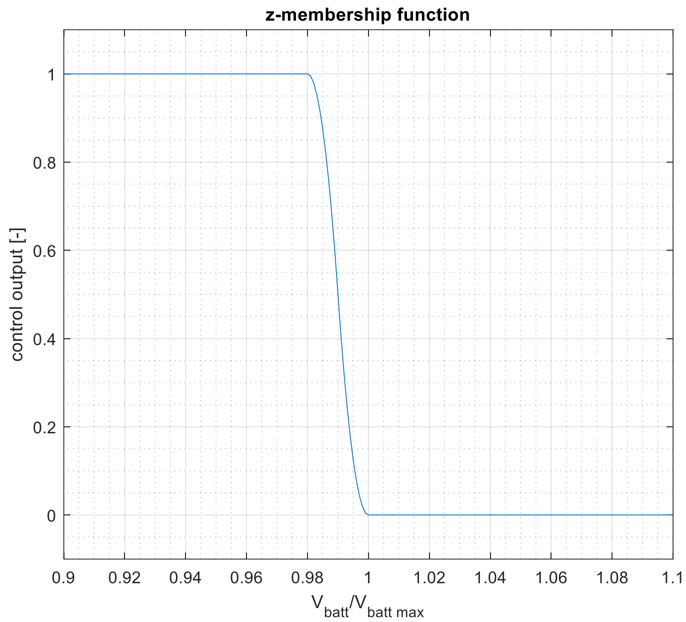

FIGURE 4-10. Z-MEMBERSHIP FUNCTION IN REGENERATIVE BRAKING MANAGEMENT

The z-function output is multiplied by the braking action signal (brk)coming from the driver's model and effectively inhibits it when needed.

Finally, the only missing part of the model that should be described in this chapter is the *simple gear with variable efficiency* block lying on the torque-speed bus connecting the drive models and the longitudinal dynamics subsystem, as pictured in Figure 4-1.

Even though the original BCargo is endowed with a 9-speed Shimano derailleur [24], it was decided not to include it into the forward simulation because of several reasons. First, the actual transmission ratios were not known, nor the efficiency for each gear. Secondly, even if a gearbox were included in the model, a gear shift profile relative to the reference driving cycles would also be needed, meaning that further experimental campaigns on the matter should be conducted. At last, the original Shimano transmission does not allow regenerative braking due to presence of the free wheel pinion on the rear wheel.

Being regenerative braking a big portion of this feasibility study, it was decided to simply model the transmission as a 1-speed gearbox with a certain transmission ratio τ that was evaluated as follows. First, the maximum vehicle speed $V_{bike\ max}$ on flat road was computed by re-arranging the power balance equation (**Eq 3-1**) and setting $P_{wheel} = P_{m\ cont} * \eta_{trans}$ and $\alpha = 0$, i.e., flat road.

$$\frac{1}{2} * \rho * V^3 * C_x * S_{tot} + m * g * f * V - P_{\mathrm{m}\,cont} * \eta_{trans} = 0$$

EQ 4-3

Solving for V the resulting maximum vehicle speed was found $V_{bike\ max} = 24\ Km/h$. Secondly, τ was calculated so that the bike would reach $V_{bike\ max}$ at the maximum eMotor speed $n_{max} = 120\ RPM$ [25].

$$\tau = \frac{n_{max} * \frac{\pi}{30} * r_l * 3.6}{V_{bike\ max}} = 0.63 \qquad \textbf{EQ 4-4}$$

$\tau\ and\ \eta_{trans}$ were then fed to the *simple gear with variable efficiency* block as parameters (Figure 4-11).

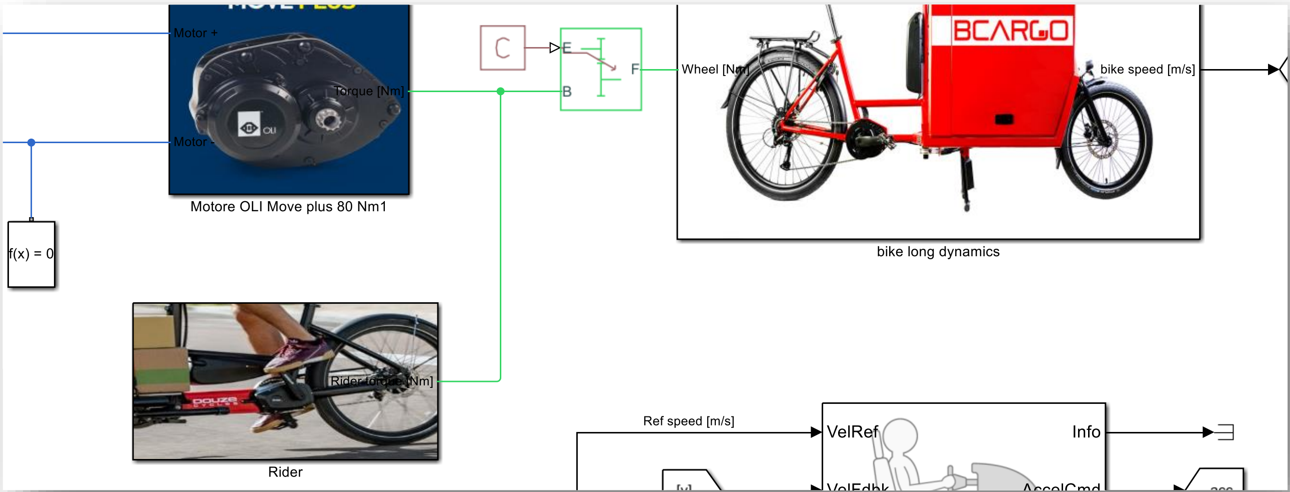

FIGURE 4-11. TRANSMISSION MODEL

The *simple gear with variable efficiency* block represents a simple gear train with variable meshing efficiency. The gear train transmits torque at a specified ratio between base and follower shafts arranged in a parallel configuration. Shaft rotation was set to occur in equal directions. To specify the variable meshing efficiency, the block contains a physical signal port that is used to input the desired transmission efficiency. Inertia and compliance effects are ignored [30].

4.2 Fuel cell system & hydrogen feed system

In this section further insight on the selected FCS is given, together with the description of how the FC stack and its auxiliaries were modeled. The section concludes with description of the selected components for the hydrogen feed system and the motives behind these choices.

4.2.1 Horizon H200 technical specifications and modeling

Horizon's FCS-C200 is a commercial open-cathode PEMFC stack system. It comes complete with its auxiliaries and a proprietary controller for managing them. The auxiliary systems include the fan blower, the short circuit unit, and the H_2 purge valve which keep the proton exchange membrane humidified just right to ensure the best performances. Being the H200 an "open cathode" fuel cell (see section 2.2), the blower forces air through the stack providing air both for cooling and the reaction. Knowing the FCS technical specifications, it is possible to define all the other powertrain components' specification in a cascade fashion. The most important technical specifications are reported in Table 4-2 while the FC polarization curve is found in Figure 4-12. Further details on the FCS operation and installation can be found in the user manual [34].

TABLE 4-2. FCS-C200 TECH SPEC [34]

Number of cells	40
H_2 working pressure	$0.45 - 0.55$ bar
Stack weight (with fan & casing)	2230 ± 50 g
Controller weight	400 ± 50 g
Dimension	11.8 cm × 18.3 cm × 9.4 cm
Low voltage shut down	20 V
Overcurrent shut down	12 A
Controller power supply	13 ± 1 V

The polarization curve was extracted from the H200 user manual through the Grabit tool [33] and was stored in a vector. The stack efficiency was also computed using Eq 2-4.

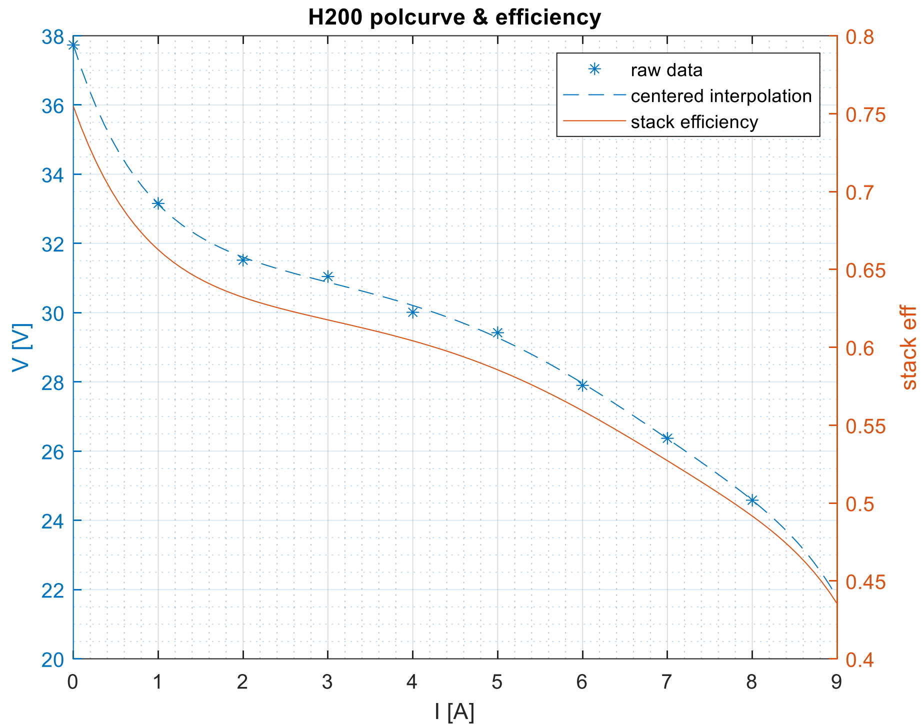

FIGURE 4-12. H200 POLARIZATION CURVE & STACK EFFICIENCY η_{stack}

The modeling of the H200 was quite a challenge. The first approach was to use the *fuel cell* block in Simscape electrical blockset, which models the FC as the equivalent circuit below.

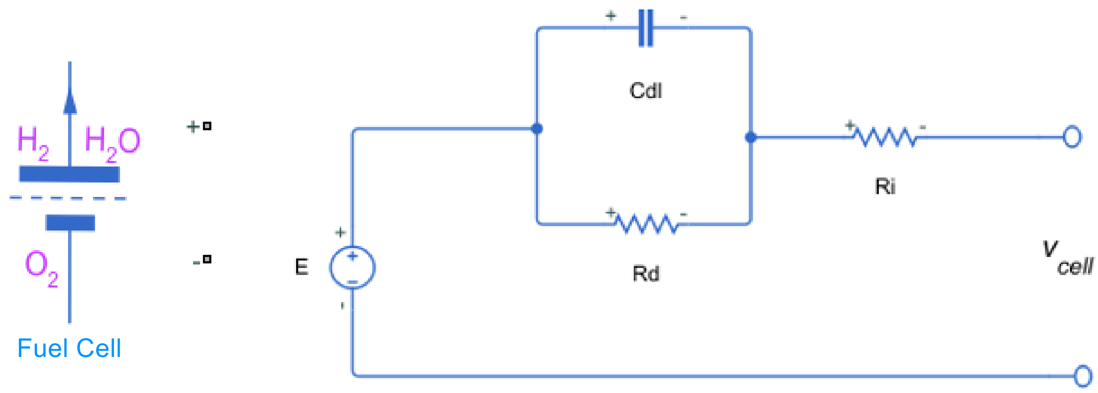

FIGURE 4-13. FUEL CELL BLOCK AND EQUIVALENT CIRCUIT

where:

- V_{cell} is the cell voltage.
- R_i is the Internal resistance.
- R_d is the Sum of activation and concentration resistances.
- C_{dl} is the parallel RC capacitance that accounts for time dynamics in the cell.

As no information on R_i, R_d, and C_{dl} are available from Horizon, it was decided to create a quasi-static model from its polarization curve by creating a 1D lookup table which outputs the FC voltage V_{FC} as a function of the load current $I_{FC\ gross}$.

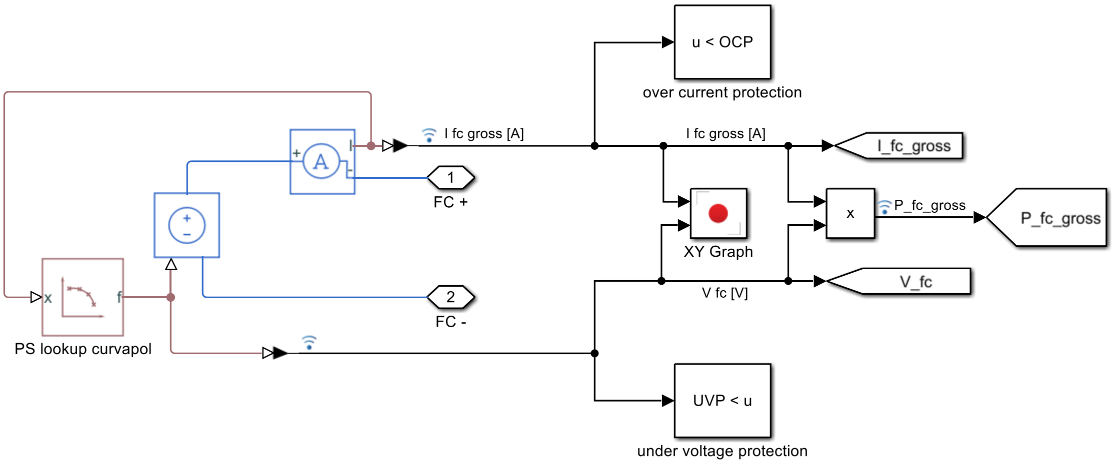

FIGURE 4-14. H200 STACK MODEL

As shown on the left of the figure above, $I_{FC\ gross}$ is fed back to the *PS lookup table (1D)* block which outputs the corresponding V_{FC} based on based on the input values using the selected interpolation and extrapolation methods, "linear" and "nearest" respectively [30]. The lookup table output drives a *controlled voltage source* block that imposes V_{FC} to the electrical conserving ports FC+ and FC-, which act very much like a real-world electrical circuit. The stack's undervoltage and overcurrent protections were also modeled as Simulink's *assertion* blocks, yielding a warning in case the voltage went below threshold or the current went above it.

Regarding the FCS auxiliaries, they significantly affect the overall FCS efficiency η_{FCS} (see section 2.2) and so they had to be included in the dynamic model in some way. The final solution involved again a lookup table block reproducing the relationship between the power drawn from the auxiliaries P_{aux} as a function of the net FCS output power measured on the DC-bus P_{net}.

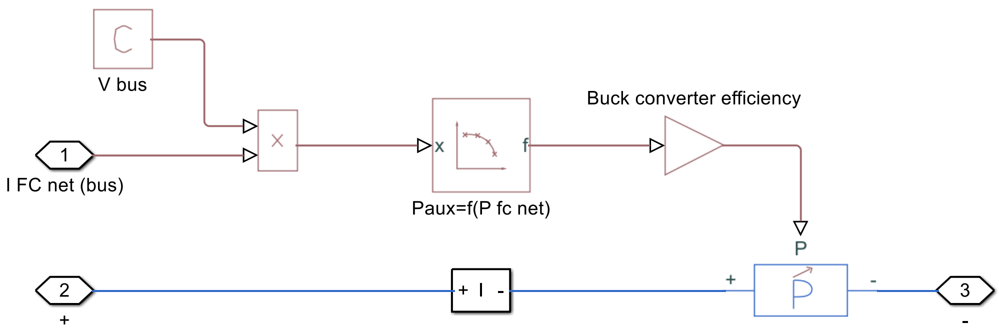

FIGURE 4-15. FCS AUXILIARIES MODEL

The lookup table was again modeled with the *PS lookup table (1D)* block receiving P_{net} as an input which in turn is obtained multiplying the $I_{FC\ net}$ signal, fed back from a current sensor on the bus, and the bus reference voltage V_{bus}. The table output P_{aux} is divided by the buck converter efficiency and the result is fed to a *dynamic load* block which imposes a load equivalent to the input signal [30] on the DC-bus.

The relationship $P_{aux} = f(P_{bus})$ was obtained starting from Eq 2-5 and substituting $P_{stack} = P_{net} + P_{aux}$ as summarized in the following equations.

$$\eta_{aux} = \frac{\eta_{FCS}}{\eta_{stack}} = \frac{P_{net}}{P_{net} + P_{aux}} \qquad \textbf{Eq 4-5}$$

Which by solving for P_{aux} becomes

$$P_{aux} = \frac{P_{net}}{\eta_{aux}} * (1 - \eta_{aux}) \qquad \textbf{Eq 4-6}$$

η_{aux} was found according to **Eq 4-5** (see Figure 2-4) and from it the raw P_{aux} was calculated. An asymptotical behavior near the ends of the working FC net power region was observed, which does not make physical sense but it is most likely related to the poor resolution of the experimental data from which η_{FCS} was extrapolated [14]. It was thus decided to saturate P_{aux} to its minimum and maximum. The results can be seen in the next figure.

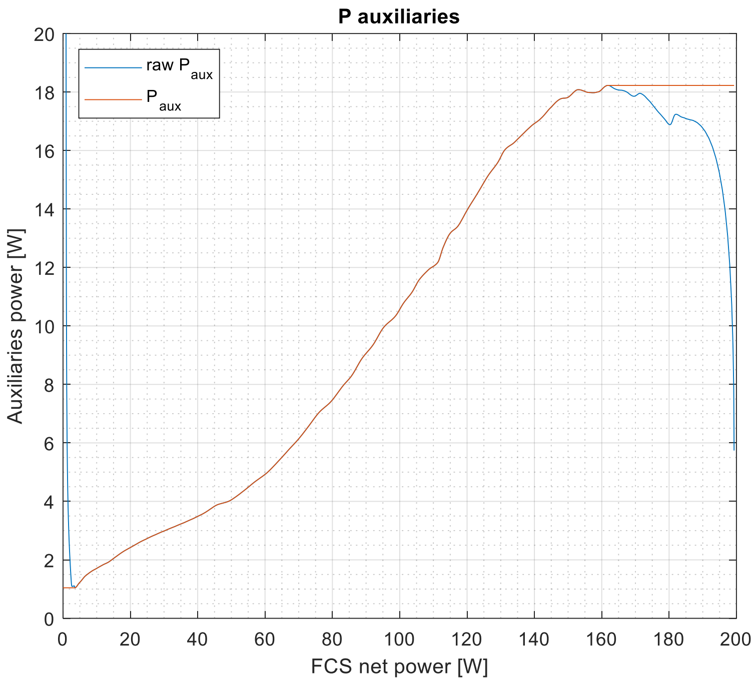

FIGURE 4-16. $\boldsymbol{P_{aux} = f(P_{bus})}$

4.2.2 Hydrogen feed system

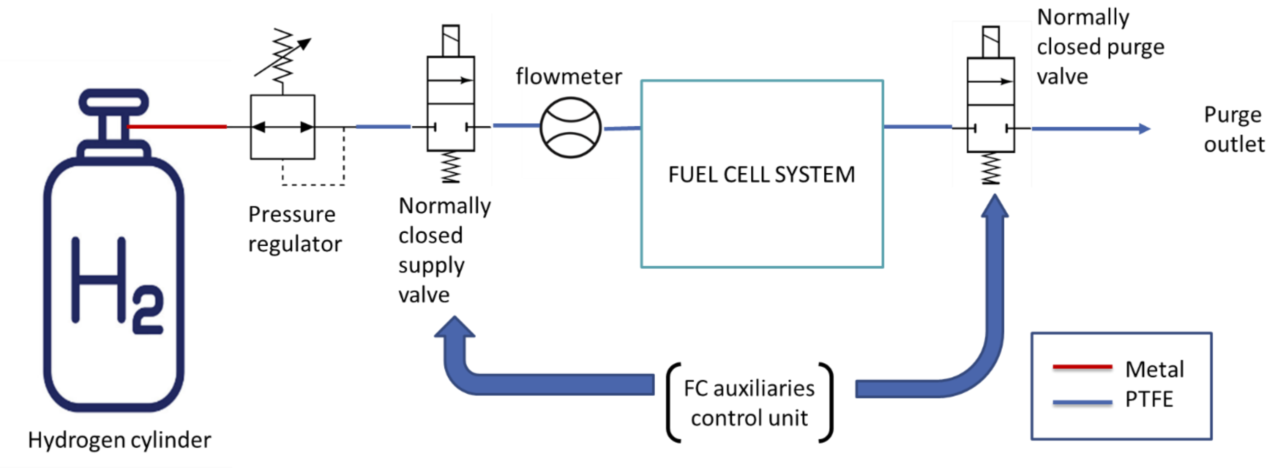

FIGURE 4-17. H_2 CIRCUIT SCHEMATIC

The final design of the hydrogen feed circuit for the hydrogen BCargo prototype is shown in Figure 4-17 and it is composed mainly of the hydrogen cylinder, a pressure regulator, a normally closed supply valve, a flowmeter, and a purge valve. The two valves are included into the H200 package, they are normally closed and are controlled by the FC auxiliaries control unit together with the stack blowers. Additionally, the tubing from the pressure regulator to the purge outlet are made of PTFE, a material that is inert to hydrogen, and comes with the H200 as well [34].

A hydrogen capacity target of 900 Nl was set for the hydrogen cylinder, in order to be consistent with the HydroCargo project [8]. The final choice fell on the F3 cylinder among the F-series vessels by HES, which is a composite, 300 bar cylinder [35]. It comes fully equipped with a pressure regulator integrated with hydrogen fill port, manual shutoff valve, high pressure gauge, and a pressure transducer on request [36], which could be easily linked with the bike's control board to implement a "fuel gauge". The main technical specifications are summarized in Table 4-3.

TABLE 4-3. HYDROGEN CYLINDER & PRESSURE REGULATOR TECH SPEC

Water capacity	3 L
Dimensions (excl. pressure regulator)	Ø: 122 mm L: 440 mm
Max pressure	350 bar
Max flow	< 50 slpm
Outlet pressure	0.5 to 1 bar (adjustable)
Outlet connection	1/8" NPT
Total weight (incl. pressure regulator)	2.1 kg

The next part that is worth to mention is the flowmeter, which purpose is to record the hydrogen consumptions when the BCargo prototype will be tested on the road. A Vögtlin *red-y compact 2 series* flowmeter was selected because of the high precision MEMS technology (CMOS sensor) in a user-friendly device thanks to the built-in touch display [37]. The device is very compact, can be installed in any position, it is AA battery powered, and is immediately ready for operation.

Additionally, it can display the total consumption which is the most useful characteristic for the purposes of this work. The most relevant technical specifications are reported in Table 4-4.

TABLE 4-4. FLOWMETER TECH SPEC

Ports	1/4" F G
Measuring range	0-6000 mNl/min

4.3 Powertrain electrical layout & components

According to section 2.3, the "textbook" hybridization layout for the future BCargo prototype consists into the H200 connected downstream to a DC/DC converter which in turn is connected to the eDrive DC-bus in parallel with the battery, as shown in Figure 4-18. The FC auxiliaries could also be connected to the DC-bus through another power converter keeping a reference output voltage of 13 V also during FCS startups or shutdowns, i.e., when the FCS cannot self-sustain its auxiliaries.

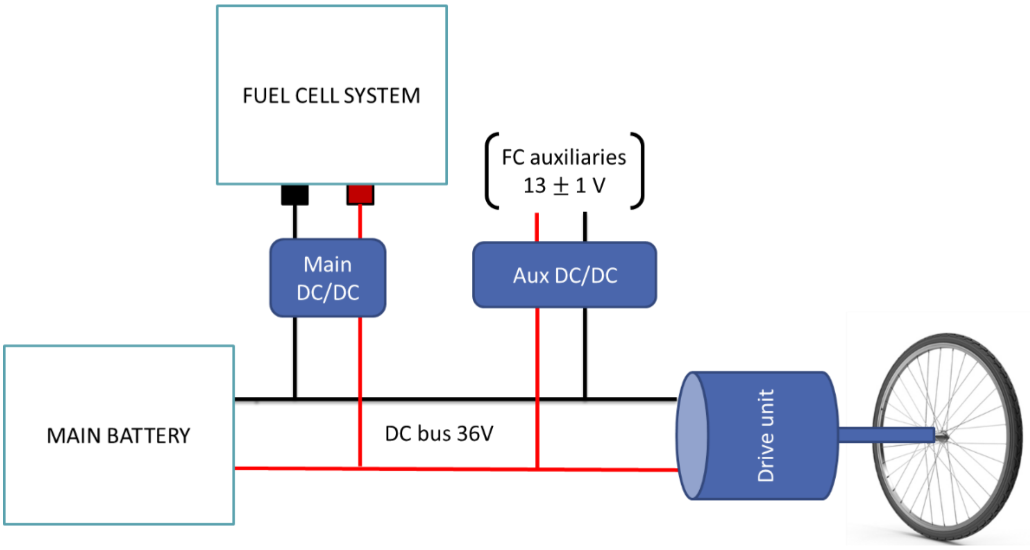

FIGURE 4-18. BASIC HYBRIDIZATION LAYOUT FOR THE HYDROGEN BCARGO

Nevertheless, this configuration complicates greatly the power split control between FC and battery, of which the *Main DC/DC* should be in charge. In order to keep a set power flowing out of the FC to the DC-bus, such device should be able to control the output current as a function of the bus voltage. The latter is driven by the battery terminals' one and fluctuates according to SoC and battery current, making impossible to manage the power split by simply controlling the DC/DC output current. Furthermore, the power through the main DC/DC should account for the power drawn from the auxiliaries to track accurately the reference power that must be delivered to the bus, as set by the EMS. This second matter is particularly challenging because one would need accurate knowledge on the power drawn by the auxiliaries as a function of the FCS output power to make this layout work properly. These issues were deemed too complex to address, so the author came up with a second layout which is more complex than the first but simplifies greatly the power split management.

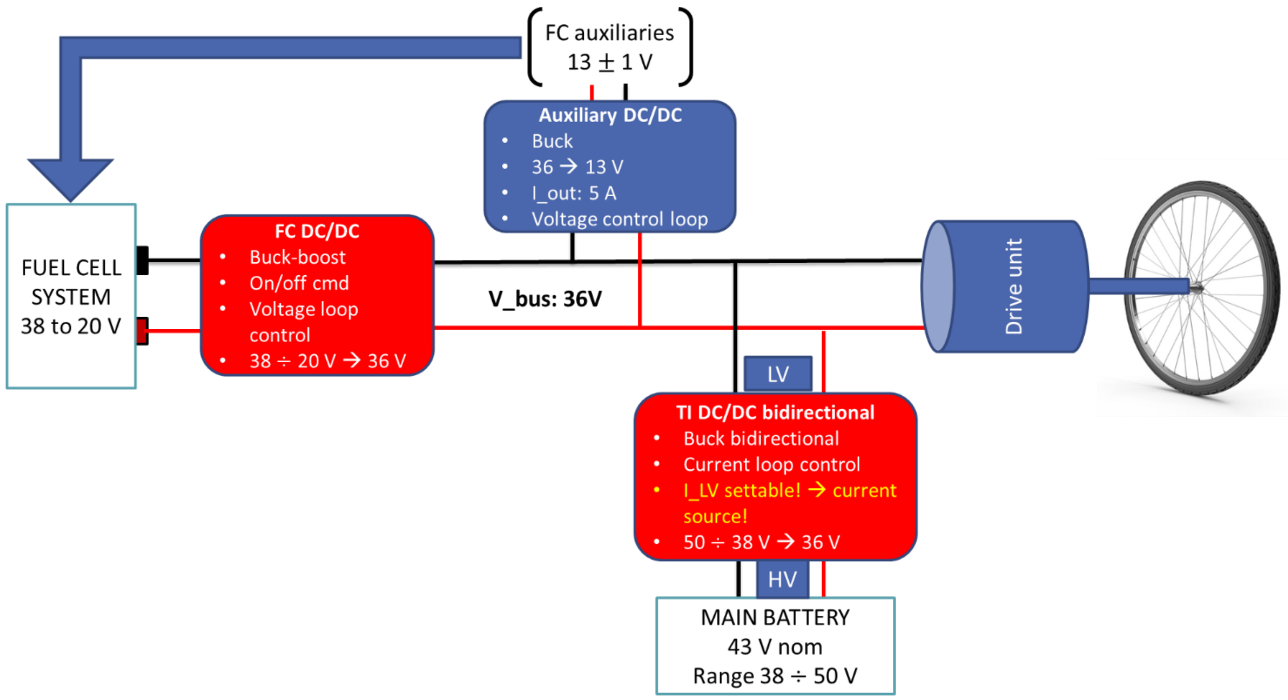

FIGURE 4-19. FINAL HYBRID POWERTRAIN LAYOUT

The main difference with respect to Figure 4-18 is the presence of a second DC/DC converter on the battery side of the bus, which transformed the layout into a compromise solution between *c* and *d* in Figure 2-8. In this case the buck-boost converter on the FC side keeps the DC-bus voltage to a quasi-stable 36 V, i.e., the rated eDrive voltage, allowing to perform an effective power split control by setting the current of the battery DC/DC. This is easily done with a current-loop bidirectional converter.

More specifically, the controller board should receive in input:

- The eMotor torque or current (according to how the eDrive is designed) to estimate the power demand P_{dem}.
- The battery voltage, to perform some basic battery management functions such as keeping $V_{batt} < V_{batt\ max}$.
- The battery SoC, one of the basic inputs for a goof EMS.

The outputs are:

- Direction & magnitude of the bidirectional converter current I_{bidir}, which is set in such a way that the FC current on the DC-bus node is proportional to the desired $P_{FC\ net}$ set by the EMS.
- On/off signals for all the power converters on board and the FCS.

The block diagram for power split control is schematized in Figure 4-20.

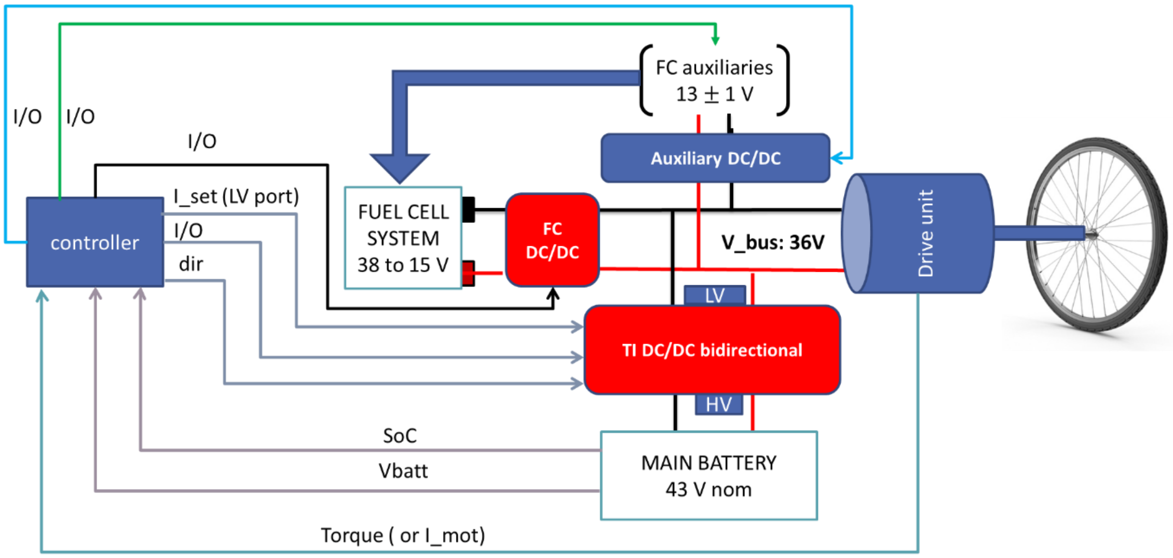

FIGURE 4-20. POWER SPLIT CONTROL SCHEMATIC

The following three converter were chosen for the purpose:

- The LM5170 48V-12V bidirectional converter evaluation module by Texas Instruments mounted on the battery side
- The I7C series buck-boost converter evaluation module by TDK mounted on the FC side
- The I34A series buck converter evaluation module by TDK to supply the FC auxiliaries

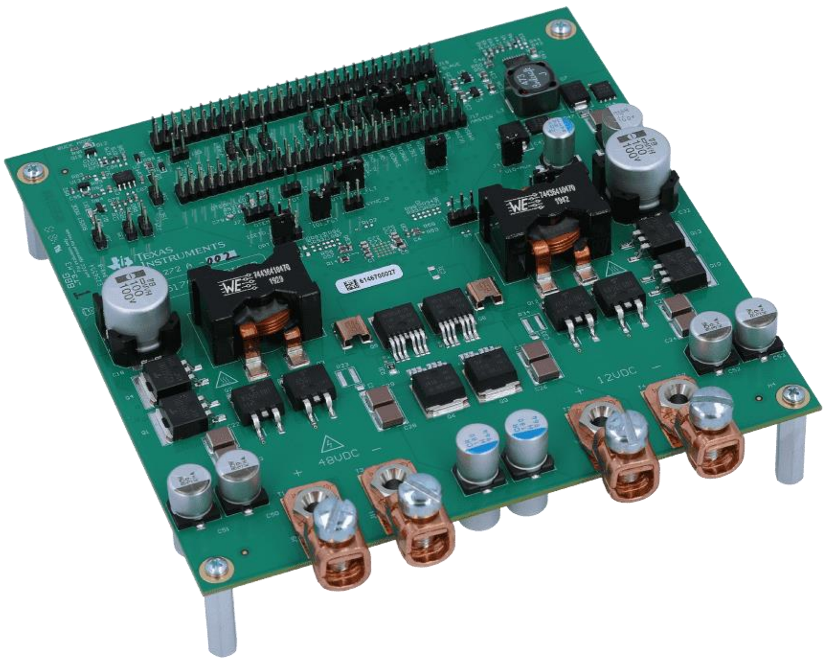

FIGURE 4-21. PICTURE OF THE LM5170-BIDIR CONVERTER EVALUATION MODULE

The LM5170-BIDIR Evaluation Module (EVM) is designed to showcase the LM5170-Q1 high performance dual-channel bidirectional controller suitable for, but not limited to, the automotive 48V to 12V dual battery system applications. The EVM can be configured to achieve a bidirectional power converter in the form of either current source or voltage source. The direction of power flow can be controlled either by an external command signal (DIR), together with the reference current and the turning on/off signal. Through the onboard interface headers, the EVM can be operated by an external MCU development kit board such as the TI C2000 Delfino LaunchPad XL [38], widely employed within the CARS group. The two channels operate in 180degree interleaved operation, and they evenly share a max dc current of up to 60A in/out the 12V port, which sets the converter's power rating to about 900W that is plenty for its application on the eCargo. It is equipped with built-in voltage loop control for both low voltage (LV) and high voltage (HV) ports, while it potentially accepts MCU digital voltage loop control through the interface connectors [39]. The most relevant features are summarized in Table 4-5.

TABLE 4-5. LM5170-BIDIR CONVERTER EVALUATION MODULE TECH SPEC

Port	Boost mode		Buck mode	
LV	3 ÷ 48 V	OVP disabled	14.5 V (if VL enabled)	OVP: 22 V
HV	50.5 V (if VL enabled)	OVP: 75 V	6 ÷ 75 V	OVP: 75 V

According to the voltage rating data in the table above, the mounting configuration was defined (see Figure 4-19). The LV port will be linked to the 36 V DC-bus while the HV port will be linked to the battery. For the converter to work there must always be a non-zero voltage difference between the bus and the battery terminals, a fact which influenced the choice of the battery.

Additionally, the EVM is factory set with over-voltage protection (OVP) circuitry on both power ports, a desirable feature which obstacles the application on the eCargo. As highlighted in **Errore. L'origine riferimento non è stata trovata.**, the OVP for the LV port in buck mode il 22 V, which is lower than the bus voltage and so not compatible with the future operating point of the device. Nonetheless, it is possible to change the OVP setting by replacing R18 in the EVM as explained in section 9.2.1.2.11 of the LM5170-Q1 datasheet [40].

As the factory inner loop voltage control is not matching the working voltages of the prototype, it was decided to keep it disabled for the first tests and to leave the duty of keeping the DC-bus voltage at 36V to the I7C series converter, which should be left on as well as the FCS during the early tests.

Concerning the EVM settings, the two and three pin headers should be kept with factory settings, while the following pins in J17 should be for sure connected to the LaunchPad board.

TABLE 4-6. LM5170-BIDIR RELEVANT PINS

Pin	Signal	Description
1	V48SN	HV port voltage sense, i.e., battery voltage sense
5	EN (MASTER ENABLE)	EVM enable signal
9	DIR	Power flow direction command
11 or 13	ISETA or ISETD	Channel current setting (analog voltage or PWM signal)
35	AGND	Reference GND for control signals

The LM5170-BIDIR was modeled within the FC hybrid eCargo model (Figure 4-1) through a Simscape *bidirectional DC-DC converter* block connected to the DC-bus and the battery model via electrical conserving ports. The block was initialized with parameters from the EVM's datasheet [39] that are reported in the table below.

TABLE 4-7. LM5170-BIDIR MODELING PARAMETERS

Switching device		Averaged switch
On-state resistance		0.001 Ohm
Protection diode	Forward voltage	0.8 V
	On resistance	0.001 Ohm
	Off conductance	1e-5 Ohm
LC parameters	Inductance	100 µH
	Inductor series resistance	0 Ohm
	C1	470 µF
	C2	100 µF
	R1	0.4 mOhm
	R2	0.4 mOhm

The block receives the gate physical signal, i.e., the Simscape equivalent to the PWM signal sent to a MOSfet's gate, which is set to "modulation waveform" so the model can act as an average-value converter. The signal's duty cycle is set by a PI controller which was tuned via Simulink's PID tuner tool [30] to obtain performances close to the ones described in the EVM's datasheet.

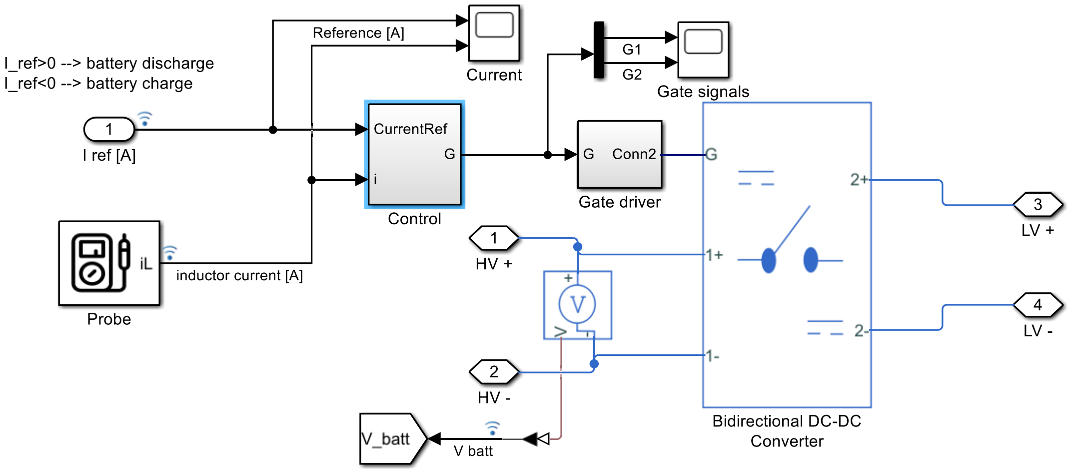

FIGURE 4-22. LM5170-BIDIR MODEL

Moving on, the converter model i7C4W008A120V-003-R belonging to the I7C series by TDK was selected for the FC side. It is a non-isolated step-up / step-down converter ideal for generating additional DC output voltage up to 300 W from a single output 12V, 24V or 48V DC power supply. The highly efficient i7C series accepts a very wide DC input and has a wide output adjustment range

[41]. For the eCargo application the corresponding evaluation module was selected because it incorporates the required external components to ensure the complete product functionality, such as fine output voltage trimming via trimmer pot VR1 [42].

FIGURE 4-23. I7C4W008A120V-003-R EVALUATION MODULE

The most relevant features are reported below

TABLE 4-8. I7C4W008A120V-003-R EVALUATION MODULE TECH SPEC

Type	Buck-boost
Input voltage range	9 ÷ 53 V
Output voltage range	9.6 ÷ 48 V
Output current (max)	8 A
Output power (max)	300 W
Efficiency	97%

As shown in Figure 4-20, the converter should be piloted by the LaunchPad board via an on/off signal, however this version can manually be turned on/off via the S1 switch present on the evaluation module [42], which is consistent with the need of keeping the FC on during early tests.

This part was modeled on Simscape through an *average value DC-DC converter* block which is connected to the bus and the FC via electrical conserving ports and reads as only input the converter efficiency. It is controlled via a duty cycle signal set by a PI controller tuned via Simulink's PID tuner [30] trying to match as much as possible the information on the converter's response from the datasheet.

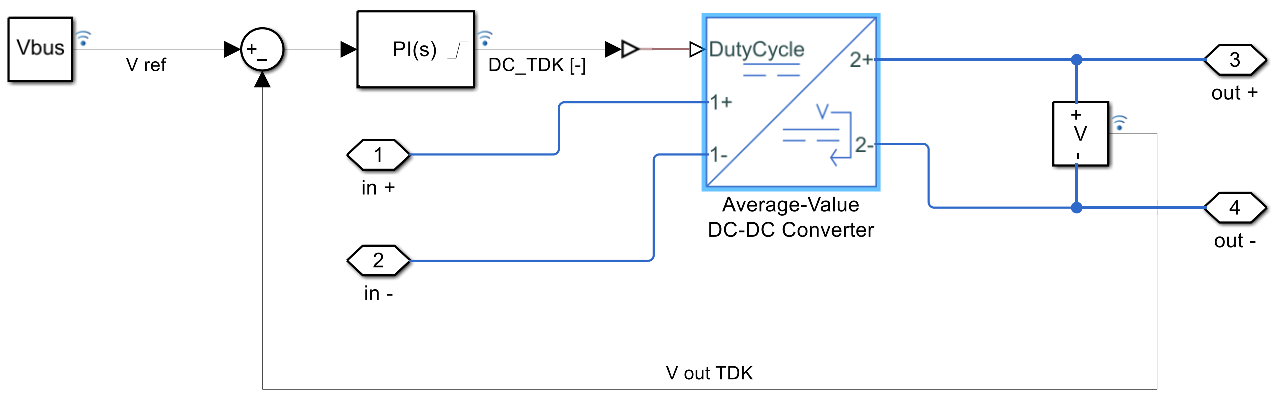

FIGURE 4-24. I7C4W008A120V-003-R MODEL

Finally, the FC controller will be supplied by another converter, the i3A4W008A033V-001-R belonging to the i3A series by TDK Lambda already installed on its evaluation module. It is a non-isolated DC-DC step-down converter that is are ideal for creating additional output voltage rails from a single output DC-DC power supply including battery sources. The highly efficient i3A series accepts a wide DC input and has a wide output adjustment range, which is made easy by trimmer VR1 welded on the evaluation module. Output trim, remote sense and negative logic remote on-off comes as standard features [43], [44].

FIGURE 4-25. I3A4W008A033V-001-R EVALUATION MODULE

The most relevant technical specifications are reported in the table below.

TABLE 4-9. I3A4W008A033V-001-R TECH SPEC

Type	buck
Input voltage range	9 ÷ 53 V
Output voltage range	3.3 ÷ 16.5 V
Output current (max)	8 A
Output power (max)	100 W
Efficiency	96.5%

As shown in Figure 4-20, the converter should be piloted by the LaunchPad board via an on/off signal, however this version can manually be turned on/off via the S1 switch present on the evaluation module [42], which is consistent with the need of keeping the FC on during early tests.

It was not really modeled on Simscape but his efficiency was considered by means of the gain in Figure 4-15.

This chapter ends with the proposed testing layout for the powertrain architecture described so far (Figure 4-26).

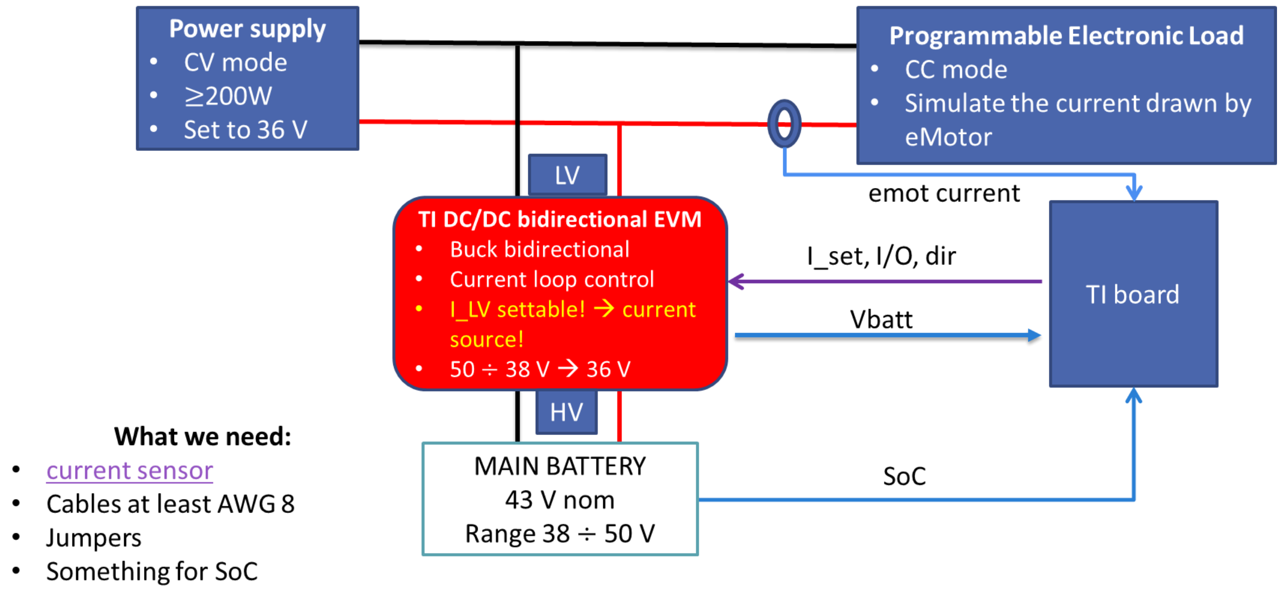

FIGURE 4-26. POWER-SPLIT TESTING LAYOUT

In particular, the aim of this testing layout it to gain a deeper understanding of the working principle of the TI bidirectional converter and make sure that it would work on the prototype. The layout relies on a bench power supply of at least 200W simulating the FCS (on the left in Figure 4-26) and on a programmable electronic load which simulates the eMotor power demand on the DC-bus. The latter should be programmed with the motor current demand over a reference cycle, which can be easily extracted from the Simscape simulation results, while the power supply should output a constant 36V voltage and have datalogging capabilities for recording the power output. If this is not possible, a current-voltage sensor should be added downstream to fill this purpose. The TI converter should be installed in the same conditions as in the future prototype and should be controlled in the same way. The only difference concerns the power demand at the bus which should be calculated from the current sensor in the picture, unless a way to program the LaunchPad synchronously to the electronic load with power demand data is found. In the pictures further details about testing can be found.

4.4 Hybridization battery

The range extender sizing approach (see section 2.3) implies that the FC provides the average power demand on a reference drive cycle, leaving the battery managing transient acceleration and deceleration phases. If this is assumed true, then the energy delivered by the FC on the DC-bus over the reference cycle is equal to the total energy demand of that cycle, meaning that the final battery SoC should be the same as at the beginning, $SoC\left(T_{cycle}\right) = SoC(0)$. In conclusion, the battery loses its role of energy storage and becomes mainly a power buffer. In this portion of the chapter the selection of a new battery pack for FC hybridization is described, with particular emphasis to the dimensioning process.

A power buffer should satisfy both the maximum power demand during transients and have enough energy stored for it; the same holds when fast charging occurs because of regenerative braking: the power buffer should have enough capacity to collect the maximum amount of transient energy over the reference cycles. Additionally, it should have maximum transient power rating safely above the maximum incoming or outgoing power peak.

Concerning the battery minimum energy content, it can be found starting from the integral functions of positive and negative energy at the wheel axle, i.e., $E_{wheel\,nrb}(t)$ and $E_{wheel\,rb}(t)$ respectively. By accounting for the efficiencies of the components upstream of the wheel axle, it is possible to obtain the total energy demand at the DC-bus for a bike with and without regenerative braking ($E_{bus\,rb}(t)$ and $E_{bus\,nrb}(t)$). These energy functions are then subtracted from $\bar{E}_{bus\,rb}(t)$ and $\bar{E}_{bus\,nrb}(t)$, the total bus energy if a constant power corresponding to the average power demand over the reference cycle ($P_{bus\,avg\,nrb/rb}$) were drawn. This maximum absolute value of the difference $\Delta E_{bus\,nrb/rb}$ is the minimum energy that the power buffer should store to complete the reference cycle with $SoC\left(T_{cycle}\right) = SoC(0)$. The passages are explained in the following equations.

Without regenerative braking:

$$E_{wheel\,nrb}(t) = \int_0^t P_{wheel\,nrb}$$

$$E_{\,bus\,nrb}(t) = \frac{E_{wheel\,nrb}\,(t)}{\eta_{trans} * \eta_{eMot} * \eta_{inv}} * PS$$

$$\bar{E}_{bus\,nrb}(t) = P_{bus\,avg\,nrb} * t$$

$$\Delta E_{bus\,nrb}(t) = \bar{E}_{bus\,nrb}(t) - E_{\,bus\,nrb}(t)$$

$$\mathrm{E_{batt\,min}} = \max\left(|\Delta E_{bus\,nrb}(t)|\right)$$

With regenerative braking:

$$E_{wheel\,reku}(t) = \int_0^t P_{wheel\,reku}$$

$$E_{bus\,rb}(t) = E_{\,bus\,nrb}(t) + E_{wheel\,reku}(t) * \eta_{trans} * \eta_{eMot} * \eta_{inv}$$

$$\bar{E}_{bus\,rb}(t) = P_{bus\,avg\,rb} * t$$

$$\Delta E_{bus\,rb}(t) = \bar{E}_{bus\,rb}(t) - E_{bus\,rb}(t)$$

$$\mathrm{E_{batt\,min}} = \max\left(|\Delta E_{bus\,rb}(t)|\right)$$

EQ 4-7

This calculation was performed for every combination of PS, urban driving cycle, and regenerative braking capabilities. Quantitatively, it was found that $E_{batt\,min} \geq 5.79$ Wh. The relative figure is reported below.

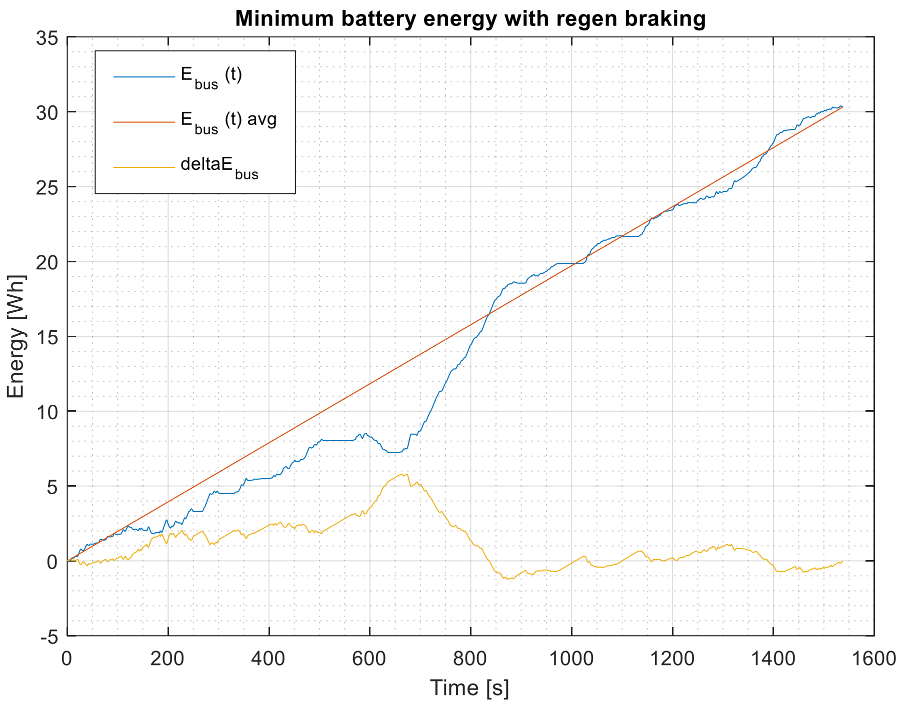

FIGURE 4-27. MINIMUM BATTERY ENERGY: CASE U1, PS=1, REGENERATIVE BRAKING

Regarding the battery power dimensioning, only the regenerative braking case was analyzed because it was deemed the most critical. The calculation procedure started from $P_{wheel\ nrb}$ and P_{reku} that were divided and multiplied by the chain of traction efficiencies and then added together to obtain $P_{bus\ rb}$. This was subtracted from $P_{bus\ rb\ avg}$ finding ΔP_{bus}, which minimum and maximum value were taken as the minimum acceptable discharge power rating ($P_{batt\ disch}$) and the minimum acceptable charge power rating ($P_{batt\ charge}$) respectively. The passages are summarized below.

$$P_{bus\ nrb} = \frac{P_{wheel\ nrb}}{\eta_{transm} * \eta_{eMot} * \eta_{inv}} * PS$$
$$P_{bus\ reku} = P_{wheel\ reku} * \eta_{transm} * \eta_{eMot} * \eta_{inv}$$
$$P_{bus\ rb} = P_{bus\ nrb} + P_{bus\ reku}$$
$$P_{batt\ disch} \geq \max\left(P_{bus\ rb}\right)$$
$$P_{batt\ charge} \geq -\min\left(P_{bus\ rb}\right)$$

EQ 4-8

All the combinations of PS and urban cycles with regenerative braking were analyzed and the results were $P_{batt\ disch} \geq 489\text{W}$ and $P_{batt\ charge} \geq 528W$. The figure reporting these results is shown below.

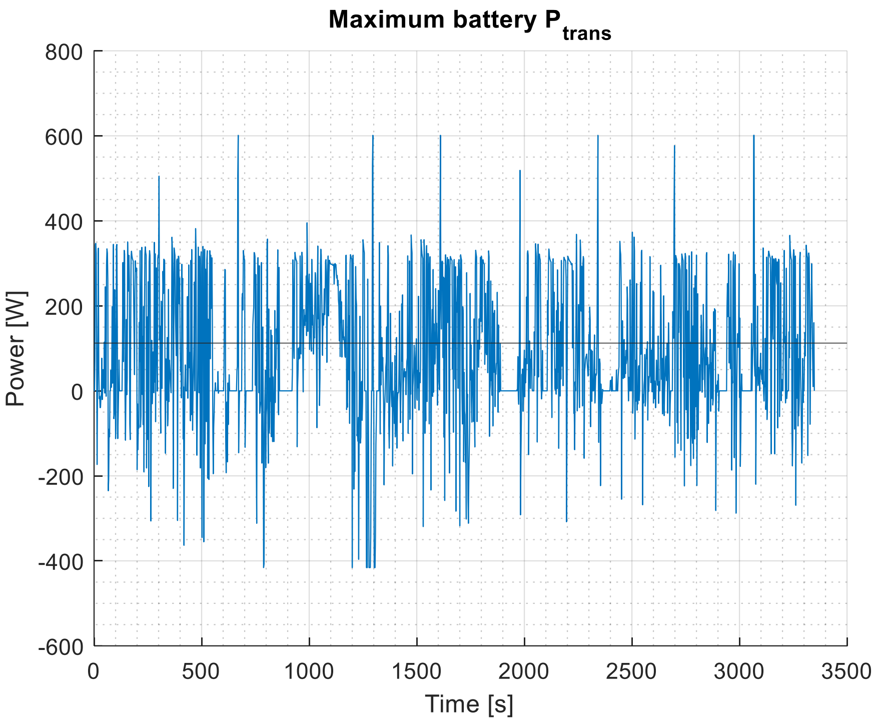

FIGURE 4-28. MAXIMUM BATTERY POWER: CASE U1, PS=1, REGENERATIVE BRAKING

According to the above information, the most critical technical requirement is the power rating rather than the battery capacity, being the latter very low compared to commercial eBike batteries' usual capacity.

Summing up, the required battery must have

- The above-mentioned peaking power rating in charge/discharge cycles
- The lowest capacity of the catalogue
- A minimum voltage that should be higher than 36V, in order not to hinder the functionality of the TI bidirectional converter (see section 4.3)

The best candidate was thus Bafang's battery pack BT F05.200.C [45], which salient technical specifications are reported below.

TABLE 4-10. BAFANG'S BATTERY TECH SPEC

Rated voltage	43 V
Nominal capacity	5 Ah
Energy content	200 Wh
Max continuous charge current	3 A
Max continuous discharge current	8 A
Voltage scope	32.4 - 49.2 V
Internal resistance	< 350 mOhm
Weight	<1.6 kg

The energy content is more than enough for the hybridization purposes, while the voltage range falls below the 36 V target, but it is considered acceptable as this happens at low SoC that should not be reached anyway. Power ratings can be estimated from the available data as follows:

$$P_{disch\ max}(cont) = 8\ A * 43\ V = 344W$$

$$P_{charge\ max}(cont) = 3\ A * 43\ V = 129W$$

EQ 4-9

Being these two continuous power rating, it is reasonable to assume that the peaking power ratings are higher and acceptable for the purposes of this work.

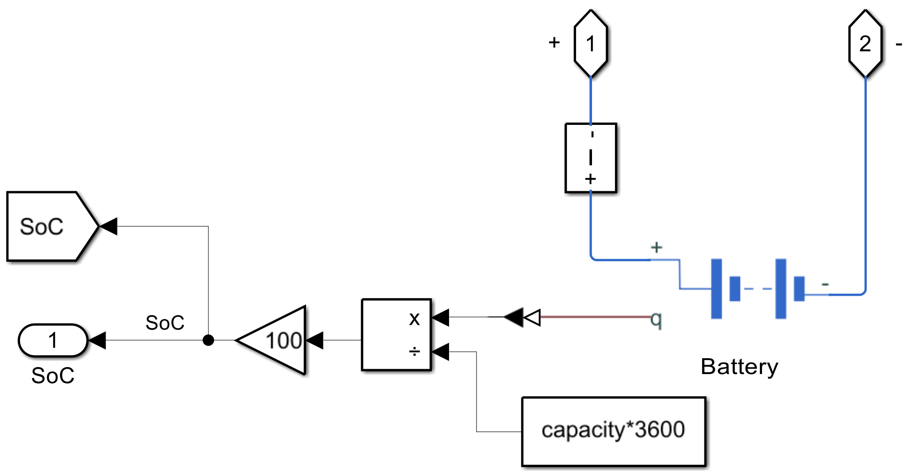

FIGURE 4-29. BATTERY MODEL

Once the hybridization battery was selected, the battery model was introduced on Simscape's simulation (). The backbone of the model is the *battery* block from Simscape electrical blockset parametrized with the selected battery parameters. A second version of the battery model was created for the battery-electric eCargo model by loading the original's BCargo battery parameters. The block reproduces the following battery equivalent circuit.

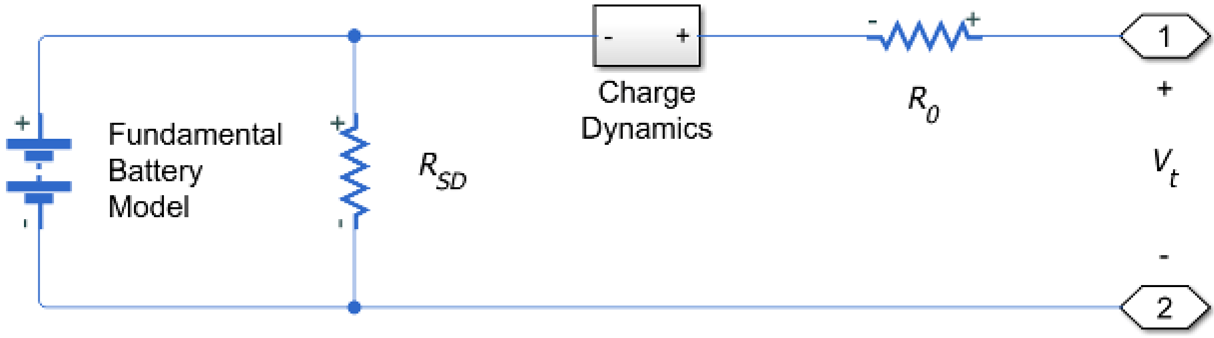

FIGURE 4-30. GENERIC BATTERY EQUIVALENT CIRCUIT [30]

The battery equivalent circuit is made up of the fundamental battery model, the self-discharge resistance R_{SD} (set to 0 for the purposes of this work), the charge dynamics model (neglected), and the series resistance R_0. The fundamental battery model reproduces a charge-dependent voltage source with output voltage as a function of charge according to the following relationship:

$$V = V_0\left(\frac{SoC}{1-\beta(1-SoC)}\right)$$

EQ 4-10

where:

- V_0 is the voltage when the battery is fully charged at no load, i.e., the maximum battery voltage.
- β is a constant that is calculated so that the battery voltage is *V1* when the charge is *AH1*, parameters that should be specified in the block. *AH1* is the charge when the no-load (open-circuit) voltage is *V1*, and *V1* is less than the nominal voltage.

The equation defines an approximate relationship between voltage and remaining charge. This approximation replicates the increasing rate of voltage drop at low charge values, and ensures that the battery voltage becomes zero when the charge level is zero [30]. As shown in Figure 4-29, the block outputs the internal charge level from which it is possible to estimate SoC.

For both batteries data from their discharge curve was necessary for such block, which were estimated by making reasonable guesses on the type of single cells that make up the two battery packs, for which the discharge curve was available. Bafang's battery was assumed to be composed of at least one pack of 12 Li-ion cells in series, in order to reach 43 V nominal from an average 3.6 V/cell [46]. Their capacity was found out iteratively by matching the battery pack total capacity with commercial single-cell one: the outcome was 2.5 Ah per cell arranged in 2 parallel stacks of 12 cells each (12s2p configuration). The single cell taken as a reference was the Samsung INR18650-25R and its discharge curve is reported below.

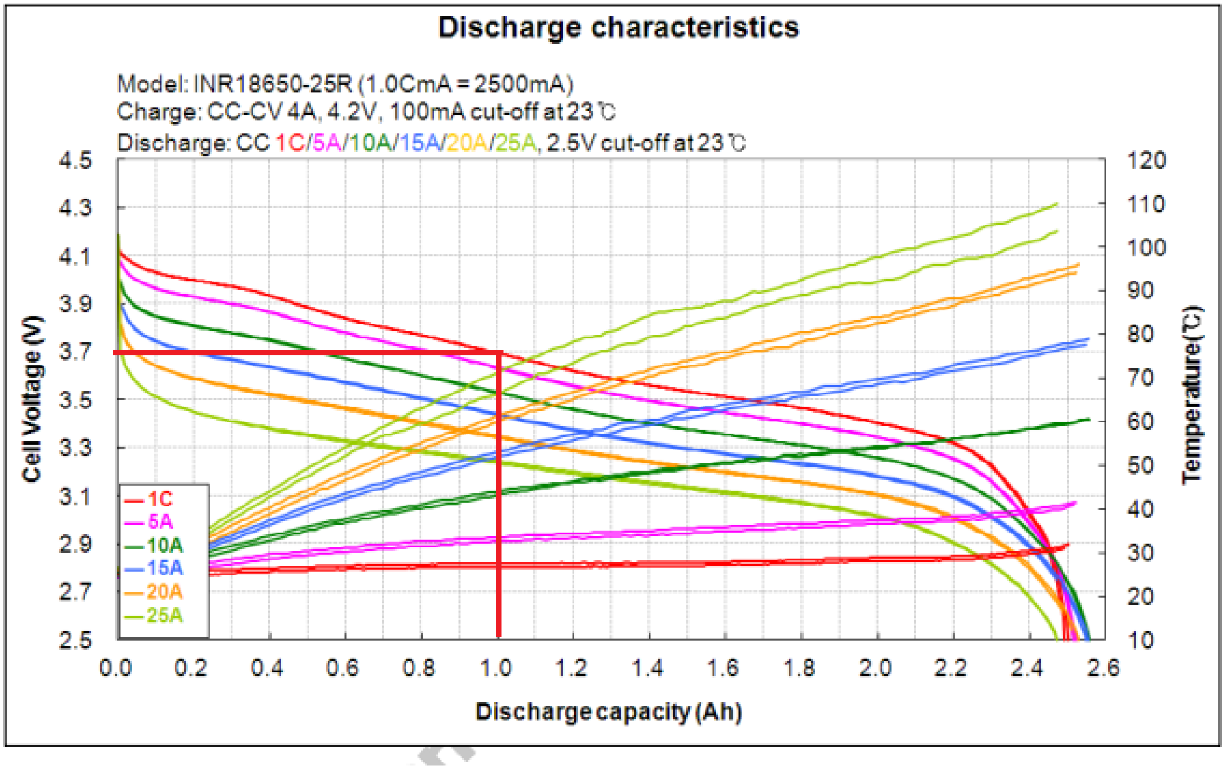

FIGURE 4-31. DISCHARGE CURVES FOR CELL **INR18650-25R** [47]

The values of AH1 and V1 were taken from the figure above considering the 1C discharge curve in red. The table below reports the summary of all the parameters fed to the *battery* block estimated from the single cell INR18650-25R or taken from Bafang's datasheet.

TABLE 4-11. BAFANG'S BATTERY MODEL BLOCK PARAMETERS

Maximum battery voltage	49.2 V
Internal resistance	0.350 Ohm
Battery capacity	5 Ah
V1	44 V
AH1	3 Ah

Regarding the original BCargo's battery model, in a similar fashion to the procedure above, the following hypotheses were made:

- The original battery pack is a BOSCH PowerPack 500, being the major commercial 500 Wh eBike battery available [29].
- Such battery pack is a 10s4p [46] made of LG 18650 MJ1 cells.

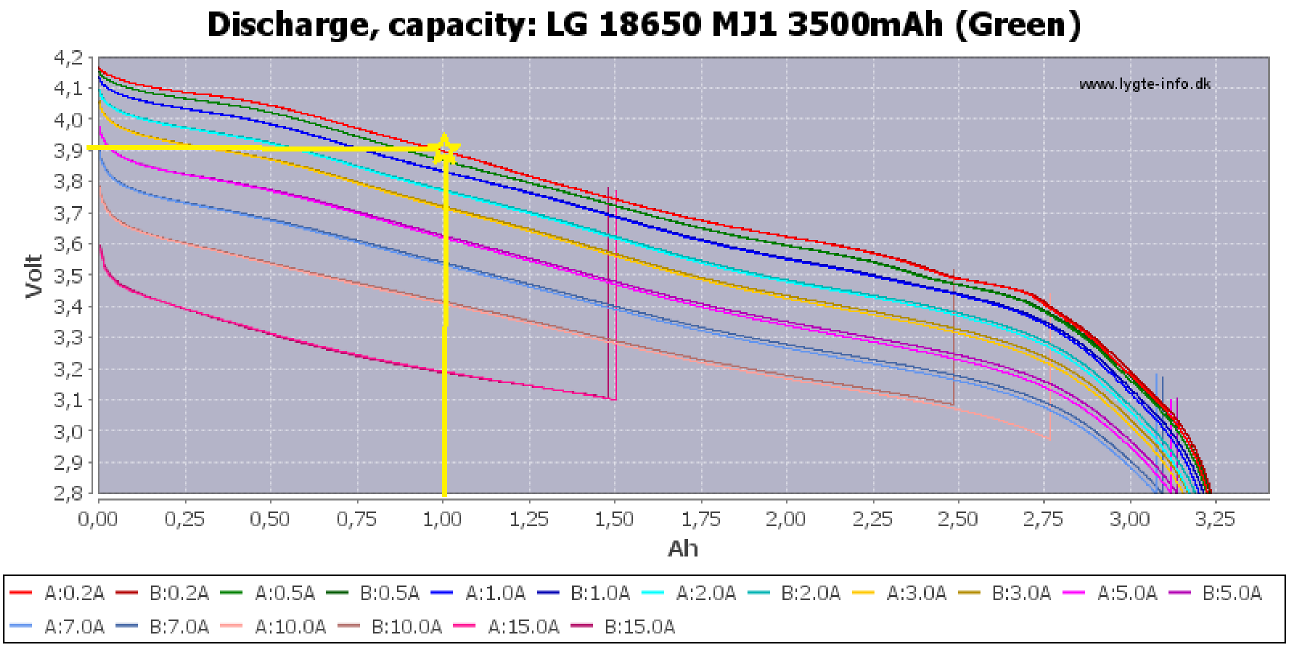

FIGURE 4-32. DISCHARGE CURVES FOR CELL LG 18650 MJ1 [48]

From Figure 4-32 and the specification found in BOSCH's battery datasheet [29], the following parameters were fed to Simscape's *battery* block.

TABLE 4-12. BOSCH'S BATTERY MODEL BLOCK PARAMETERS

Maximum battery voltage	42 V
Internal resistance	0.140 Ohm
Battery capacity	13.4 Ah
V1	31 V
AH1	10 Ah

4.5 Power split control: fuzzy logic

The idea of introducing this type of controller controller originated from Lin's thesis, where a fuzzy logic controller manages the power split between a fuel cell and a battery on a road vehicle [23]. As the prototype required as well some kind of energy management system to work, for design completeness it was decided to introduce it. Nonetheless, the vehicle's powertrain in Lin's work was sized following a load follower approach (see section 2.3), so the developed controller cannot be suitable for a fuel cell hybrid eCargo sized as range extender. Because of this reason, the main reference for the development of such controller was the work from Yang et al. on a fuzzy logic EMS development for a hybrid electric vehicle endowed with a FC range extender [49].

The idea of control algorithm was mostly inspired but Yang et al. and it can be summarized as follows.

1. If the battery SOC is medium, the FCS should turn on and vary its power output in such a way to keep the SOC close to starting value.
2. If the battery SOC is high, then only the battery works to supply the energy of the system until the power demand $P_{bus\ dem}$ increases to medium and high values, in which case the FC turns on at a high efficiency operating point.
3. If the SOC progressively decreases to low, the fuel cell should work at high power operating points, thus moving away from the high efficiency region but preventing deep discharge of the battery
4. If $P_{dem\ bus}$ transitions to negative, i.e., the bike is recovering energy during braking, the FC should move to higher efficiency operating points with respect to when $P_{dem\ bus} > 0$, eventually turning off in case the battery SOC is too high

These rules were translated into membership functions and rules that will be illustrated below. Notice that all the functions have a normalized unitary scale.

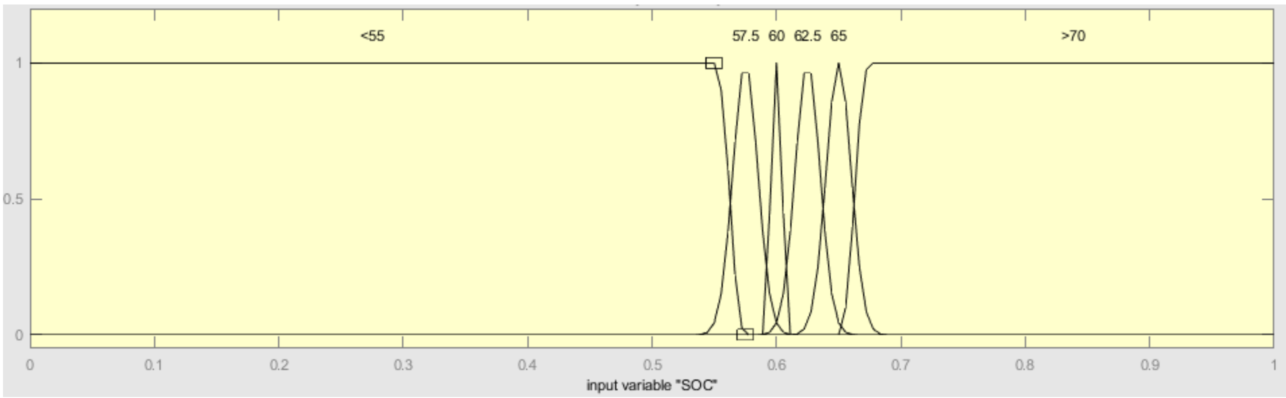

FIGURE 4-33. SOC MEMBERSHIP FUNCTIONS

The SoC admissible range was subdivided into six intervals, all named with a SoC value that is most representative for each interval. Each interval was assigned a membership function of types Z-shaped, Gaussian and Triangular for the "60" case, which corresponds to the "target" SoC at which the battery should be kept to. The crowding of functions near this case is needed to tailor more carefully the output FC power ($P_{fc\ out}$) in each case to better reach the SoC target.

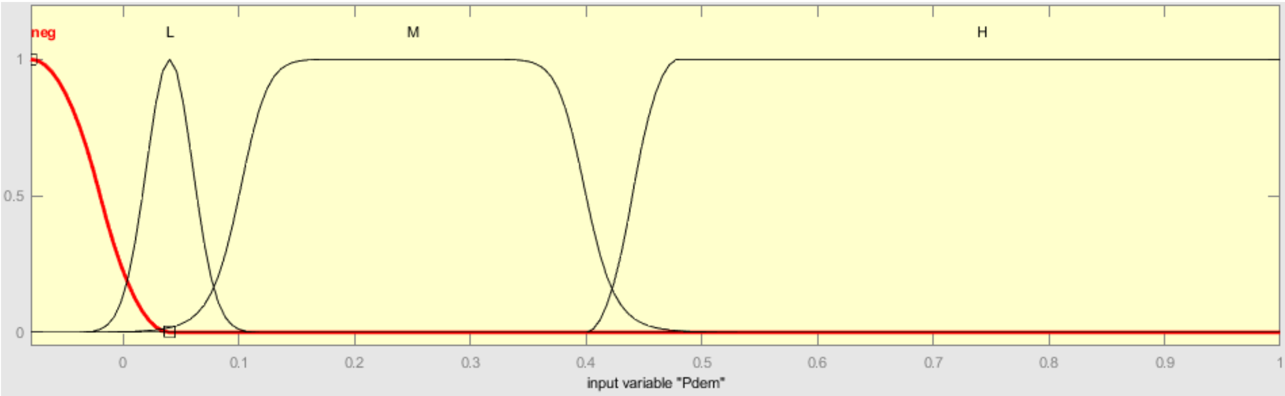

FIGURE 4-34. BUS POWER DEMAND MEMBERSHIP FUNCTIONS

Regarding $P_{bus\ dem}$, the working region is divided into 4 intervals in order to identify when the FC should work at rated power, at high power or at highest efficiency.

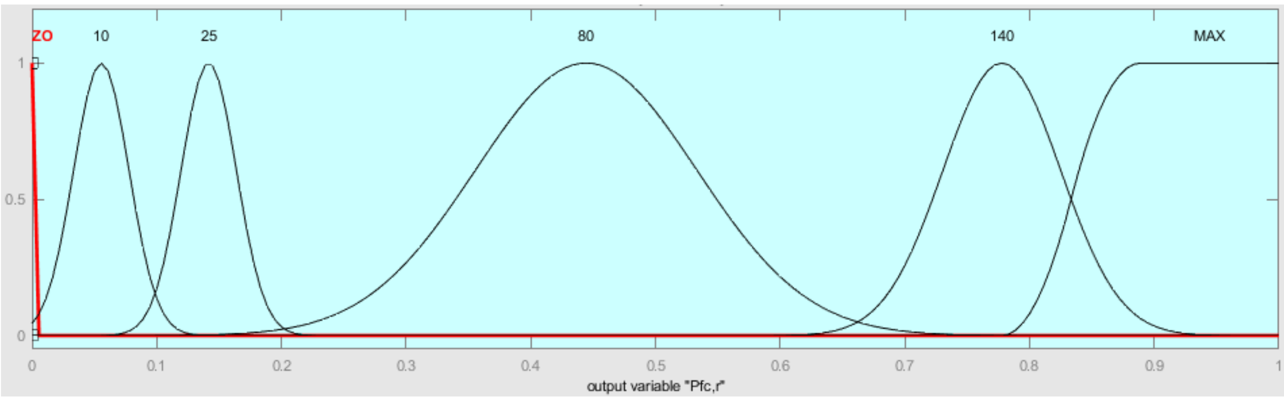

FIGURE 4-35. FC POWER OUTPUT MEMBERSHIP FUNCTIONS

Finally, the $P_{fc\ out}$ working region was divided in six intervals named after the most representative value for each of them, as for the SoC. The intervals were chosen and matched to the SoC membership function in such a way that when $SoC = 0.575 \rightarrow P_{fc\ out} = 140\ W$, which is the maximum power demand at the bus for the analyzed combinations of urban cycle, PS and regenerative braking. When $SoC = 0.625 \rightarrow P_{fc\ out} = 25W$, which corresponds to the minimum power requested in all of the above-mentioned combinations. When $SoC = 0.6 \rightarrow P_{fc\ out} = 80W$, which is something in between the other two power outputs. The remaining intervals correspond to the maximum FC power output (MAX) which is hit when SoC is low or P_{dem} is very high, 25 and 10 are the high efficiency region of the FC while ZO is the off state.

These functions were combined by a set of rules that is reported in the table below.

TABLE 4-13. FUZZY RULES

P fc out		SoC					
		<55	57.5	60	62.5	65	>70
P dem	Neg	80	25	10	ZO	ZO	ZO
	L	140	80	25	10	ZO	ZO
	M	MAX	140	80	25	10	ZO
	H	MAX	MAX	140	80	25	10

The resulting fuzzy logic controller was transformed into a surface for better visualization and for import in the Simscape model via a 2D lookup table, which resulted in a much lower computational cost than simulating with the controller itself.

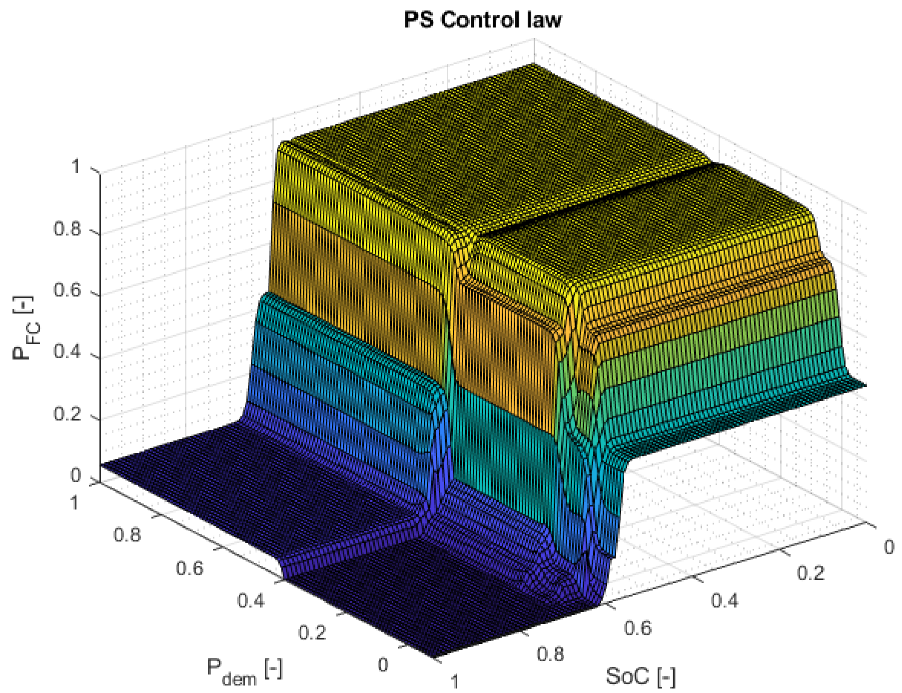

FIGURE 4-36. FUZZY LOGIC CONTROL SURFACE

The Simscape model of the EMS can be found in the TI C2000 subsystem, which is organized so it is possible to simulate with the EMS or with a pre-set constant FC output power by setting $I_{fc\,net}$, the fuel cell current output on the DC-bus. Said current is then subtracted from I_{mot}, the eMot current, to obtain I_{set}, the current to/from the battery which is set by the TI bidirectional converter controller (see Figure 4-22).

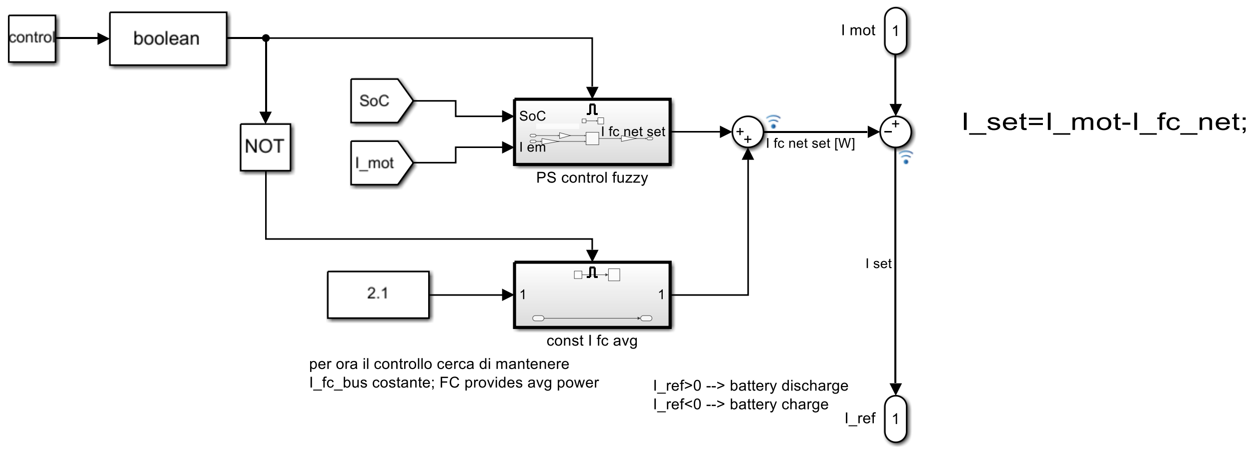

FIGURE 4-37. POWER SPLIT CONTROL MODEL

As already mentioned above, the fuzzy logic power split control is achieved on Simulink through a *2-D lookup table* block, which maps inputs to an output value by looking up or interpolating a table of values set by the user with block parameters [30]; in this case the control surface in Figure 4-36. The inputs are normalized SoC and P_{dem} data while the output is the normalized $P_{fc\,out}$. The former is obtained from a sensor on the bus measuring I_{mot} which is then multiplied by the reference bus voltage V_{bus}, on the other hand $P_{fc\,out}$ must be de-normalized and divided by V_{bus} to obtain $I_{fc\,net}$.

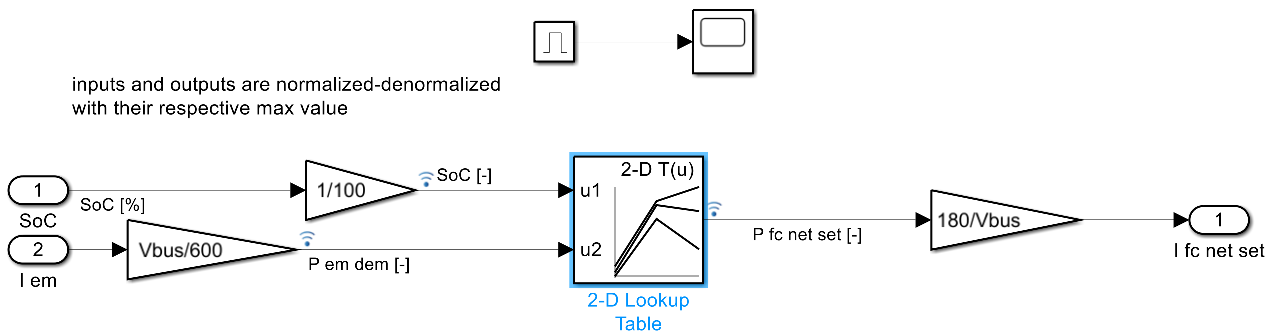

FIGURE 4-38. FUZZY LOGIC CONTROL MODEL

5 Results & discussion

This chapter's aim is to describe the results from Simulink's dynamic model. In the first part a series of graphs are shown that should give a better insight on how key topics such as power split and speed tracking are achieved in the model, followed by tables collecting the numerical results un terms of energy consumption, driveline efficiency and range extension. Finally, the results from Simulink are compared with the backward-modeling ones in order to check for consistency.

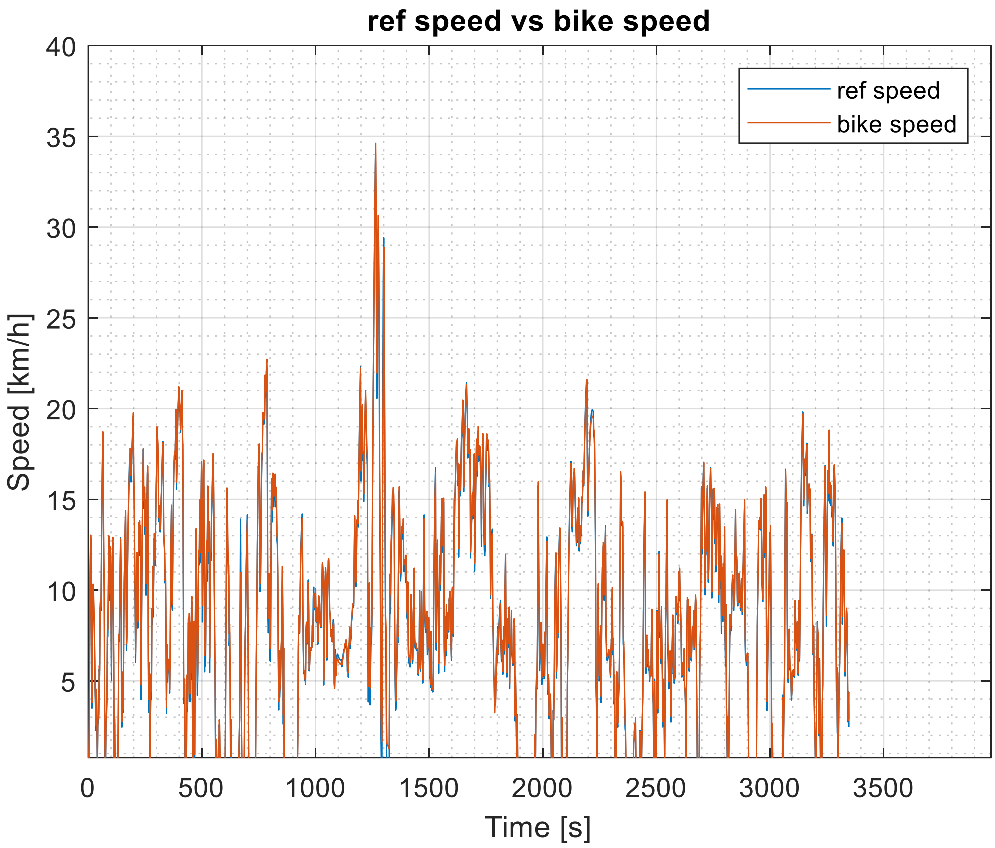

FIGURE 5-1. SPEED PLOT FROM SIMULATION OUTPUT

The *longitudinal driver* block tracks the reference speed with a maximum delay of 0.8 s due to the driver response and vehicle dynamics. The maximum difference between the reference speed and the bike speed that was recorded is around 0.7 km/h. These performances were considered acceptable by the author, but indeed are responsible for at least some of the differences in results between the quasi-static simulation and the Simulink one.

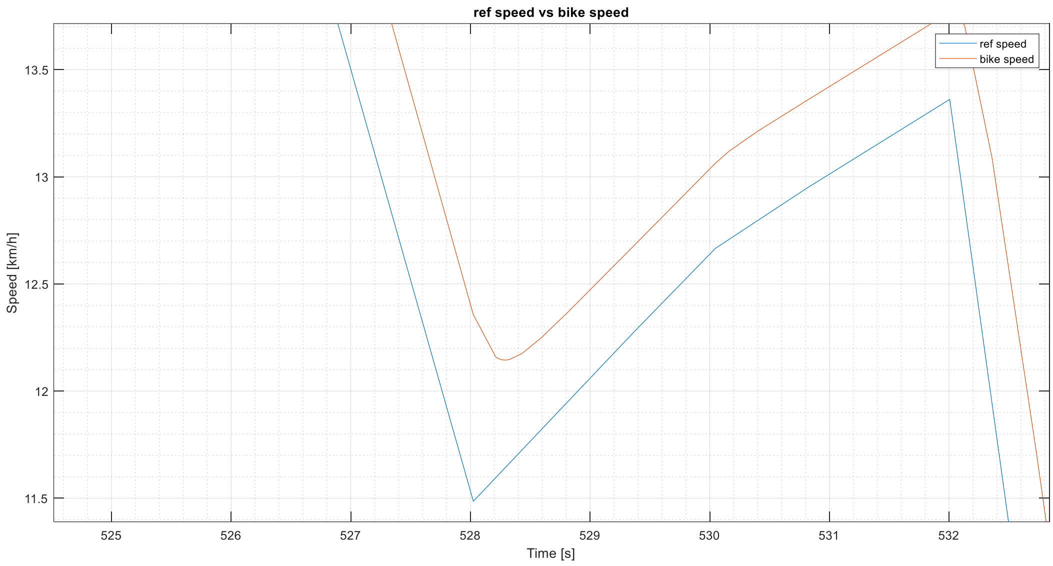

FIGURE 5-2. ZOOM OF THE VELOCITY TRACKING PERFORMANCES

The following figure show how the mechanical power is split between the eDrive model and the rider model when PS =0.5, so the conditions in which the rider provides the highest amount of power for motion.

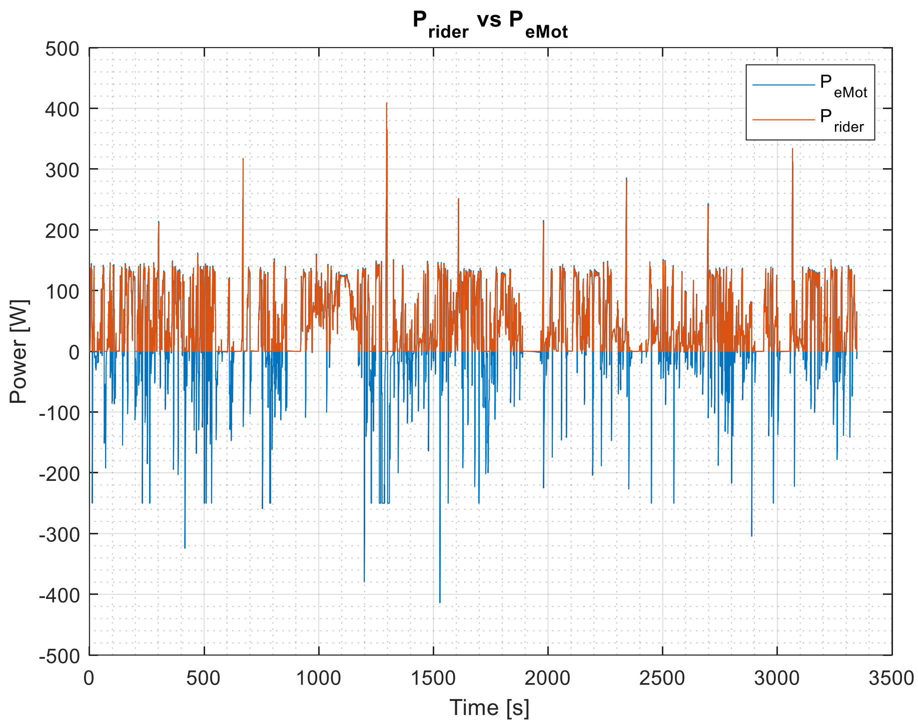

FIGURE 5-3. POWER SPLIT RIDER-EMOTOR WITH PS=0.5 AND CYCLE U1

The blue plot is the power provided by the eMotor and it can be noticed that becomes negative when regenerative braking occurs while the other stays zero. It is worth to point out that the rider in this case outputs an average continuous power of about 100W, whilst the peaking power reaches more than 400W, which probably is too much for an average delivery rider.

On the other hand, the FCS-battery current-split is successfully achieved as shown in the next figure.

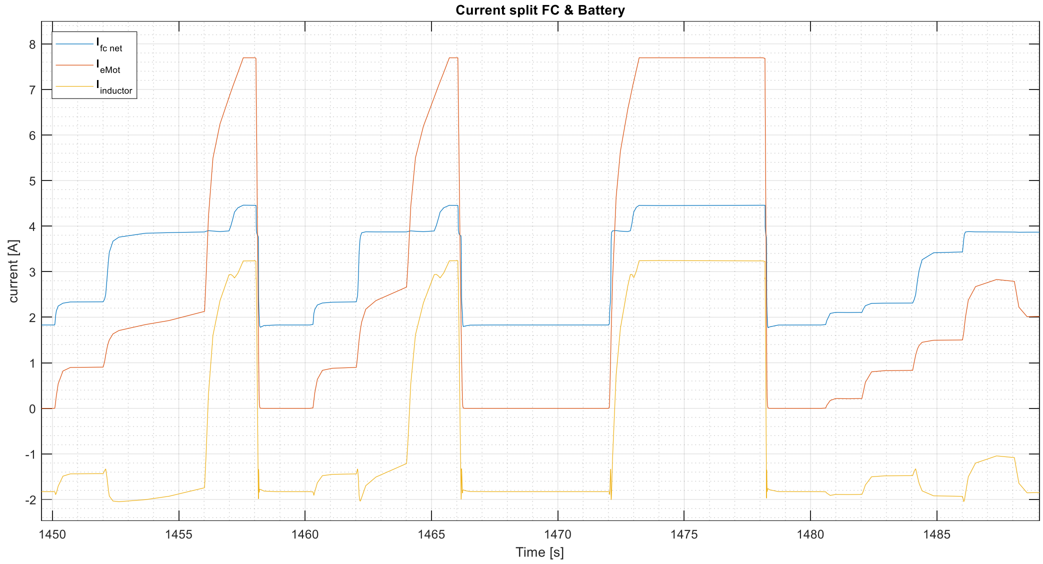

FIGURE 5-4. ZOOM OF DC BUS NODE CURRENTS FOR U1, PS=1, NRB

By analyzing the currents at the DC-bus node between the FCS branch and the battery branch in the figure above, it is evident that the three currents are always related by Kirchoff's current law as expected:

$$I_{FC\ net} + I_{inductor} - I_{eMot} = 0$$

$$I_{FC\ net} = I_{eMot} - I_{inductor}$$

Where $I_{inductor}$ is the inductor current in the TI bidirectional DC-DC, which is the result of the converter's PI controller tracking I_{ref}, i.e., the desired inductor current according to the fuzzy logic controller(see section 1.1). The power split controller performances can be assessed by checking the power split, SoC, the stack efficiency, and the FCS efficiency in the least and most demanding combinations of driving cycle, PS and regenerative braking capability.

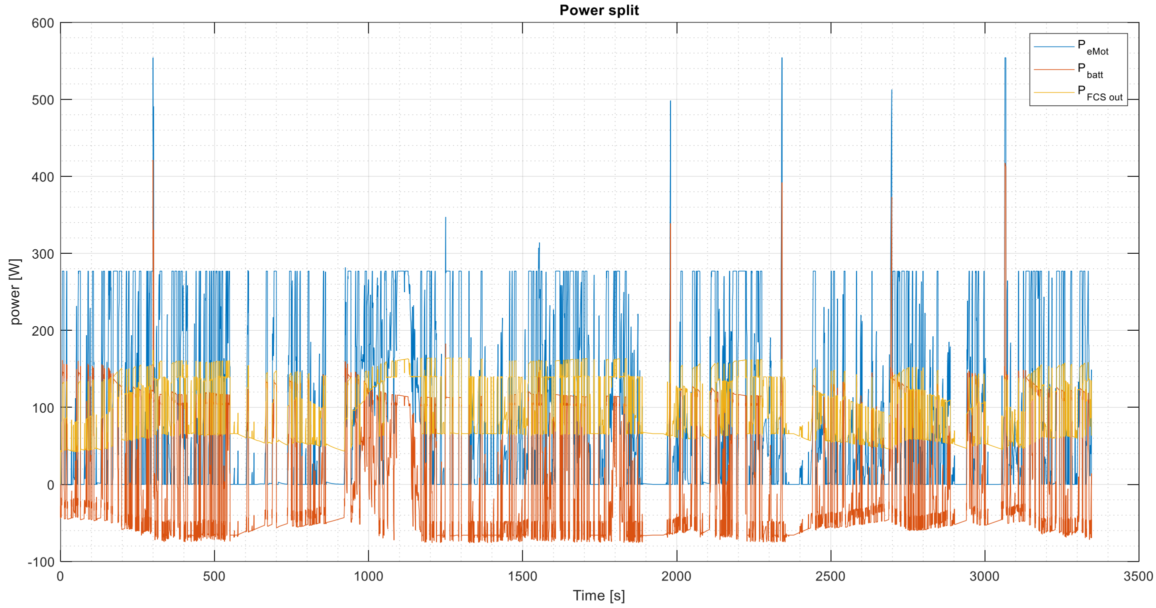

FIGURE 5-5. FCS-BATT POWER SPLIT FOR U1, PS=1, NRB

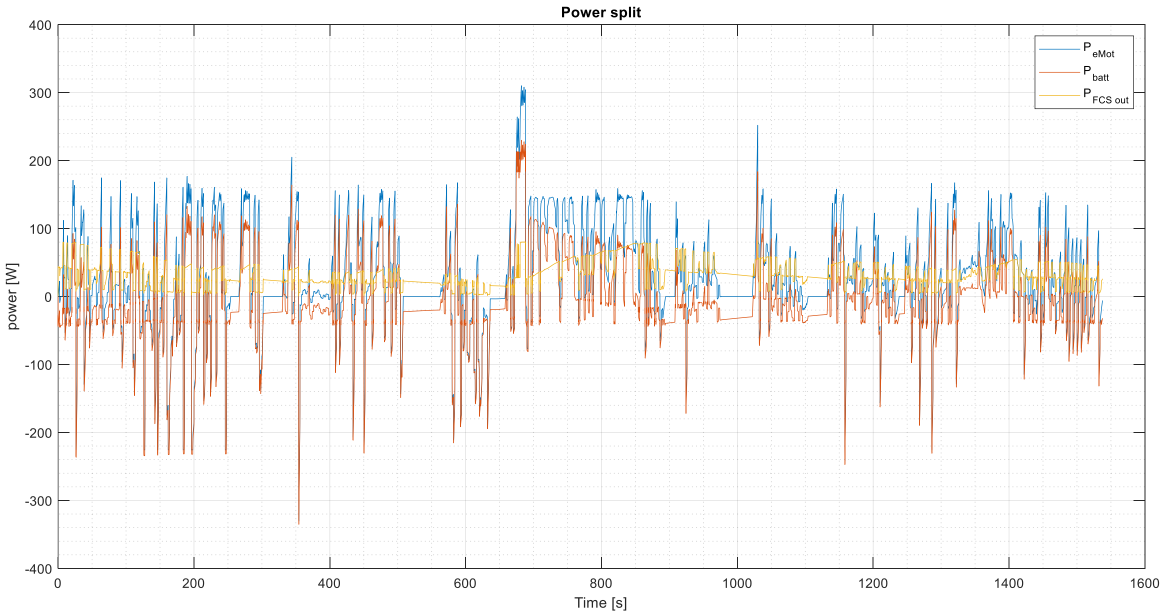

FIGURE 5-6. FCS-BATT POWER SPLIT FOR U2, PS=0.5, RB

IT CAN BE NOTICED IN BOTH FIGURES ABOVE THAT THE CONTROL STRATEGY TENDS TO VARY CONSIDERABLY THE FCS POWER WITHIN A CERTAIN INTERVAL, FROM ABOUT 50W TO 150W IN

FIGURE 5-5 AND FROM ALMOST 0W TO ABOUT 100W IN

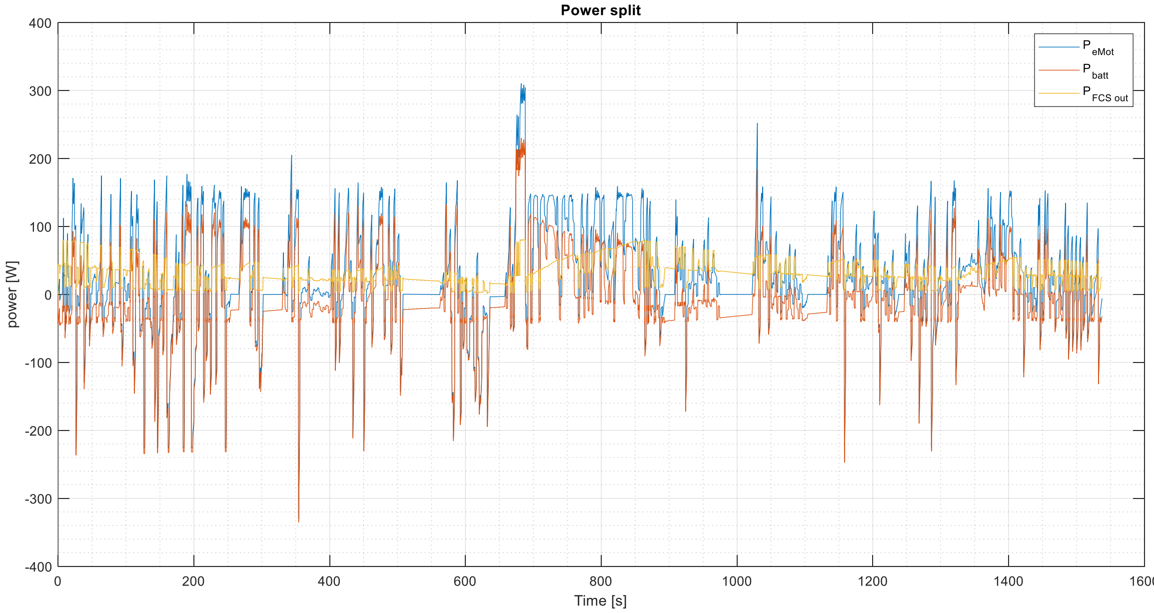

Figure 5-6. These sharp load changes could eventually deteriorate the FC, which tends to last longer and work more efficiently in stationary conditions. Nonetheless, in Figure 5-5 this control strategy helps keeping the battery power well below the boundaries set in Eq 4-9, in other words $-129W < P_{batt} < 344W$, which are the continuous power ratings for the selected hybridization battery. This holds for most of the analyzed drive cycle, with a few exceptions on the peaks. On the other hand, in the scenario pictured in Figure 5-6, rapid battery charge occurring during regenerative braking generates high power peaks, mostly above the maximum continuous charge power. Hence, it will be necessary to check with Bafang about the maximum transient charge power for the selected battery, in order to make sure that dangerous effects will not be set up by an excessive charging current.

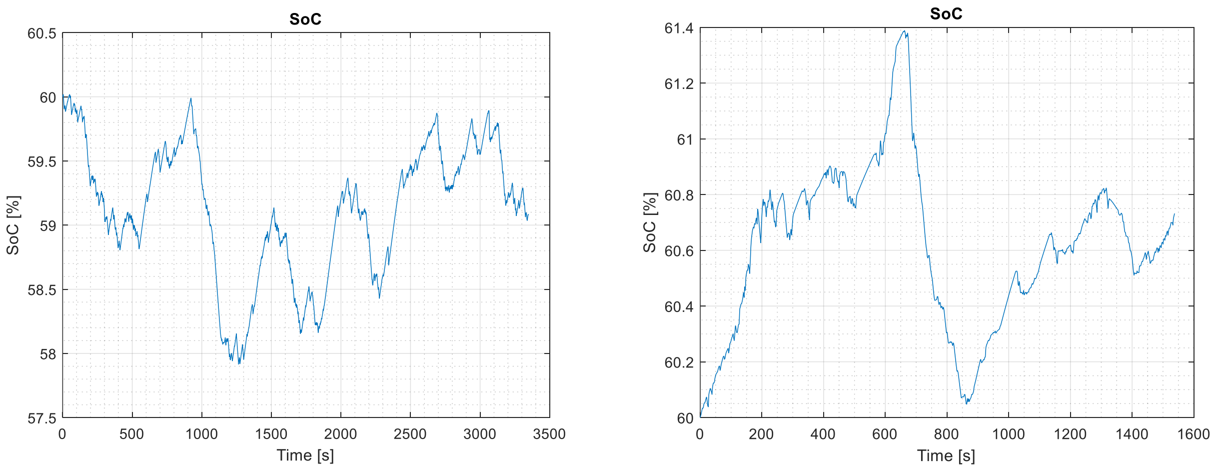

FIGURE 5-7. SOC TREND IN BOTH U1,2; PS=1,0.5; NRB, RB CASES RESPECTIVELY

Concerning the SoC management, Figure 5-7 show that the fuzzy logic controller is very successful in implementing battery charge sustaining, as the difference in SoC between the beginning and the end of the two cases is less than $\pm 1\%$. This is true for all the combinations of driving cycle, PS, and regenerative braking capability, since the two plots above are referred to the worst and the best scenarios respectively and all the other scenarios present a final SoC included between the two above.

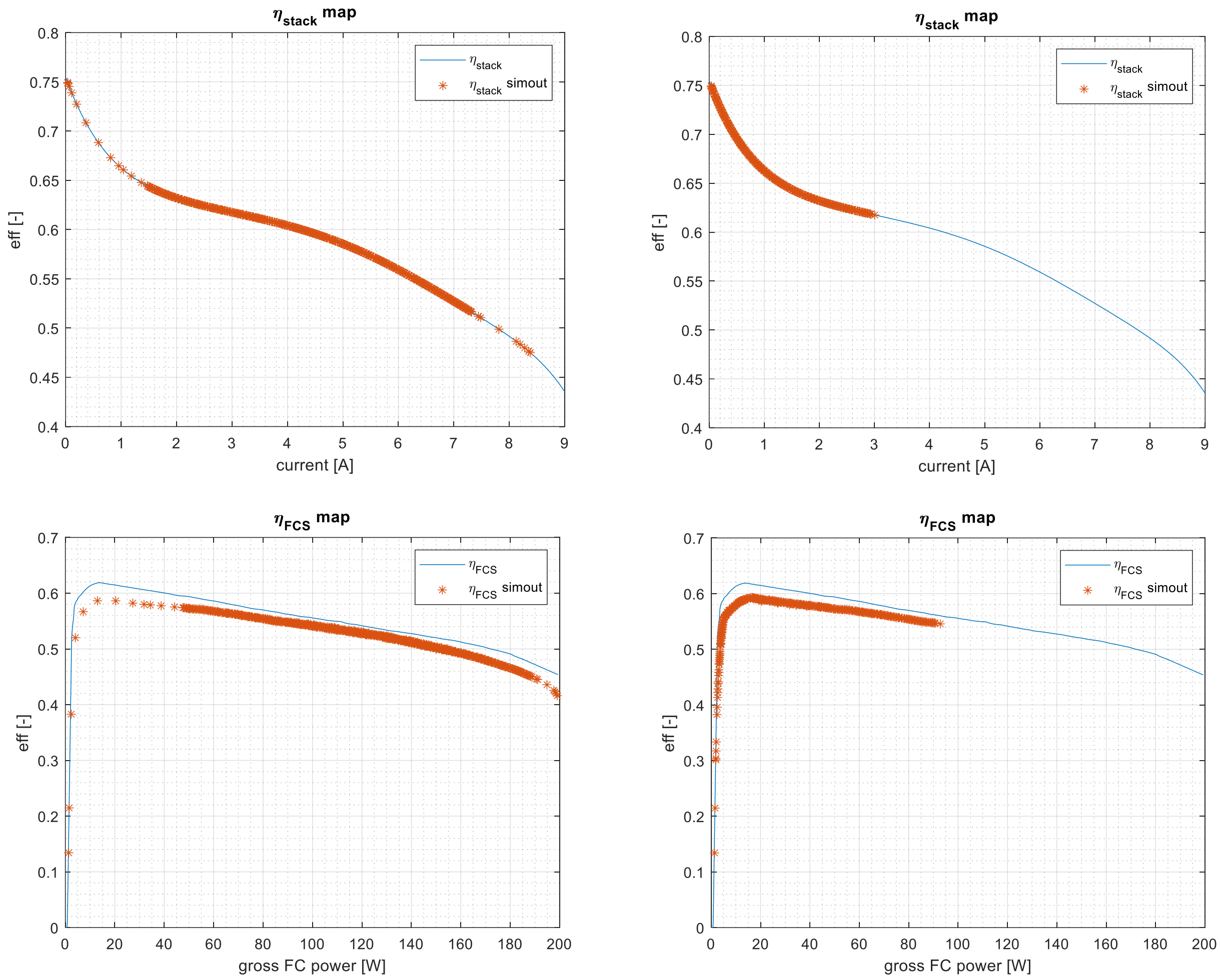

FIGURE 5-8. η_{stack} *and* η_{FCS} IN SCENARIO U1, PS=1, NRB ON THE LEFT AND SCENARIO U2, PS=0.5, RB ON THE RIGHT

Concerning the FCS and stack efficiency, Figure 5-8 shows the stack and overall FCS efficiency (in blue) for the two scenarios, while the red marks indicate the operating point of the fuel cell during the driving cycle. It is worth to point out that the FCS efficiencies during the cycles are lower than the theoretical value due to the presence of the power converters, which losses ad up to the auxiliary FCS power. Both efficiency values assumed throughout the cycle are fairly spread out, for example in the most demanding scenario (plots to the left) it is evident that η_{FCS} spreads between 0.44 and 0.58 while η_{stack} oscillates between 0.65 and 0.5. This is consistent with Figure 5-5 in which the net FCS power often varies throughout an interval going from 50W to 150 W, which correspond to slightly higher values of FC gross power that can be observed in Figure 5-8 left. On the other hand, η_{FCS} and η_{stack} in the least demanding scenario to the right vary between 0.40-0.58 and 0.62-0.75 respectively. The gross FC power output is again consistent with the net FCS power output shown in Figure 5-6.

These plots prove that the power split controller could be improved in its capabilities to keep the FCS efficient. In the bottom right plot, it is evident that a good portion of the FCS efficiencies hit during the cycle falls to the left of the high efficiency region, where η_{FCS} falls sharply within just a few watts of power.

This matter was investigated further with the help of the following equations.

$$E_{H_2\,fuzzy}(t) = \int_0^t \dot{H}(I_{FC\,gross}) * h_{H_2}$$

$$E_{H_2\,ideal}(t) = \frac{\bar{P}_{FCS\,net}}{\bar{\eta}_{FCS}} * t \qquad \textbf{EQ 5-1}$$

Where $\dot{H}(I_{FC\,gross})$ is the hydrogen flow rate (see Eq 2-6), which is a function of the stack's output current, and h_{H_2} is the hydrogen's specific enthalpy equal to 33.5862e3 Wh/kg [13]. $\bar{P}_{FCS\,net}$ and $\bar{\eta}_{FCS}$ are the average FCS power output on the DC-bus and the average operating FCS efficiency over the cycle. $E_{H_2\,fuzzy}(t)$ is the resulting hydrogen energy consumption over a reference drive cycle, while $E_{H_2\,ideal}(t)$ can be seen as the same energy consumption if the power split controller were ideal. An ideal power split controller keeps the FC at constant power equal to the average power demand over the cycle, which is easy to implement if the cycle is known but not applicable in case of road vehicles. A graphic example for the most relevant case is reported below.

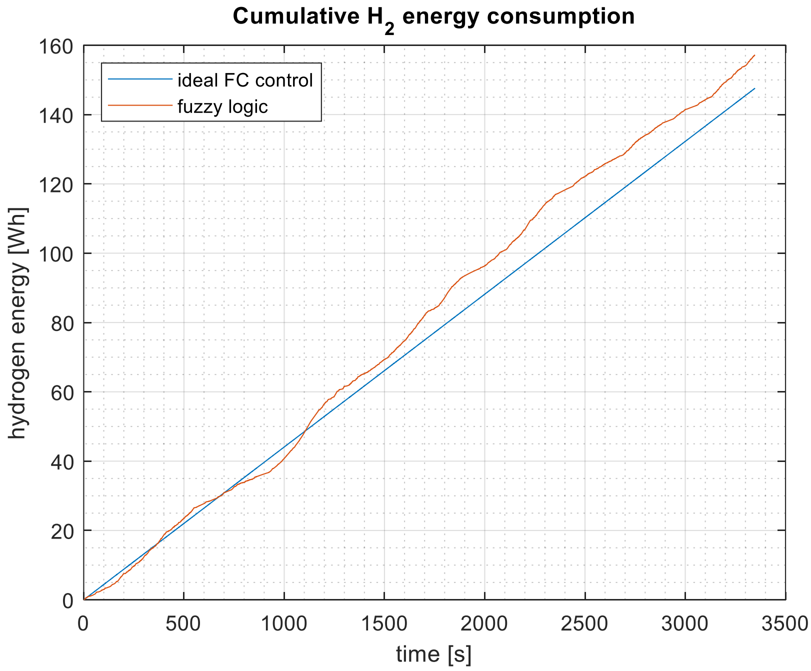

FIGURE 5-9. HYDROGEN ENERGY CONSUMPTION IN THE SCENARIO U1, PS=1, RB

The red line represents $E_{H_2\,fuzzy}(t)$ while the blue one $E_{H_2\,ideal}(t)$. Due to the actions of the fuzzy logic controller, a positive difference can be noticed between the two energies. In fact, $E_{H_2\,fuzzy}(t)$ ends up higher than $E_{H_2\,ideal}(t)$ because the power split controller does not maintain the optimal FC efficiency, which would be achieved with an ideal controller. Thus, the performances of the power split controller can be measured by such difference, i.e., $\Delta E_{H_2} = E_{H_2\,fuzzy}(T_{cycle}) - E_{H_2\,ideal}(T_{cycle})$. This calculation was performed and transformed in percentage increments in Table 5-1.

TABLE 5-1. PERCENTAGE INCREMENT OF ΔE_{H_2}

PS	with FCS range extender		FCS range extender & regenerative braking	
	Simscape: $\Delta E_{H_2}(T_{cycle})$			
	U1	U2	U1	U2
0.5	+2.2%	+2.1%	+2.3%	+1.8%
0.66	+2.7%	+2.5%	+3.3%	+2.7%
0.75	+3.1%	+3.0%	+3.9%	+3.4%
0.8	+3.4%	+3.3%	+4.2%	+3.8%
1	+4.8%	+4.6%	+6.1%	+5.7%

It is worth to notice that for little eMotor assistance the controller performs well, while its decision-making worsens up to more than 6% as the eMotor assistance increases. From these results it can be deducted that the fuzzy-logic EMS performs generally worse as the power demand from the eMotor increases, especially if regenerative braking is active. This might be due to the "power-follower" strategy that the controller applies during power demand peaks (section 1.1).

TABLE 5-2. AVERAGE FCS EFFICIENCY MEASURED IN THE FORWARD MODEL

PS	with FCS range extender		FCS range extender + 100% regenerative braking	
	Avg fcs efficiency in Simscape			
	U1	**U2**	**U1**	**U2**
0.5	0.57	0.57	0.58	0.58
0.66	0.56	0.56	0.57	0.57
0.75	0.55	0.56	0.56	0.57
0.8	0.55	0.55	0.56	0.56
1	0.53	0.54	0.54	0.55

It is also worth to point out that if the efficiencies in Table 5-2 are compared with the ones in the backward modeling chapter in **Errore. L'origine riferimento non è stata trovata.**, a difference of about 0.2 is observed, which is perfectly consistent with the difference between the theoretical η_{FCS} function and Simulink's measured efficiency in Figure 5-8. Thus, such difference is to be attributed mainly to the presence of the DC-DC converters, which were not included in the backward model, while the fuzzy logic controller affects mostly the instantaneous efficiency, resulting in higher energy consumption.

TABLE 5-3. DYNAMIC MODEL ENERGY CONSUMPTION RESULTS & INCREMENTS WITH RESPECT TO THE BENCHMARK (BORDERS IN RED)

Simscape: energy consumption [Wh/Km]																		
PS	**Battery only**		**with 100% regenerative braking**				**with FCS range extender**				**FCS range extender & regenerative braking**			
	U1	**U2**	**U1**		**U2**		**U1**		**U2**		**U1**		**U2**	
0.5	3.5	3.1	2.5	-29%	2.1	-34%	6.5	+88%	6.2	+98%	4.7	+37%	4.4	+40%
0.66	4.6	4.1	3.6	-22%	3.0	-26%	8.7	+90%	7.9	+94%	6.8	+49%	6.0	+48%
0.75	5.2	4.7	4.2	-19%	3.6	-22%	10.0	+93%	9.1	+95%	8.1	+56%	7.2	+53%
0.8	5.5	5.0	4.5	-18%	3.9	-21%	10.7	+94%	9.7	+95%	8.8	+60%	7.8	+56%
1	6.9	6.2	5.9	-14%	5.2	-17%	13.9	+102%	12.3	+99%	12.0	+74%	10.3	+66%

THE ENERGY CONSUMPTION RESULTS OBTAINED FROM THE SIMULINK MODEL (

Table 5-3) are considerably different with respect to the backward simulation (see Table 3-9). This is due to several factors which affect the results differently depending on the scenario.

In the battery electric eCargo simulations, the resulting energy consumption shows an average 5% less with respect to the backward simulation, probably due to the natural differences between the two modeling approaches such as tracking error and delay caused by the driver's model in Simulink. This is also confirmed by the average power demand on the DC-bus, which results slightly higher (see …) If regenerative braking capability is introduced, an advantage of 14% to 34% is achieved with respect to the benchmark. This advantage is reduced of 5% to 10% with respect to the backward model, as in the latter all the negative power at the wheels was assumed to be provided by the motor, while in Simulink also the contribution of ideal brakes is added. It can be assumed that these errors affect all the simulations but are mostly noticeable in the battery electric case.

The FC hybrid eCargo scenarios are characterized by a significant increase in energy consumption due to the lower driveline efficiency of the hybrid traction system with respect to the battery electric one. However, these increments are significantly higher with respect to the ones observed in the backward model (Table 3-9) due to the combined effects of

- An average -10% in driveline efficiency (See Table 5-4 and Table 3-10).
- The above-mentioned reduced regenerative braking capability resulting in higher average power demand on the DC-bus (see Table 5-5).
- An inefficient FCS management perpetrated by the fuzzy logic EMS, as illustrated earlier in Figure 5-9 and Table 5-3.

In conclusion, energy consumption for the plain FC hybrid case is about doubled, while regenerative braking can contain the energy consumption increase to +74% at most. It is worth to notice that in the backward simulation for PS=0.5 the energy consumption actually decreased with respect to the benchmark in the FC hybrid eCargo with regenerative braking, while in Simulink's results this does not hold. In general, it is safe to state that the results that should be expected when testing the prototype will be much closer to the higher fidelity Simulink model ones than to backward model, which should be used as preliminary dimensioning and consistency checks only.

TABLE 5-4. SIMULINK MODEL DRIVELINE EFFICIENCY RESULTS

Simscape: driveline efficiency [-]						
PS	**Battery only**		**with FCS range extender**			
	U1	**U2**	**U1**		**U2**	
0.5	0.86	0.86	0.47	-45%	0.45	-48%
0.7	0.86	0.87	0.47	-46%	0.46	-47%
0.8	0.86	0.86	0.46	-47%	0.46	-47%
0.8	0.86	0.86	0.46	-47%	0.46	-47%
1	0.87	0.87	0.44	-49%	0.45	-48%

TABLE 5-5. SIMULINK MODEL AVERAGE POWER DEMAND AT THE BUS

Simscape: average power demand at bus [W]		
PS	**Without regenerative braking**	**With regenerative braking**

	U1	**U2**	**U1**	**U2**
0.5	51	45	38	32
0.66	66	57	53	44
0.75	75	64	61	51
0.8	80	68	66	55
1	98	83	85	70

Finally, the results concerning the achieved range extension in all the analyzed combinations is presented in the table below.

TABLE 5-6. SIMULINK MODEL RANGE EXTENSION RESULTS

Simscape: range [Km]														
PS	**Battery only**		**with regenerative braking**				**with FCS range extender**				**FCS range extender & regenerative braking**			
	U1	**U2**	**U1**		**U2**		**U1**		**U2**		**U1**		**U2**	
0.5	144	160	202	+40%	241	+51%	374	+159%	393	+146%	514	+256%	555	+248%
0.66	110	122	140	+28%	165	+35%	280	+156%	307	+151%	358	+227%	403	+229%
0.75	97	107	120	+24%	138	+29%	244	+153%	267	+150%	301	+212%	340	+218%
0.8	91	100	110	+22%	127	+27%	227	+151%	250	+150%	277	+205%	314	+213%
1	73	80	85	+17%	97	+20%	176	+141%	197	+145%	204	+180%	236	+193%

Consistently with what stated so far, for the battery electric BCargo the introduction of regenerative braking would increase of at least 17% the usable range, which is again 7% less than the results obtained in the backward model because of the above-mentioned reduced regenerative braking capability. The FC hybrid BCargo, however, undergoes a range extension of at least +141% with respect to the baseline case, which becomes +180% if regenerative braking is also introduced. These growths are less than what predicted in the backward simulation because of the same reasons mentioned when commenting the energy consumption results, but still very significant for the aim of this thesis work.

6 Conclusions and perspective work

Summing up, results showed that the FC hybrid BCargo bike can potentially achieve a huge range extension with respect to the original model. In particular, range increases by a minimum factor of almost 2.5, which becomes almost 3 is regenerative braking is introduced. All this with very little additional weight, just 5 kg, and a small reduction of the cargo volume, potentially only 12 L. This provides considerable technical advantage with respect to all commercially available eCargo bikes by successfully increasing the bike range even for heavy-duty parcel delivery mission profiles, triggering a mass diffusion of these clean, traffic-reducing vehicles for last-mile delivery. Nonetheless, this design is far from flawless and could use some improvements. The most relevant are described below.

First, as mentioned in the previous chapter, the fuzzy-logic EMS does not perform well in keeping the highest possible FCS efficiency over the cycle, wasting de-facto up to more than 6% of the fuel. It should thus be tuned better by modifying or removing completely the “power follower” strategy for peaking power conditions, as it is believed to contribute a lot to the poor EMS performances. Additionally, the output FC current seen in Figure 5-4 experiences steep transients, which is not good for FCS performances and durability; the improvements in EMS strategy should address this matter as well.

Concerning the FCS system, further research should be conducted to find out if it would be possible to install a fuel cell system rated >250W on-board. If this were possible, the correct FCS dimensioning for high efficiency would be employing the FCS-C1000 stack mentioned in section 3.3. Another significant improvement to the Simulink model would be to substitute the current FC model in Figure 4-14 with the *fuel cell* block in Figure 4-13 to improve the model’s fidelity. This modification requires some quantitative intrinsic knowledge about the cells, such as the internal resistance, parameters about concentration and activation losses and the time dynamics of the stack.

Regarding the electromechanical part of the model, firstly more accurate data on the torque-speed characteristic for an average biker rather than an athlete should be found in order to correctly model its behavior into the rider model subsystems. The eMotor model could also be improved by substituting it with a Simscape block reproducing a real DC motor behavior (PM brushless, coreless, …) once more information on how the OLI eDrive installed on BCargo is available. Finally, the gearbox model should be substituted with a multi-speed gearbox in order to model the derailleur transmission. This also implies the creation of a gear speed profile for the reference driving cycles.

As for the electrical part, the first layout considered in Figure 4-18, even though it was not brought forward because of power split control issues, it boasts a simpler layout and fewer components with respect to the one adopted in this thesis work, so it should be given a second change by finding a way to manage the power split with that configuration. On the other hand, the TI bidirectional DC-DC converter on the battery side could be provided an external, digital voltage loop control for the LV port in such a way that it is possible to completely disable the FCS while keeping the bus voltage constant at 36V. At last, the hybridization battery dimensioning procedure in section 4.4 proved that the most desirable power buffer needs a very low energy content but high rated charging and discharging current. These requirements make supercapacitors an ideal candidate for the job, given their very high specific power despite a relatively low specific energy. It would be worth to find out whether the use of supercaps could save weight with respect to the current configuration.

Bibliography

[1] P. L. Parcu, N. Innocenti, C. Carrozza, and A. Pisarkiewicz, "The rise of e-commerce platforms in the parcel delivery markets," pp. 1–23, 2021.

[2] Energy saving trust, "Ecargo bikes," 2022. https://energysavingtrust.org.uk/service/e-cargo-bikes/#:~:text=An ecargo bike (also known,food%2C parcels or heavy goods. (accessed Jun. 15, 2022).

[3] EU, "Impact assessment - Proposal for a Regulation of the European Parliament and of the Council on cross-border parcel delivery services." https://publications.europa.eu/resource/cellar/9bd3a5b2-2330-11e6-86d0-01aa75ed71a1.0001.03/DOC_148

[4] C. Rudolph and J. Gruber, "Cargo cycles in commercial transport : Potentials , constraints , and recommendations," *Res. Transp. Bus. Manag.*, vol. 24, no. June, pp. 26–36, 2017, doi: 10.1016/j.rtbm.2017.06.003.

[5] Nicolas Collignon, "Why Cargo bikes? An empirical analysis of the Pedal Me fleet," 2020. https://pedalme.co.uk/why-cargo-bikes/ (accessed Jun. 15, 2022).

[6] Urban Arrow, "Frequently asked questions about the Cargo L & XL." https://urbanarrow.com/urban-arrow-faqs/cargo-faqs/ (accessed Jun. 15, 2022).

[7] Bergamont, "FAQ-FREQUENTLYASKED QUESTIONS." https://www.bergamont.com/gb/en/support/help

[8] HAN newsroom, "STUDENTS UNVEIL PROTOTYPE DUTCH HYDROCARGO BIKE_," 2021. https://www.hanuniversity.com/en/news/2021/09/students-unveil-prototype-dutch-hydrocargo-bike/ (accessed Jun. 15, 2021).

[9] ROBU.IN, "Introduction to E-bike Technology," 2021. https://robu.in/introduction-to-e-bike-technology/#:~:text=E-bike is an electric,throttle assist and pedal assist. (accessed Jun. 29, 2022).

[10] Pete, "Understanding Electric Bike Modes: Throttle vs. Pedal Assist (Pedelec)," *Electric Bike Report*, 2022. https://electricbikereport.com/electric-bike-throttle-pedal-assist-pedelec/

[11] D. A. J. Rand, R. M. Dell, and J. C. R. Hunt, *Hydrogen Energy : Challenges and Prospects*. Cambridge, UNITED KINGDOM: Royal Society of Chemistry, 2007. [Online]. Available: http://ebookcentral.proquest.com/lib/polito-ebooks/detail.action?docID=1185621

[12] J.-H. Jung and S. Ahmed, "Dynamic Model of PEM Fuel Cell Using Real-time Simulation Techniques," *J. Power Electron.*, vol. 10, Nov. 2010, doi: 10.6113/JPE.2010.10.6.739.

[13] J. Larminie and A. Dicks, *Fuel Cell Systems Explained*, vol. 93, no. 1–2. 2001. doi: 10.1016/s0378-7753(00)00571-1.

[14] P. Grady, G. Chen, S. Verma, A. Marellapudi, and N. Hotz, "A study of energy losses in the world's most fuel efficient vehicle," *2019 IEEE Veh. Power Propuls. Conf. VPPC 2019 - Proc.*, 2019, doi: 10.1109/VPPC46532.2019.8952212.

[15] P. J. Berlowitz and C. P. Darnell, "Fuel Choices For Fuel Cell Powered Vehicles," 2000. doi: 10.4271/2000-01-0003.

[16] M. Ehsani, Y. Gao, and Ali Emadi, *Modern electric, hybrid electric and fuel cell vehicles*. 2010.

[17] D. Wu, C. Peng, C. Yin, and H. Tang, “Review of System Integration and Control of Proton Exchange Membrane Fuel Cells,” *Electrochem. Energy Rev.*, vol. 3, no. 3, pp. 466–505, 2020, doi: 10.1007/s41918-020-00068-1.

[18] J. C. Kurnia, B. A. Chaedir, A. P. Sasmito, and T. Shamim, “Progress on open cathode proton exchange membrane fuel cell : Performance , designs , challenges and future directions,” *Appl. Energy*, vol. 283, no. November 2020, p. 116359, 2021, doi: 10.1016/j.apenergy.2020.116359.

[19] H. Zhao and B. Andrew, *Fuel Cell Powered Vehicles*. Wiley & sons, 2013. [Online]. Available: https://onlinelibrary.wiley.com/doi/10.1002/9781118354179.auto066

[20] G. Mohan, F. Assadian, and S. Longo, “An Optimization Framework for Comparative Analysis of Multiple Vehicle Powertrains,” *Energies (Basel)*, vol. 6, no. 10, pp. 5507–5537, 2013, doi: 10.3390/en6105507.

[21] G. Yao *et al.*, “Traffic-Condition-Prediction-Based HMA-FIS Energy-Management Strategy for Fuel-Cell Electric Vehicles,” *Energies*, vol. 12, p. 4426, Nov. 2019, doi: 10.3390/en12234426.

[22] Q. Xue, X. Zhang, T. Teng, J. Zhang, Z. Feng, and Q. Lv, “A Comprehensive Review on Classification, Energy Management Strategy, and Control Algorithm for Hybrid Electric Vehicles,” 2020.

[23] J. Lin, “Fuel cell vehicle simulation and optimization based on ADVISOR,” Politecnico di Torino, 2021. [Online]. Available: https://webthesis.biblio.polito.it/18858/

[24] BCARGO, “Manuale d’uso e scheda tecnica bici eCargo.” 2020.

[25] OLI eBike systems, “MOVE / MOVE PLUS - unità motrice e display.” 2018.

[26] Urban Arrow, “Cargo,” 2022. https://urbanarrow.com/business-bikes/cargo/

[27] Horizon technologies, “H-SERIES AIR COOLED 10W-5kW PEM STACK MODULES.” 2020. [Online]. Available: https://www.horizonfuelcell.com/hseries

[28] Fuel Cell Earth, “Horizon 1000W PEM Fuel Cell,” 2022. https://www.fuelcellearth.com/fuel-cell-products/horizon-1000w-pem-fuel-cell/ (accessed Jul. 01, 2022).

[29] Robert Bosch Gmbh, “PowerPack 300|400|500, PowerTube 400|500|625.” 2020.

[30] MathWorks, “MATLAB Documentation.” 2022.

[31] S. Strom, K. Nathan, and J. Woland, *Site Engineering for Landscape Architects*, 6. Aufl. Somerset: Somerset: Wiley, 2013.

[32] C. Abbiss, “Optimal cadence selection during cycling,” no. March 2014, 2009.

[33] J. Doke, “GRABIT,” 2022. https://it.mathworks.com/matlabcentral/fileexchange/7173-grabit

[34] Horizon fuel cell technologies, “H-200 Fuel Cell Stack User Manual.” pp. 1–17, 2013.

[35] HES Energy Systems, “HES Cylinders Series F datasheet.” p. 12245. [Online]. Available: https://www.h3dynamics.com/hydrogen-storage-and-accessories

[36] HES Energy Systems, "Ultralight H 2 Gas Pressure Regulator," vol. 10. p. 517.

[37] Vogtlin instuments, "Red-y compact 2 series product information."

[38] Texas Instrumets, "LAUNCHXL-F28379D C2000 Delfino MCU F28379D LaunchPad™ development kit." https://www.ti.com/tool/LAUNCHXL-F28379D?keyMatch=&tisearch=search-everything&usecase=hardware#tech-docs (accessed Jul. 05, 2022).

[39] Texas Instruments, "LM5170-Q1 EVM User Guide," no. December, pp. 1–38, 2016, [Online]. Available: www.ti.com

[40] Texas Instruments, "LM5170-Q1 Multiphase Bidirectional Current Controller," no. November 2016, 2017.

[41] TDK Lambda, "i7C Series." pp. 1–7, 2022. [Online]. Available: https://product.tdk.com/en/search/power/switching-power/dc-dc-converter/info?part_no=i7C4W008A120V-003-R

[42] TDK Lambda, "Evaluation kit manual for i7A and i7C non-isolated DC-DC series." pp. 1–12. [Online]. Available: https://product.tdk.com/en/search/power/switching-power/pwr-acc/info?part_no=i7C08A-C03-EVK-S1

[43] TDK Lambda, "i3A Series datasheet." pp. 1–5, 2021. [Online]. Available: https://product.tdk.com/en/search/power/switching-power/dc-dc-converter/info?part_no=i3A4W008A033V-001-R

[44] TDK Lambda, "Evaluation Kit Manual for i3A and i6A Non-Isolated DC-DC Series." [Online]. Available: https://product.tdk.com/en/search/power/switching-power/pwr-acc/info?part_no=i3A08A-C01-EVK-S1

[45] Bafang, "BT F05.200.C." https://bafang-e.com/en/oem-area/components/component/battery/bt-f05200c-1/ (accessed Jun. 06, 2022).

[46] Bafang Electric, "Bafang 43V battery design – Advantages compared to 36V and 48V systems," 2019.

[47] Samsung SDI, "INR18650-25R Testing and Specifications," 2013.

[48] lygte, "LG 18650 MJ1 3500mAh (Green)." https://lygte-info.dk/review/batteries2012/LG 18650 MJ1 3500mAh (Green) UK.html

[49] L. Yang, E. Markert, and U. Heinkel, "Fuzzy logic based energy management algorithm of a hybrid electric vehicle with range-extender," *2014 IEEE 11th Int. Multi-Conference Syst. Signals Devices, SSD 2014*, pp. 1–5, 2014, doi: 10.1109/SSD.2014.6808880.